

A COUPLED FLOW AND CHEMICAL REACTOR NETWORK MODEL FOR  
PREDICTING GAS TURBINE COMBUSTOR PERFORMANCE

A THESIS SUBMITTED TO  
THE GRADUATE SCHOOL OF NATURAL AND APPLIED SCIENCES  
OF  
MIDDLE EAST TECHNICAL UNIVERSITY

BY

SEYFETTİN ERTAN HATAYSAL

IN PARTIAL FULFILLMENT OF THE REQUIREMENTS  
FOR  
THE DEGREE OF DOCTOR OF PHILOSOPHY  
IN  
MECHANICAL ENGINEERING

MARCH 2016



Approval of the thesis:

**A COUPLED FLOW AND CHEMICAL REACTOR NETWORK MODEL  
FOR PREDICTING GAS TURBINE COMBUSTOR PERFORMANCE**

submitted by **Seyfettin Ertan Hataysal** in partial fulfillment of the requirements for the degree of **Doctor of Philosophy in Mechanical Engineering Department, Middle East Technical University** by,

Prof. Dr. Gülbin Dural Ünver  
Dean, Graduate School of **Natural and Applied Sciences**

Prof. Dr. R. Tuna Balkan  
Head of Department, **Mechanical Engineering**

Assoc. Prof. Dr. Ahmet Yozgatlıgil  
Supervisor, **Mechanical Engineering Dept., METU**

**Examining Committee Members:**

Assoc. Prof. Dr. Metin Yavuz  
Mechanical Engineering Dept., METU

Assoc. Prof. Dr. Ahmet Yozgatlıgil  
Mechanical Engineering Dept., METU

Prof. Dr. Nuri Yücel  
Mechanical Engineering Dept., GAZİ UNI.

Assoc. Prof. Dr. Murat Kadri Aktaş  
Mechanical Engineering Dept., TOBB ETU

Assist. Prof. Dr. Feyza Kazanç  
Mechanical Engineering Dept., METU

**Date : 02.03.2016**

**I hereby declare that all information in this document has been obtained and presented in accordance with academic rules and ethical conduct. I also declare that, as required by these rules and conduct, I have fully cited and referenced all material and results that are not original to this work.**

Name, Last name : Seyfettin Ertan HATAYSA

Signature :



## **ABSTRACT**

### **A COUPLED FLOW AND CHEMICAL REACTOR NETWORK MODEL FOR PREDICTING GAS TURBINE COMBUSTOR PERFORMANCE**

Hataysal, Seyfettin Ertan

Ph.D., Department of Mechanical Engineering

Supervisor: Assoc. Prof. Dr. Ahmet Yozgatligil

March 2016, 166 pages

A 1D flow and chemical reactor network model was developed to predict the performance of a combustor chamber and the model output was verified by the 3D Computational Fluid Dynamics (CFD) analysis and experimental measurements of the chamber. To obtain chamber flow split three different nodal flow network solvers were coupled with a chemical reactor network model. Simplified, segregated and direct solutions of the nodal equations were led to these three different flow solvers. Flow models were utilized to predict the flow, pressure, density and temperature distribution inside the chamber domain. After getting a converged solution, the reactor network processed the incoming data inside its inner loop. The output of the reactor network was fed back to the flow network and the solution is iterated until convergence of the whole system. The network model can supply information about pressure drop, pressure distribution, average temperature distribution, species distribution and flow split. For the verification of the results, a detailed CFD analysis was performed on a seven sector annular test combustor of TEI. Basic performance investigation experiments of the combustor were utilized for comparison of the results. The numerical results were presented for two different detailed chemical mechanisms. The results showed that preliminary code predicted an accurate flow

distribution. Pressure distribution also showed consistency with the CFD results however level of predictions was found to change from model to model. Inner temperature profiles got the trend changes at the dilution and exit zones, however developed code predicted higher elemental temperatures at the main combustion zones. Finally the code was modified to include design parameters and thermal prediction feature for the liner cooling. A new design was also made by using this capability of the code. The performance of the new design is also presented.

Keywords: flow network, chemical reactor network, turbulent combustion, combustor CFD, combustor performance, combustor preliminary design

## ÖZ

### GAZ TÜRİNİ YANMA ODASI PERFORMANSININ TAHMİNİ İÇİN BİR EŞLENİK AKIŞ VE KİMYASAL REAKTÖR MODELİ

Hataysal, Seyfettin Ertan

Yüksek Lisans, Makina Mühendisliği Bölümü

Tez Yöneticisi: Assoc. Prof. Dr. Ahmet Yozgatlıgil

Mart 2016, 166 sayfa

Bir yanma odasının performansını tahmin edebilmek için bir boyutlu akış ve kimyasal reaktör ağ modeli geliştirilmiş ve bu model 3 boyutlu Hesaplamalı Akışkanlar Dinamiği (HAD) analizleri ve yanma odası deney sonuçları ile doğrulanmıştır. Yanma odasındaki akış dağılım karakterinin elde edilmesi için üç farklı nodal akış çözücü bir kimyasal reaktör ağ modeli ile eşleştirilmiştir. Sadeleşmiş, ayrılmış ve doğrusal olmayan yaklaşımlar kullanılarak nodal denklemler çözülmüş ve bu sayede üç farklı çözücü incelenmiştir. Akış çözücü modelleri yanma odası içerisinde akış, basınç, yoğunluk ve sıcaklık dağılımlarının tespit edilmesini sağlamıştır. Yakınsayan bir çözüm elde edildikten sonra, reaktör ağı elde edilmiş veriyi işleyerek kendi çevriminde kullanmaktadır. Reaktör ağının ürettiği çıktı daha sonra tekrar akış ağına beslenir, ve süreç bu şekilde tamamen yakınsamış bir sonuç elde edilene kadar devam ettirilir. Ağ modeli basınç düşüşü, basınç dağılımı, ortalama sıcaklık dağılımları, kimyasal tür dağılımı ve akış dağılımı ile ilgili bilgi vermektedir. Ağ modeli ile elde edilen ortalaması alınmış sonuçların doğrulanabilmesi için detaylı bir

HAD analizi TEI tarafından tasarlanıp üretilmiş yedi sektörlü annular bir yanma odasına uygulanmıştır.

Buna ilave olarak, bu yanma odası üzerinde gerçekleştirilmiş temel performans testleri de karşılaştırma amacıyla sunulmuştur. Numerik çalışma iki farklı detaylı kimyasal mekanizma kullanılarak sunulmuştur. Sonuçlar incelendiğinde ön performans kodunun akış dağılımını yüksek bir kesinlikle tahmin edebildiği gösterilmiştir. Basınç dağılımlarının da CFD sonuçları ile uyum gösterdiği ancak modelden modele merite olarak bazı farklar ortaya çıktığı gözlenmiştir. İç sıcaklık dağılımlarının trend olarak çıkışa yakın bölgelerde CFD sonuçları ile uyumlu olduğu ancak ana yanma bölgesinde 1 boyutlu kodun daha yüksek sıcaklıklar öngördüğü tespit edilmiştir. Son olarak geliştirilen koda temel tasarım parametreleri ve ısı yanma odası duvar soğutma özelliğinin belirlenebilmesi için ısı karakteri tespit eden fonksiyonlar eklenmiştir. Bu özellikleri kullanarak yeni bir yanma odası da tasarlanmıştır. Bu yanma odasının performans analizleri de burada sunulmuştur.

Anahtar sözcükler: akış ağı, kimyasal reaktör ağı, türbülent yanma, yanma odası HAD, yanma odası performans, yanma odası ön tasarımı

*to my dear wife Eda and my son Doğu*

## **ACKNOWLEDGMENTS**

The author wishes to express his deepest gratitude to his supervisor, Assoc. Prof. Dr. Ahmet Yozgatlıgil; for his guidance, advice, criticism, encouragement, insight and endless support throughout the research.

The author also wants to express his gratitude to Assoc. Prof. Dr. Metin Yavuz and Assoc. Prof. Dr. Murat Kadri Aktaş for their guidance, advice and criticism during the thesis progress meetings.

The author also would like to thank his dear wife Eda Önat Hataysal for her endless love, support and patience during this period.

And special thanks to colleagues and companions, Cem Gözükara, Güvenç Canbaloğlu, Mustafa Ocak, Osman Akdağ and Serkan Kayılı, for their moral support and their precious friendship.

Finally the author would like to mention the name of Prof. Dr. Cahit Eralp who passed away in 2010, his great engineering legacy is going to be kept and transferred to the new generations.

## TABLE OF CONTENTS

ABSTRACT.....	v
ÖZ .....	vii
ACKNOWLEDGMENTS .....	x
TABLE OF CONTENTS.....	xi
LIST OF TABLES .....	xv
LIST OF FIGURES .....	xvii
LIST OF SYMBOLS .....	xxii
CHAPTERS	
INTRODUCTION .....	1
1.1 The Background and Literature Survey .....	2
1.1.1 Flow Network Solvers .....	2
1.1.2 Reactor Networks.....	3
1.2 Theory .....	6
1.2.1 Flow and Chemical Reactor Network Equations .....	6
1.2.1.1 Flow Equations .....	6
1.2.1.2 Incompressible Extension of the Equations .....	9
1.2.1.3 Compressible Extension of the Equations .....	9
1.2.1.4 Reactor Theory .....	11
1.2.2 CFD Theory .....	11
1.2.2.1 General Equations of Fluid Motion .....	12
1.2.2.2 Reynolds-Averaged Navier-Stokes Equations .....	13
1.2.2.3 k- $\epsilon$ turbulence model.....	15
1.2.2.4 Scale-Adaptive Simulation (SAS) Model .....	18
1.2.2.5 Non-Premixed Combustion CFD Model .....	21
NUMERICAL MODELS .....	27
2.1 Network Structure .....	27

2.2 Flow Models.....	29
2.2.1 Linear Method .....	29
2.2.2 Segregated Method.....	30
2.2.3 Non-linear Method .....	35
NETWORK MODEL COMBUSTOR APPLICATION .....	39
3.1 Combustor Network Model.....	39
3.2 Loss Models .....	42
3.3 Fuel Surrogate Models .....	44
3.3.1 Aviation Fuels General.....	44
3.3.2 Chemical Modeling of Jet Fuels.....	46
3.4 Combustor Results .....	47
COMBUSTOR PERFORMANCE VERIFICATION DATA .....	57
4.1 CFD Verification.....	57
4.1.1 Model Description.....	57
4.1.2 Boundary Conditions.....	59
4.1.3 Numerical Settings .....	60
4.1.4 RANS-CFD Results .....	63
4.1.4.1 Velocity Results .....	64
4.1.4.2 Flow Streamlines.....	70
4.1.4.3 Temperature Results.....	74
4.1.4.4 Total Pressure Results .....	76
4.1.4.5 Species Distribution Results.....	79
4.1.5 SAS-CFD Results.....	86
4.1.5.1 Velocity Results .....	86
4.1.5.2 Flow Streamlines.....	90
4.1.5.3 Temperature Results.....	90
4.2 Experimental Verification .....	94
4.2.1 Experiment Set-up.....	94
4.2.1.1 General .....	94
4.2.1.2 Measurement Instrumentation.....	97
4.2.2 Test Objective .....	97
4.2.3 Test Methodology .....	98



4.2.4 Test Results .....	100
4.2.4.1 Temperature Measurements .....	102
4.2.4.2 Total Pressure Loss Measurements .....	103
4.2.4.3 Species Measurements .....	104
APPLICATION: A COMBUSTOR DESIGN TOOL .....	107
5.1 Combustor Design Methodology .....	107
5.2 Basic Combustor Design Parameters .....	107
5.3 Thermal Design .....	112
5.3.1 Heat Transfer Model .....	112
5.3.2 Internal Radiation, $R_i$ .....	114
5.3.3 Internal Convection, $C_i$ .....	116
5.3.4 External Radiation, $R_o$ .....	116
5.3.5 External Convection, $C_o$ .....	117
5.3.6 Calculation Procedure .....	118
5.4 Wall Cooling Design and Implementation .....	119
5.4.1 Film Cooling Methods .....	120
5.4.2 Implementation of Film Cooling to the Heat Transfer Model .....	122
5.5 Design Code Solution Methodology .....	125
5.6 Case Study: A New Test Combustor .....	127
5.6.1 Existing Combustor Configuration .....	127
5.6.2 New Combustor .....	129
5.6.3 Detailed Performance Analysis of the New Design .....	137
5.6.3.1 Velocity Results .....	141
5.6.3.2 Flow Streamline .....	145
5.6.3.3 Temperature Results .....	146
5.6.3.4 Total Pressure Results .....	148
CONCLUSION AND FUTURE WORK .....	151
6.1 Conclusion .....	151
6.2 Future Work .....	156
REFERENCES .....	157
APPENDICES	
A.EXPERIMENTAL EQUIPMENTS .....	161

A.1 Temperature Measurements .....	161
A.2 Pressure Measurements .....	162
A.3 Species Concentration Measurements .....	162
CURRICULUM VITAE .....	165

## LIST OF TABLES

### TABLES

Table 3.1 – Hole element numbers and their corresponding location.....	41
Table 3.2 – Common Characteristics of Jet Fuels [29].....	44
Table 3.3 – World Survey Composition Results [29].....	45
Table 3.4 – Jet A Surrogates [30].....	46
Table 3.5 – JP-8 Surrogates [30].....	46
Table 3.6 – JP-8 Surrogates - Aachen [30] .....	46
Table 3.7 – Hole mass flow distribution in percentage - Aachen Mechanism .....	51
Table 3.8 – Hole mass flow distribution in percentage - Creck Mechanism .....	56
Table 4.1 – Combustion chamber test boundary conditions .....	60
Table 4.2 – Analysis Settings.....	61
Table 4.3 – Convergence Criteria for the Analysis.....	63
Table 4.4 – Combustion Chamber Operating Conditions.....	98
Table 4.5 – The List of Measurement Points at the Chamber Exit.....	101
Table 5.1– Basic combustor design parameters for the existing design .....	128
Table 5.2– Basic combustor design parameters for the new combustor.....	130
Table 5.3– Current mass flow distribution between the holes of the new design, iteration-1 .....	131
Table 5.4– Gas temperature of the new design, iteration-1 .....	132
Table 5.5– Liner wall temperature of the new design, iteration-1 .....	133
Table 5.6– Hole area iterations to get optimum wall cooling mass flow.....	135
Table 5.7 – Analysis Settings.....	139
Table 5.8 – Combustion chamber CFD boundary conditions.....	140
Table 5.9 – Convergence Criteria for the Analysis.....	141
Table 6.1 - Solver runtime comparison.....	153

Table 6.2 – Mass flow rate percentage comparison of existing and new designs....	155
Table A.1– Thermocouple properties.....	161
Table A.2– Pressure transducer properties.....	162
Table A.3– Gas analyzer unit properties .....	163
Table A.4– Gas analyzer measurement specs. ....	163

## LIST OF FIGURES

### FIGURES

Figure 1.1 - The CFD-to-CRN model of Fichet et al. [19] .....	4
Figure 1.2 - CRN model of Chen et al. [21].....	5
Figure 1.3 - ERN Model of Drennan et al. [24] .....	6
Figure 1.4 - A pipe element.....	7
Figure 1.5 – Comparison of SST-URANS with SST-SAS solutions for cylinder in cross flow [38].....	19
Figure 1.6 – Graphical description of PDF function.....	24
Figure 2.1 - A sample flow network .....	27
Figure 2.2 - Notation used to define a network.....	28
Figure 2.3 -The Iteration Steps of the Pressure Corrector Scheme.....	35
Figure 3.1 - Network map of the combustor .....	40
Figure 3.2 - Solution procedure for the network system.....	42
Figure 3.3 – Flow Through Liner Hole [1] .....	43
Figure 3.4 - Sudden expansion and sudden contraction loss elements .....	43
Figure 3.5 - Total pressure distribution outer annulus nodes -Aachen mechanism ...	48
Figure 3.6 - Total pressure distribution inner annulus nodes -Aachen mechanism ...	48
Figure 3.7 - Total pressure distribution liner inner nodes - Aachen mechanism .....	49
Figure 3.8 - Total pressure drop - Aachen mechanism .....	49
Figure 3.9 - Temperature distribution - liner elements - Aachen mechanism .....	50
Figure 3.10 - Average exit temperature - Aachen mechanism.....	51
Figure 3.11 - Total pressure distribution outer annulus nodes -Creck mechanism....	52
Figure 3.12 - Total pressure distribution inner annulus nodes -Creck mechanism....	53
Figure 3.13 - Total pressure distribution - liner inner nodes - Creck mechanism .....	53
Figure 3.14 - Total pressure drop - Creck mechanism.....	54

Figure 3.15 - Temperature distribution - liner elements - Creck mechanism .....	55
Figure 3.16 - Average exit temperature - Creck mechanism .....	55
Figure 4.1 - TEI experimental through flow combustor [34].....	57
Figure 4.2 - Cut Section of the TEI Combustor .....	58
Figure 4.3 - Liner Air Flow Hole Configuration.....	59
Figure 4.4 - Combustor solution grid .....	60
Figure 4.5 - Change of temperature for aachen mechanism for scalar dissipation ....	62
Figure 4.6 - Velocity distribution along centerline section .....	64
Figure 4.7 - Velocity vector distribution along centerline section .....	65
Figure 4.8 - Mach number distribution along centerline section .....	65
Figure 4.9 - Velocity distribution at the exit plane .....	66
Figure 4.10 - Mach number distribution at the exit plane .....	66
Figure 4.11 - Velocity distribution along centerline section .....	67
Figure 4.12 - Velocity vector distribution along centerline section .....	68
Figure 4.13 - Mach number distribution along centerline section .....	68
Figure 4.14 - Velocity distribution at the exit plane .....	69
Figure 4.15 - Mach number distribution at the exit plane.....	69
Figure 4.16 – Streamlines emanating from the inlet .....	70
Figure 4.17 – Streamlines emanating from the swirler holes.....	71
Figure 4.18 – Streamlines emanating from liner holes .....	71
Figure 4.19 – Streamlines emanating from the inlet .....	72
Figure 4.20 – Streamlines emanating from the swirler holes.....	73
Figure 4.21 – Streamlines emanating from liner holes .....	73
Figure 4.22 - Temperature distribution along centerline.....	74
Figure 4.23 - Exit plane temperature distribution .....	75
Figure 4.24 - Temperature distribution along centerline.....	75
Figure 4.25 - Exit plane temperature distribution .....	76
Figure 4.26 - Total pressure distribution along centerline .....	77
Figure 4.27 - Pressure drop distribution at the exit plane .....	77
Figure 4.28 - Total pressure distribution along centerline section .....	78
Figure 4.29 - Pressure drop distribution at the exit plane .....	79
Figure 4.30 - O <sub>2</sub> and CO <sub>2</sub> mass fraction percentage along centerline exit plane .....	80

Figure 4.31 – $C_{10}H_{22}$ Mass fraction distribution along centerline section .....	80
Figure 4.32 – $C_9H_{12}$ Mass fraction distribution along centerline section .....	81
Figure 4.33 – $CO_2$ Mass fraction distribution along centerline section .....	81
Figure 4.34 – $H_2O$ Mass fraction distribution along centerline section .....	82
Figure 4.35 – CO Mass fraction isosurface, $Y_{CO}=0.1$ .....	82
Figure 4.36 - $O_2$ and $CO_2$ mass fraction percentage along centerline exit plane .....	83
Figure 4.37 – $C_{10}H_{22}$ Mass fraction distribution along centerline section .....	84
Figure 4.38 – $C_9H_{12}$ Mass fraction distribution along centerline section .....	84
Figure 4.39 – $CO_2$ Mass fraction distribution along centerline section .....	85
Figure 4.40 – $H_2O$ Mass fraction distribution along centerline section .....	85
Figure 4.41 – CO Mass fraction isosurface, $Y_{CO}=0.1$ .....	86
Figure 4.42 - Velocity distribution along centerline section - instantaneous values at $t=0.02$ sec .....	87
Figure 4.43 - Velocity distribution along centerline section - time averaged velocity distribution .....	88
Figure 4.44 - Velocity vector distribution along centerline section- instantaneous values at $t=0.02$ sec .....	88
Figure 4.45 - Velocity distribution at the exit plane - instantaneous values at $t=0.02$ sec .....	89
Figure 4.46 - Velocity distribution at the exit plane - time averaged velocity distribution .....	89
Figure 4.47- Streamlines emanating from the inlet - instantaneous values at $t=0.02$ sec .....	90
Figure 4.48 - Temperature distribution along centerline- instantaneous values at $t=0.02$ sec .....	91
Figure 4.49 - Temperature distribution along centerline- time averaged values .....	91
Figure 4.50 - Exit plane temperature distribution- instantaneous values at $t=0.02$ sec .....	92
Figure 4.51 - Exit plane temperature distribution- instantaneous values at $t=0.02$ sec .....	92
Figure 4.52 – CO Mass fraction isosurface, $Y_{CO}=0.1$ .....	93
Figure 4.53 - Combustion Chamber Performance Test Set-up Sketch .....	94

Figure 4.54 - Test Set-up Photos .....	95
Figure 4.55 - Test Section and Instrumentation .....	96
Figure 4.56 - Traverse Blocks and Measurement Probe .....	97
Figure 4.57 - Ignition Operation and Normal Operation of the Chamber.....	99
Figure 4.58 - a. Zero of the Measurement Grid b. Measurement Points.....	100
Figure 4.59 - Experimental Exit Temperature Distribution .....	102
Figure 4.60 - Percent Pressure Drop at Combustion Chamber Exit.....	103
Figure 4.61 - O <sub>2</sub> and CO <sub>2</sub> Mass Fraction Percentage wrt. Angular Position .....	104
Figure 4.62 - Centerline Temperature and NO <sub>x</sub> amount in ppm wrt. Angular Position .....	105
Figure 4.63 - CO, C <sub>x</sub> H <sub>y</sub> , NO <sub>x</sub> amount in ppm wrt. Angular Position .....	105
Figure 4.64 - Pressure drop distribution at the exit plane .....	149
Figure 5.1 – Mach number limits inside the combustor [2] .....	110
Figure 5.2 – Fuel-air equivalence ratio limits inside the combustor [2] .....	111
Figure 5.3 – Thermal flow through combustion liner [1] .....	113
Figure 5.4 – Simple film cooling slot representation. ....	120
Figure 5.5 – Film cooling configurations: a. wiggletrip b. stacked ring c. splash-cooling ring d. machined ring [1].....	121
Figure 5.6 – Improves film cooling configurations [1].....	122
Figure 5.7 - Solution procedure for the 1D design code .....	126
Figure 5.8 – Combustor zones, iteration-1 .....	132
Figure 5.9 – Network model of the new combustor.....	134
Figure 5.10 – Average wall temperature calculated downstream of the cooling holes at 1 <sup>st</sup> and 2 <sup>nd</sup> Zones.....	136
Figure 5.11 – New combustor design with film cooling.....	137
Figure 5.12 – New combustor solution grid.....	138
Figure 5.13 – Velocity distribution along centerline section .....	142
Figure 5.14 – Velocity vector distribution along centerline section .....	143
Figure 5.15 – Mach number distribution along centerline section.....	143
Figure 5.16 – Velocity distribution at the exit plane.....	144
Figure 5.17 – Mach number distribution at the exit plane .....	144
Figure 5.18 – Streamlines emanating from the inlet .....	145



Figure 5.19 – Streamlines emanating from the swirler holes.....	146
Figure 5.20 – Streamlines emanating from liner holes .....	146
Figure 5.21 – Temperature distribution along centerline section .....	147
Figure 5.22 – Temperature distribution at the exit plane .....	147
Figure 5.23 – Temperature distribution on liner walls – centerline section.....	148
Figure 5.24 - Total pressure distribution along centerline .....	149

## LIST OF SYMBOLS

$\rho$	: density
$V$	: velocity
$P$	: total pressure
$A$	: element area
$D$	: element diameter, hydraulic diameter
$dx$	: infinitesimal pipe element
$g$	:gravitational acceleration
$F$	:body force,
$\tau_0$	:shear stress
$f$	: friction factor, mixture fraction
$\bar{f}^2$	: mixture fraction variance
$l$	: length of the element
$\dot{m}$	: mass flow
$Y$	: species mass fraction
$U$	: internal energy
$T$	: temperature, time in PDF section
$\dot{Q}$	: heat generated
$h$	: enthalpy
$t$	: time
$\kappa$	:dynamic pressure terms
$d$	: external mass flow
$s_{ij}$	: is a direction indicator of the flow inside the element it either gets 1 or -1.
$f_{ij}$	: element loss
$i$	: global node number

$j$	: local branch number
$J$	: Jacobian of the matrix
$u$	: u component of velocity
$v$	: v component of velocity
$w$	: w component of velocity
$\mu$	: dynamic viscosity
$S$	: source terms, rate of deformation
$k$	: turbulence kinetic energy
$\varepsilon$	: rate of dissipation of turbulent kinetic energy, convergence criterion
$L_{VK}$	: Von Karman length scale
$Z$	: mass fraction
$\phi$	: equivalence ratio
$C_D$	: discharge coefficient
$\psi$	: ratio of jet dynamic pressure to the annulus dynamic pressure
$\alpha$	: ratio of hole mass flow rate to annulus mass flow rate
$I$	: combustion intensity
CL	: combustor loading
$t_{res}$	: residence time
$\dot{m}_{31}$	: mass flow entering to the combustor
$\dot{m}_f$	: fuel mass flow rate
$\eta_c$	: combustion efficiency
$LHV$	: fuel lower calorific value
$P_{31}$	: inlet pressure of the combustor
$T_{31}$	: inlet temperature
$V$	: liner volume
$\sigma$	: Stefan Boltzmann constant
$\varepsilon_g$	: gas emissivity at average gas temperature at the axial location
$\alpha_g$	: absorptivity of the gas at wall temperature
*	: tentative values
'	: corrections, fluctuating components of flow parameters



## **CHAPTER 1**

### **INTRODUCTION**

Gas turbine combustor design includes preliminary design, detailed design and rig testing for verification phases. In preliminary design phase analytical and semi-empirical models are utilized to generate a rapid, reduced dimensional model of combustion chamber. Key performance parameters are pressure drop, exit average temperature, flow split through liner holes and Mach number along the gas path. Additional preliminary design features like average wall temperature and average species distribution can also be obtained.

Preliminary design tools are restricted with the semi-empirical design limits these are available in various sources [1-3]. Detailed design phase includes detailed CFD modeling of the combustor flow domain and there exists many sub-phases which cause this phase to consume significant amount of time. In order to shorten the design cycle for combustors, preliminary tools are preferred and there exists different preliminary design approaches available in the literature. Simplified preliminary design approaches are not only used at the pre-design phase but nowadays they are linked with the outcomes of the detailed design phase. This is mainly related with the strict emission regulations for aero engines. In order to control the emission characteristics of the chambers simplified reactor approaches are attached to the detailed design output of the chambers.

In this study, a simplified performance prediction tool is presented. The flow network solver methods are coupled with chemical reactor network and they are compared with the detailed 3D analysis of a prototype combustor.

## **1.1 The Background and Literature Survey**

### **1.1.1 Flow Network Solvers**

Modeling of flow inside the gas turbine combustors can be simplified by utilizing a pipe flow approach simply called Network approach. Pipe flow network solvers have an essential history and they were modified many times for inventing a better approach in the past years. Flow network solvers are generally classified into three categories which are loop, element and node solvers [4].

Loop methods, as the ancestor of the network methods, were presented by Hardy Cross in 1936 [5]. The method simply groups the several branches inside the flow loops and solves a general mass flow conservation equation. The method was especially suitable for limited computational sources however it came with several shortcomings such as defining of the loop structure for complicated cases and conservation of the initial flow distribution during initialization phase [6]. The shortcoming of the method led to a search for improved versions.

Element methods although require more storage they reported to be converged better [7], however they also require to define loop structures separately. Node methods however, have a couple of advantages when compared with the other two methods. They require less computational power, can be adapted for different boundary conditions [4], system initiation without specifying the initial conserved flow values and no specifying of the loops. This method also has the similar structure with the Navier-Stokes CFD solvers. This character of the method enables Greyvenstein et al. [4] to adapt segregated solver approach to nodal method. They applied Patankar and Spalding's [4] Semi-Implicit Method for Pressure-Linked Equations (SIMPLE) algorithm to the node method.

Nodal equations can also be solved directly or by using simplifications. The former approach results in solution of a large system matrix composed of linear node flow equations and non-linear head loss equations. The solution of the non-linear system

both satisfies the head loss and continuity equations. This method is described in works of Costa et al. [8]. The simplified solution of the nodal equations is based on the Linear Theory Method (LTM). The non-linear equations in direct the solution of the flow network system is linearised according to the LTM and a simplified nodal set of equations are solved by basic matrix algebra [9-11].

The works on nodal methods are excessively available in literature. The segregated nodal method, [4], was also applied to the gas turbine combustors in the works of Stuttford [12]. The segregated method was combined with the energy equation by the help of an enthalpy balance equation. This was mainly achieved by defining the properties of the mixture in each network element. The mixture composition was decided by utilization of some mixing and recirculation models. The reaction temperatures were decided by using constrained equilibrium model. Furthermore conduction, convection and radiation are also taken into account to find the wall temperature distribution. Another significant work on segregated model is performed by Pretorius et al [13-14]. They developed a hybrid nodal method, which was based on solving the pressure field accurately before the flow field inside the network. They extended the segregated model for systems including flows with higher Mach numbers. Direct solution of the nodal approach is widely used in gas pipelines and given in many different researches [15-16].

### **1.1.2 Reactor Networks**

Chemical Reactor Networks (CRN) are widely used in predicting preliminary performance of gas turbine performance. Reactors are small tubes which has input ports and an outlet port. The incoming fuel and air are well mixed inside and react according to the reaction kinetics. The reactors can be connected in series for simulating successive hole rows and mass flow injections. And also can be connected in parallel to simulate recirculation regions. The work of Murthy [17] gave an outline of the older efforts for modeling of combustor reactor models. In his study, he developed a semi-empirical 1D flow and thermal model to predict the equilibrium composition inside combustor. Another flow split and equilibrium chemistry utilized

reactor model was studied by Rodriguez and O'brien mentioned in Stuttford [6] but these models were limited with their capacity of modeling different geometries. This main disadvantage of semi-empirical methods is reported as the adaption of the methods to different cases [6]. CRN can get flow information from detailed CFD analysis [18] by equivalent processing approach, by this way it is possible to obtain chemical species concentrations and temperature with detailed chemical reaction mechanisms in a fast manner, this type of modeling is useful for industry. Equivalent reactor modeling from CFD was also utilized to predict a target species inside a combustor [19-20].

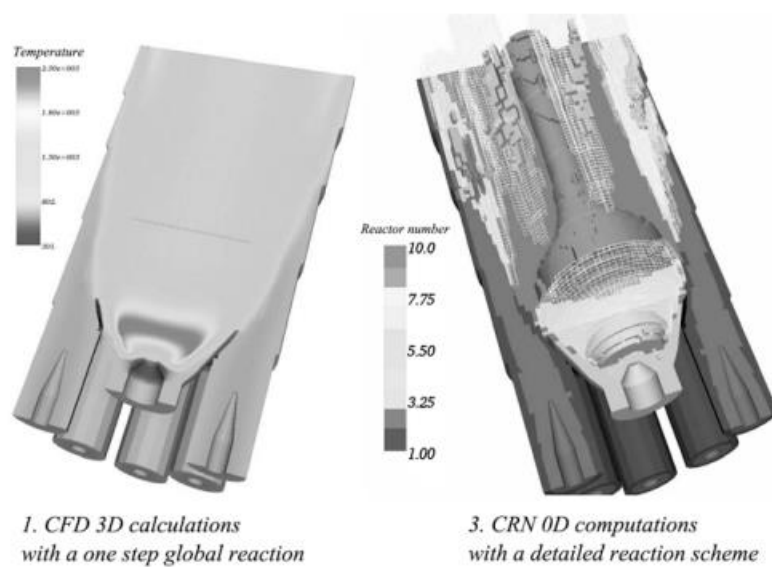


**Figure 1.1** - The CFD-to-CRN model of Fichet et al. [19]

By concentrating on a species such as  $\text{NO}_x$ , it is possible to make a sensitivity analysis regarding the humidity and gas turbine load. In the work by Chen et al [21], a preset CRN was utilized to design and optimize a gas turbine combustor. Target temperature and concentration of critical species were examined by changing the flow distribution among the holes. A combination of perfectly stirred reactors, plug flow reactors and mixers were utilized for modeling of the reactor network.



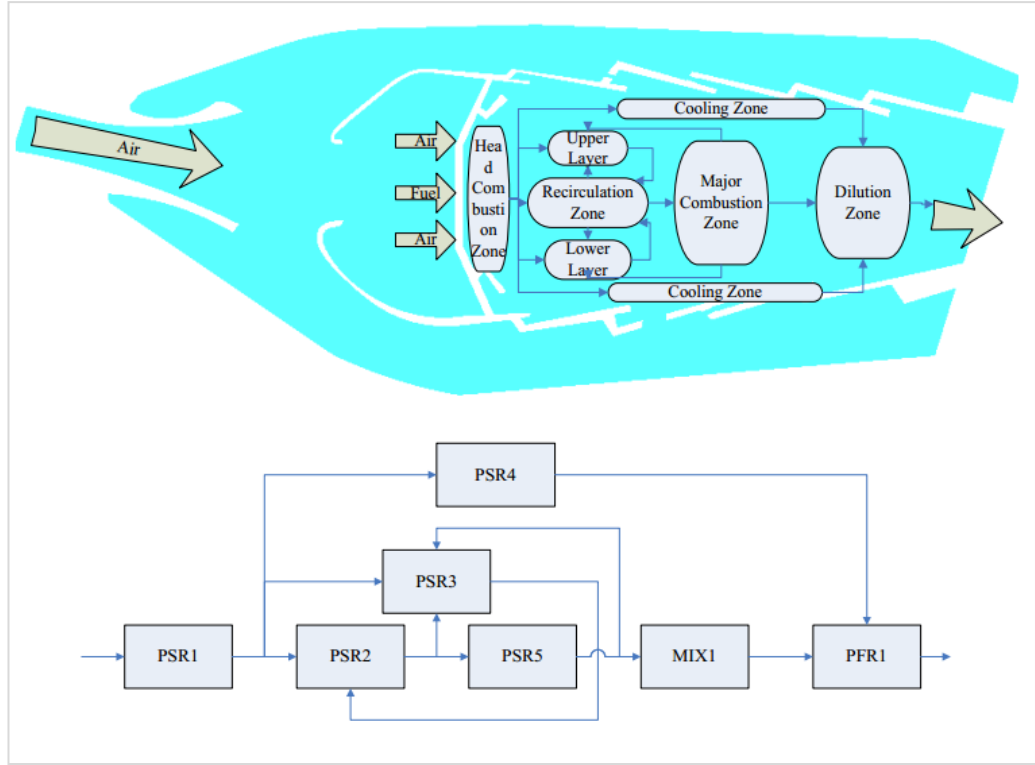


**Figure 1.2** - CRN model of Chen et al. [21]

A CRN application on lean-premixed burners and two phase combustion inside wood dust burners was performed by Novosselov [22]. NO<sub>x</sub> and CO emissions were investigated in the study and a coupled CFD and reactor network approach with a detailed chemistry was used. Another study on emission predictions in preliminary combustor design step was conducted by Rezvani [23]. The study combined the basic flow distribution and CRN together. The flow distribution calculates the flow split according to the on-design and off-design conditions. The model also included the effect of evaporation and diffusion of the fuel. While carefully setting the pre-reactor conditions in detail, CRN were created in a zonal approach with high number of reactors. The emission results were verified with the Rich-Quench-Lean (RQL) combustor data. An Equivalent Reactor Network (ERN) was presented by Drennan et al [24], this work distinguished from other CFD methods in terms of its reactor network forming algorithm. A reactor network of the combustor domain was formed by applying a group of filters to the detailed CFD solution. This approach created a complete 0-D mimic of the combustor and this model enabled to obtain better

emission predictions without calculating the CFD solution of whole combustor domain.

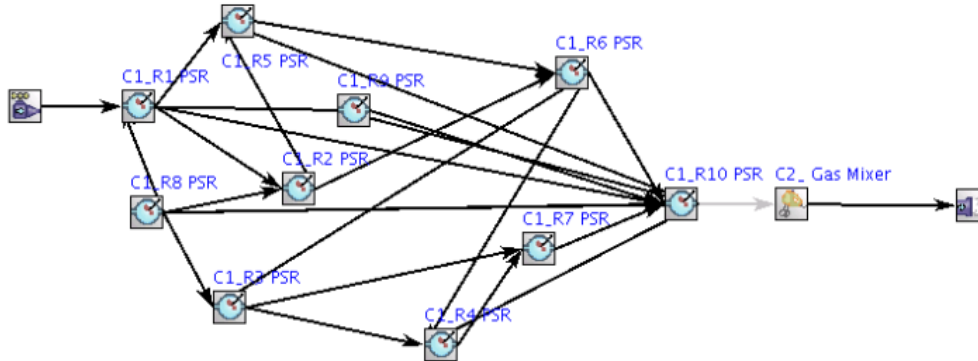


**Figure 1.3** - ERN Model of Drennan et al. [24]

A novel CRN model was developed by Xu et al [25]. The model principally included all the features for CRN modeling of a combustor, it also took the evaporation and mixing degree into consideration and model was applied to the lean premixed pre-vaporized combustor. Nilsson [26] focused on developing CRN model on a pre-calculated CFD solution. The significant important part of the study was utilization of different algorithms for formation of the network.

## 1.2 Theory

### 1.2.1 Flow and Chemical Reactor Network Equations

#### 1.2.1.1 Flow Equations

In order to solve the flow network fundamental equations for single-phase compressible flow are written for two sections shown in Figure 1.4 - (a.) [5]. The flow parameters are assumed to be calculated isothermally during the current calculation.

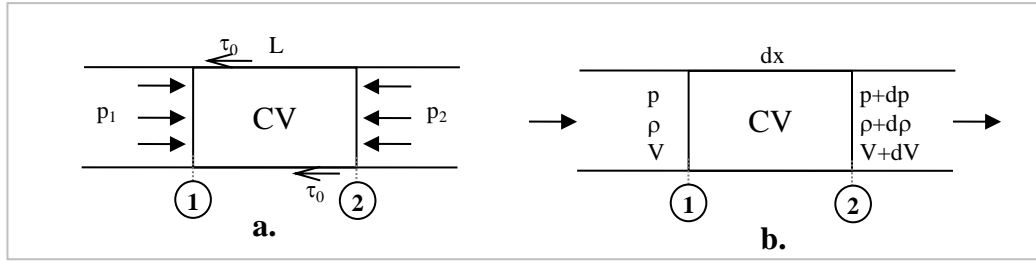


**Figure 1.4 - A pipe element**

continuity:  $\rho_1 V_1 A_1 = \rho_2 V_2 A_2 = \text{const.}$  (1)

energy:  $\frac{V_1^2}{2} + \frac{P_1}{\rho_1} + gz_1 = \frac{V_2^2}{2} + \frac{P_2}{\rho_2} + gz_2 + hf$  (2)

momentum:  $F = \rho_2 V_2^2 A_2 - \rho_1 V_1^2 A_1$  (3)

By writing the right hand side of the momentum equation and neglecting the small terms, following equation is obtained,

$$F = (\rho + d\rho)(V + dV)^2 A - \rho V^2 A \quad (4)$$

$$F = A(2\rho V dV + V^2 d\rho) \quad (5)$$

By writing the left hand side of the momentum equation and neglecting the small terms, following equation is obtained,

$$F = pA - (p + dp)A - \tau_0 \pi D dx = -Adp - \tau_0 \pi D dx \quad (6)$$

$$F = -Adp - \tau_0 \pi D dx \quad (7)$$

Combining momentum equation together by equating (5) and (7),

$$2\rho V dV + V^2 d\rho + dP + \frac{4\tau_0 dx}{D} = 0 \quad (8)$$

When the pipe element is straight and has a constant diameter, furthermore with an incompressible assumption at this step only. The energy and momentum equations can be written as follows,

$$\text{energy: } \frac{P_1}{\rho g} - \frac{P_2}{\rho g} = hf = f \frac{L}{D} \frac{V^2}{2g} \quad (9)$$

$$\text{momentum: } F = (P_1 - P_2)A - \tau_0 \pi DL = 0 \quad (10)$$

If momentum equation is rearranged Equation (10) can be obtained.

$$\tau_0 = \frac{(P_1 - P_2)A}{\pi DL} = \frac{(P_1 - P_2)D}{4L} \quad (11)$$

By putting equation (9) into equation (10), following equation for the shear is obtained.

$$\tau_0 = \frac{f\rho V^2}{8} \quad (12)$$

If equation (11) is inserted into equation (8) following form of the compressible flow equation will be obtained.

$$2VdV + V^2 \frac{d\rho}{\rho} + \frac{dP}{\rho} + \frac{fV^2 dx}{2D} = 0 \quad (13)$$

If continuity equation (1) is differentiated for constant area;

$$\frac{dV}{V} + \frac{d\rho}{\rho} = 0 \quad (14)$$

The final form of the compressible flow equation along a pipe element is obtained by inserting equation (14) into equation (13).

$$\frac{dV}{V} + \frac{dP}{\rho V^2} + \frac{f dx}{2D} = 0 \quad (15)$$

Because the exact evaluation of the pressure integral is not possible in this form, a reversible idealization should be made for solution of the equation. In the context of this study only the isothermal and adiabatic idealizations will be utilized.

#### 1.2.1.2 Incompressible Extension of the Equations

Equation (15) can be simplified by assuming low pressure lines and constant density and takes the following form [9];

$$\frac{dP}{\rho V^2} + \frac{f dx}{2D} = 0 \quad (16)$$

Rearranging the equation (16) gives the following form,

$$\frac{dP}{dx} = -\frac{f \rho V^2}{2D} \quad (17)$$

$$P_1 - P_2 = \frac{fL}{D} \frac{\rho V^2}{2} \quad (18)$$

Equation (17) is simply the Darcy pressure loss equation.

#### 1.2.1.3 Compressible Extension of the Equations

Isothermal extension of the pipe equation can be obtained by using the following assumptions. The ideal gas equation is given in equation (19).

$$p = \rho RT \quad (19)$$

Note that  $RT$  is constant.

$$\frac{p}{\rho} = \frac{p_1}{\rho_1} = c \quad (20)$$

$$\frac{\rho_1}{\rho} = \frac{p_1}{p} \quad (21)$$

Furthermore from continuity equation,

$$\rho V = \rho_1 V_1 \quad (22)$$

$$\frac{\rho_1}{\rho} = \frac{V}{V_1} \quad (23)$$

By inserting equation (21) into equation (23), following equation is obtained.

$$\begin{aligned} \frac{p_1}{p} &= \frac{V}{V_1} \\ pV &= p_1 V_1 = \text{const.} \end{aligned} \quad (24)$$

From equation (24)

$$\rho V^2 = \frac{\rho_1^2 V_1^2}{\rho} \quad (25)$$

Dividing  $dp$  by  $\rho V^2$ , and by utilizing equation (25)

$$\frac{dp}{\rho V^2} = \frac{\rho dp}{\rho_1^2 V_1^2} = \frac{p dp}{(\rho_1 V_1)(p_1 V_1)} \quad (26)$$

Equation (15) can be rewritten by using equation (23), notice that  $\rho_1 V_1$  and  $p_1 V_1$  terms are constant.

$$\frac{dV}{V} + \frac{pdp}{(\rho_1 V_1)(p_1 V_1)} + \frac{f dx}{2D} = 0 \quad (27)$$

Integrating the main equation gives the following final form for the compressible isothermal pipe flow.

$$p_1^2 - p_2^2 = \rho_1 p_1 V_1^2 \left[ 2 \ln \frac{V_2}{V_1} + \frac{f l}{D} \right] \quad (28)$$

#### 1.2.1.4 Reactor Theory

A general perfectly stirred reactor (PSR) model of CANTERA [27] is utilized in this study. A 0D reactor is a system which has one or more inlet and an exit. For the reactor the general state variables are the mass inside the reactor, the reactor volume, total internal energy of the contents and the mass fraction of the contents. The fundamental equations for determining the state inside the reactor are mass conservation equation, species conservation equation and energy conservation equation. These equations are given in equations (29)-(31) in order [27].

$$\frac{dm}{dt} = \sum_{in} \dot{m}_{in} - \sum_{out} \dot{m}_{out} \quad (29)$$

$$\frac{d(mY_k)}{dt} = \sum_{in} \dot{m}_{in} Y_{k,in} - \sum_{out} \dot{m}_{out} Y_k + \dot{m}_{k,gen} \quad (30)$$

$$\frac{d(U)}{dt} = -P \frac{dV}{dt} - \dot{Q} + \sum_{in} \dot{m}_{in} h_{in} - h \sum_{out} \dot{m}_{out} \quad (31)$$

#### 1.2.2 CFD Theory

CFD equations that belong to the models used in this thesis are described in this section. Firstly, the general equations of fluid motion, simply the Navier-Stokes equations, are described. Secondly, RANS (Reynolds Average Navier-Stokes) and SAS (Scale Adaptive Simulation) processing of these equations are mentioned [37].

Finally the combustion CFD theory which is Non-premixed combustion model is described [41].

### 1.2.2.1 General Equations of Fluid Motion

General equation of fluid motion which are Navier-Stokes Equations can be written in open form in equations (32)-(34).

$$\begin{aligned} \rho \frac{Du}{Dt} = & -\frac{\partial p}{\partial x} + \frac{\partial}{\partial x} \left[ 2\mu \frac{\partial u}{\partial x} + \lambda(\nabla \cdot V) \right] + \frac{\partial}{\partial y} \left[ \mu \left( \frac{\partial u}{\partial y} + \frac{\partial v}{\partial x} \right) \right] + \\ & \frac{\partial}{\partial z} \left[ \mu \left( \frac{\partial u}{\partial z} + \frac{\partial w}{\partial x} \right) \right] + S_{Mx} \end{aligned} \quad (32)$$

$$\begin{aligned} \rho \frac{Dv}{Dt} = & -\frac{\partial p}{\partial y} + \frac{\partial}{\partial x} \left[ \mu \left( \frac{\partial u}{\partial y} + \frac{\partial v}{\partial x} \right) \right] + \frac{\partial}{\partial y} \left[ 2\mu \frac{\partial v}{\partial y} + \lambda(\nabla \cdot V) \right] + \\ & \frac{\partial}{\partial z} \left[ \mu \left( \frac{\partial v}{\partial z} + \frac{\partial w}{\partial y} \right) \right] + S_{My} \end{aligned} \quad (33)$$

$$\begin{aligned} \rho \frac{Dw}{Dt} = & -\frac{\partial p}{\partial z} + \frac{\partial}{\partial x} \left[ \mu \left( \frac{\partial u}{\partial z} + \frac{\partial w}{\partial x} \right) \right] + \frac{\partial}{\partial y} \left[ \mu \left( \frac{\partial v}{\partial z} + \frac{\partial w}{\partial y} \right) \right] + \\ & \frac{\partial}{\partial z} \left[ 2\mu \frac{\partial w}{\partial z} + \lambda(\nabla \cdot V) \right] + S_{Mz} \end{aligned} \quad (34)$$

By rearranging the equations the following form shown in equation (35) can be obtained, notice that this form is given only for x direction.

$$\begin{aligned} \rho \frac{Du}{Dt} = & -\frac{\partial p}{\partial x} + \frac{\partial}{\partial x} \left( \mu \frac{\partial u}{\partial x} \right) + \frac{\partial}{\partial y} \left( \mu \frac{\partial u}{\partial y} \right) + \frac{\partial}{\partial z} \left( \mu \frac{\partial u}{\partial z} \right) + \\ & \left[ \frac{\partial}{\partial x} \left( \mu \frac{\partial u}{\partial x} \right) + \frac{\partial}{\partial y} \left( \mu \frac{\partial v}{\partial x} \right) + \frac{\partial}{\partial z} \left( \mu \frac{\partial w}{\partial x} \right) \right] + S_{Mx} \\ & + \frac{\partial}{\partial x} (\lambda(\nabla \cdot V)) \end{aligned} \quad (35)$$

In equation (35), the terms in parenthesis disappear for the incompressible N-S equations by using mass flow conservation. However for the general usage these



terms are put into the momentum source terms and the final closed form of the generalized N-S equations for Newtonian fluids are obtained.

The closed form of the equations is also shown in equations (36)-(38).

$$\rho \frac{Du}{Dt} = \rho \frac{\partial u}{\partial t} + (\nabla \cdot uv) = -\frac{\partial p}{\partial x} + \nabla \cdot (\mu \nabla u) + S_{Mx} \quad (36)$$

$$\rho \frac{Dv}{Dt} = \rho \frac{\partial v}{\partial t} + (\nabla \cdot v\mathbf{v}) = -\frac{\partial p}{\partial y} + \nabla \cdot (\mu \nabla v) + S_{My} \quad (37)$$

$$\rho \frac{Dw}{Dt} = \rho \frac{\partial w}{\partial t} + (\nabla \cdot w\mathbf{v}) = -\frac{\partial p}{\partial z} + \nabla \cdot (\mu \nabla w) + S_{Mz} \quad (38)$$

### 1.2.2.2 Reynolds-Averaged Navier-Stokes Equations

For turbulent flow, the flow variables can be written as mean and fluctuating components, given in equations (39)-(43).

$$\mathbf{v} = \mathbf{V} + \mathbf{v}' \text{ (Total Velocity Vector)} \quad (39)$$

$$u = U + u' \quad (40)$$

$$v = V + v' \quad (41)$$

$$w = W + w' \quad (42)$$

$$p = P + p' \quad (43)$$

Some important time averaged terms are given in equations (44)-(47) [37];

$$\overline{\frac{\partial u}{\partial t}} = \frac{\partial U}{\partial t} \quad (44)$$

$$\nabla \cdot (\overline{uv}) = \nabla \cdot (UV) + \nabla \cdot (\overline{u'v'}) \quad (45)$$

$$-\frac{1}{\rho} \overline{\frac{\partial p}{\partial x}} = -\frac{1}{\rho} \frac{\partial P}{\partial x} \quad (46)$$

$$\overline{\nu \nabla \cdot (\nabla u)} = \nu \nabla \cdot (\nabla U) \quad (47)$$

Using these time averaged terms, the time averaged version of the Navier-Stokes Equations can be obtained.

$$\frac{\partial U}{\partial t} + \nabla \cdot (UV) + \nabla \cdot (\overline{u'v'}) = -\frac{1}{\rho} \frac{\partial P}{\partial x} + \nu \nabla \cdot (\nabla U) + S_{Mx} \quad (48)$$

$$\frac{\partial V}{\partial t} + \nabla \cdot (VV) + \nabla \cdot (\overline{v'v'}) = -\frac{1}{\rho} \frac{\partial P}{\partial y} + \nu \nabla \cdot (\nabla V) + S_{My} \quad (49)$$

$$\frac{\partial W}{\partial t} + \nabla \cdot (WV) + \nabla \cdot (\overline{w'v'}) = -\frac{1}{\rho} \frac{\partial P}{\partial z} + \nu \nabla \cdot (\nabla W) + S_{Mz} \quad (50)$$

Fluctuating velocity terms in the above equation come as a result of the time averaging process. These fluctuating terms are related with convective transport of momentum due to small eddies. If these terms are put into the right hand side and are expanded, the following form of the Reynold's Averaged Navier-Stokes Equations are obtained.

$$\begin{aligned} \frac{\partial U}{\partial t} + \nabla \cdot (UV) = & -\frac{1}{\rho} \frac{\partial P}{\partial x} + \nu \nabla \cdot (\nabla U) + \\ & \frac{1}{\rho} \left[ \frac{\partial(-\overline{\rho u'^2})}{\partial x} + \frac{\partial(-\overline{\rho u'v'})}{\partial y} \frac{\partial(-\overline{\rho u'w'})}{\partial z} \right] + S_{Mx} \end{aligned} \quad (51)$$

$$\begin{aligned} \frac{\partial V}{\partial t} + \nabla \cdot (VV) = & -\frac{1}{\rho} \frac{\partial P}{\partial y} + \nu \nabla \cdot (\nabla V) + \\ & \frac{1}{\rho} \left[ \frac{\partial(-\overline{\rho u'v'})}{\partial x} + \frac{\partial(-\overline{\rho v'^2})}{\partial y} \frac{\partial(-\overline{\rho v'w'})}{\partial z} \right] + S_{My} \end{aligned} \quad (52)$$

$$\begin{aligned} \frac{\partial W}{\partial t} + \nabla \cdot (WV) = & -\frac{1}{\rho} \frac{\partial P}{\partial z} + \nu \nabla \cdot (\nabla W) + \\ & \frac{1}{\rho} \left[ \frac{\partial(-\overline{\rho u'w'})}{\partial x} + \frac{\partial(-\overline{\rho v'w'})}{\partial y} \frac{\partial(-\overline{\rho w'^2})}{\partial z} \right] + S_{Mz} \end{aligned} \quad (53)$$

The stress terms reflecting the turbulent character of the flow field they are namely called Reynolds Stresses and are given as follows;

$$\text{Normal Stresses: } \tau_{xx} = -\overline{\rho u'^2}, \tau_{yy} = -\overline{\rho v'^2}, \tau_{zz} = -\overline{\rho w'^2} \quad (54)$$

$$\text{Shear Stresses: } \tau_{xy} = \tau_{yx} = -\overline{\rho u'v'}, \tau_{xz} = \tau_{zx} = -\overline{\rho u'w'}, \tau_{yz} = \tau_{zy} = -\overline{\rho v'w'} \quad (55)$$

Using Boussinesq approximation Reynolds stresses can be written proportional to the mean rates of deformation;

$$\tau_{ij} = -\overline{\rho u'_i u'_j} = \mu_t \left( \frac{\partial U_i}{\partial x_j} + \frac{\partial U_j}{\partial x_i} \right) - \frac{2}{3} \rho k \delta_{ij} \quad (56)$$

$k = \frac{1}{2} (\overline{u'^2} + \overline{v'^2} + \overline{w'^2})$  is the turbulent kinetic energy and  $\mu_t$  is eddy viscosity.

### 1.2.2.3 k-ε turbulence model

k-ε turbulent model is basically used for calculation of the Reynolds Stress terms in RANS equations. They are solved by using the Boussinesq approximation and they are function of the rate of deformation ( $S_{ij}$ ), turbulence kinetic energy ( $k$ ), the rate of dissipation of turbulent kinetic energy ( $\varepsilon$ ) and density ( $\rho$ ).

$$\tau_{ij} = -\overline{\rho u'_i u'_j} = \tau_{ij}(S_{ij}, k, \varepsilon, \rho) \quad (57)$$

The model is based on the changes in the turbulent kinetic energy. Instantaneous kinetic energy can be written as follows; similar to the velocity components, the instantaneous kinetic energy is composed of a mean kinetic energy term and a turbulent kinetic energy term as given in equation (58).

$$k(t) = K + k \quad (58)$$

$$K = \frac{1}{2} (U^2 + V^2 + W^2) \quad (59)$$

$$k = \frac{1}{2} (\overline{u'^2} + \overline{v'^2} + \overline{w'^2}) \quad (60)$$

The rate of deformation ( $S_{ij}$ ) can be obtained by decomposition of the deformation of a fluid element, it can also be written as a sum of the mean and fluctuating components.

$$s_{xx}(t) = S_{xx} + s'_{xx} = \frac{\partial U}{\partial x} + \frac{\partial u'}{\partial x} \quad (61)$$

$$s_{yy}(t) = S_{yy} + s'_{yy} = \frac{\partial V}{\partial y} + \frac{\partial v'}{\partial y} \quad (62)$$

$$s_{zz}(t) = S_{zz} + s'_{zz} = \frac{\partial W}{\partial z} + \frac{\partial w'}{\partial z} \quad (63)$$

$$s_{xy}(t) = s_{yx}(t) = S_{xy} + s'_{xy} = \frac{1}{2} \left( \frac{\partial U}{\partial y} + \frac{\partial V}{\partial x} \right) + \frac{1}{2} \left( \frac{\partial u'}{\partial y} + \frac{\partial v'}{\partial x} \right) \quad (64)$$

$$s_{xz}(t) = s_{zx}(t) = S_{xz} + s'_{xz} = \frac{1}{2} \left( \frac{\partial U}{\partial z} + \frac{\partial W}{\partial x} \right) + \frac{1}{2} \left( \frac{\partial u'}{\partial z} + \frac{\partial w'}{\partial x} \right) \quad (65)$$

$$s_{yz}(t) = s_{zy}(t) = S_{yz} + s'_{yz} = \frac{1}{2} \left( \frac{\partial V}{\partial z} + \frac{\partial W}{\partial y} \right) + \frac{1}{2} \left( \frac{\partial v'}{\partial z} + \frac{\partial w'}{\partial y} \right) \quad (66)$$

A governing equation for the mean kinetic energy can be written by using the Reynold's Averaged Navier-Stokes equation [37];

$$\frac{\partial(\rho K)}{\partial t} + \nabla \cdot (\rho K \mathbf{V}) = \nabla \cdot (-P\mathbf{V} + 2\mu \nabla S_{ij} - \rho \overline{\mathbf{V} u'_i u'_j}) - 2\mu S_{ij} \cdot S_{ij} + \overline{\rho u'_i u'_j} \cdot S_{ij} \quad (67)$$

Another equation for the turbulent kinetic energy can be written by using the Reynold's Averaged Navier-Stokes equation [37];

$$\begin{aligned} \frac{\partial(\rho k)}{\partial t} + \nabla \cdot (\rho k \mathbf{V}) = & \nabla \cdot (-\overline{p' \mathbf{v}'} + 2\mu \overline{\mathbf{v}' s'_{ij}} - \frac{1}{2} \overline{\rho u'_i u'_i u'_j}) - 2\mu \overline{s'_{ij} \cdot s'_{ij}} + \\ & \overline{\rho u'_i u'_j} \cdot S_{ij} \end{aligned} \quad (68)$$

Although the two equations for mean kinetic energy and the turbulent kinetic energy seems similar in principle, the turbulent kinetic energy equation includes the

fluctuating velocity terms which implies that the change in turbulent kinetic energy is mainly governed by the turbulent interactions.

An important term in the turbulent kinetic energy equation is the viscous dissipation term which represents the dissipation of turbulent kinetic energy as a result of the velocity fluctuations (small eddies). This term can be written as rate per unit mass terms as follows and the rate of dissipation  $\varepsilon$  can be written as follows [37];

$$\varepsilon = 2\nu \overline{s'_{ij} \cdot s'_{ij}} \quad (69)$$

The equation given above can be used to find the  $k$  value. Similarly an  $\varepsilon$  equation can be written. However the exact equations include many terms and some of those are unknowns throughout the flow field. In order to model those equations some simplified versions of them are developed.

The standard  $k$ - $\varepsilon$  model developed by Launder and Spalding includes two basic model equations for the transport of  $k$  and  $\varepsilon$ . The model begins with defining a velocity scale,  $\nu$ , and a length scale,  $\ell$  for the large scale turbulence.

$$\nu = k^{1/2} \quad (70)$$

$$\ell = \frac{k^{\frac{3}{2}}}{\varepsilon} \quad (71)$$

Then, the Eddy viscosity term in the Reynolds stress general equation can be written as;

$$\mu_t = C\rho\nu\ell = \rho C_\mu \frac{k^2}{\varepsilon} \quad (72)$$

The transport equations for  $k$  and  $\varepsilon$  are given in equation (73) and (74).

$$\frac{\partial(\rho k)}{\partial t} + \nabla \cdot (\rho k \mathbf{V}) = \nabla \cdot \left( \frac{\mu_t}{\sigma_k} \nabla k \right) + 2\mu_t S_{ij} \cdot S_{ij} - \rho \varepsilon \quad (73)$$

$$\frac{\partial(\rho \varepsilon)}{\partial t} + \nabla \cdot (\rho \varepsilon \mathbf{V}) = \nabla \cdot \left( \frac{\mu_t}{\sigma_\varepsilon} \nabla \varepsilon \right) + C_{1\varepsilon} \frac{\varepsilon}{k} 2\mu_t S_{ij} \cdot S_{ij} - C_{2\varepsilon} \rho \frac{\varepsilon^2}{k} \quad (74)$$

It should be reminded that the solution of these equations is used in Boussinesq relation to compute the Reynolds Stress terms given inside the RANS equations.

#### 1.2.2.4 Scale-Adaptive Simulation (SAS) Model

SAS model is the improved version of the unsteady RANS formulation. It allows the resolve the turbulent spectrum in unstable flow conditions. SAS model uses Von Karman length-scale to dynamically adjust to resolve structures in an unsteady RANS simulation, as a result the unsteady regions of the flow field shows LES like character. In order to achieve this character a source term is added to classical RANS turbulence model equations, this source term allows the model to adjust resolved scales during the simulation. In classical unsteady RANS, flow exhibits a single mode unphysical unsteady flow characteristics. SAS model physically split these large turbulent structures to smaller scales which are typical in a classical LES calculation.

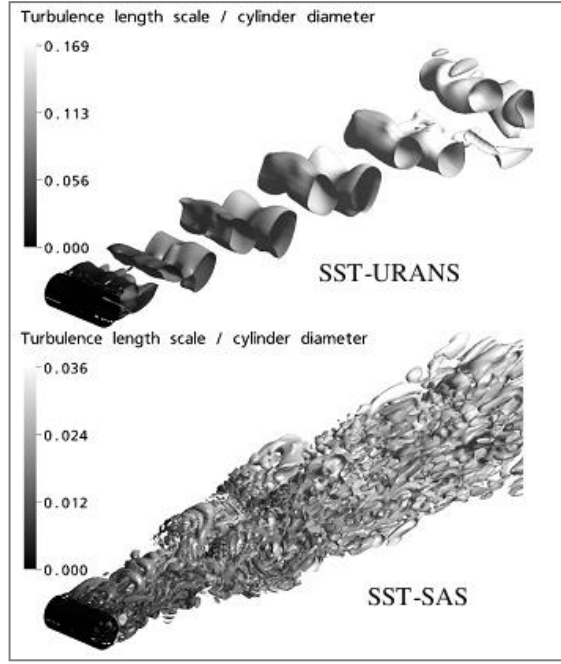


**Figure 1.5** – Comparison of SST-URANS with SST-SAS solutions for cylinder in cross flow [38]

The formulation of the SAS model based on the Menter's [38]  $k-\omega$  RANS turbulence model, so it is better to give the transport equation for the  $k-\omega$  model first.

$k-\omega$  model is also a 2-equation turbulence model.  $K$  is the turbulent kinetic energy as in  $k-\varepsilon$  turbulence model.  $\omega$  is named turbulent frequency and formulated as  $\omega = \varepsilon / k$ . The velocity and length scales in terms of these parameters are given in equations (75) and (76).

$$\nu = k^{1/2} \quad (75)$$

$$\ell = \frac{k^{1/2}}{\omega} \quad (76)$$

Again, the Reynolds stresses are calculated by using Boussinesq approximation. The transport equation of the  $k$  and  $\omega$  are given below. ( $\beta_1, \beta_2$  and  $\sigma_{\omega,1}$  are model constants.)

$$\frac{\partial(\rho k)}{\partial t} + \nabla \cdot (\rho k \mathbf{V}) = \nabla \cdot \left( \left( \mu + \frac{\mu_t}{\sigma_k} \right) \nabla k \right) + \left( 2\mu_t S_{ij} \cdot S_{ij} - \frac{2}{3} \rho k \frac{\partial U_i}{\partial x_j} \delta_{ij} \right) - \beta_1 \rho k \omega \quad (77)$$

$$\begin{aligned} \frac{\partial(\rho \omega)}{\partial t} + \nabla \cdot (\rho \omega \mathbf{V}) &= \nabla \cdot \left( \left( \mu + \frac{\mu_t}{\sigma_\omega} \right) \nabla \omega \right) + \left( 2\rho S_{ij} \cdot S_{ij} - \frac{2}{3} \rho \omega \frac{\partial U_i}{\partial x_j} \delta_{ij} \right) \\ &- \beta_2 \rho \omega^2 + \frac{2\rho}{\sigma_{\omega,1}} \frac{\partial k}{\partial x_k} \frac{\partial \omega}{\partial x_k} \end{aligned} \quad (78)$$

At this point  $\omega$  equation can be written for SAS model as in equation (79).

$$\begin{aligned} \frac{\partial(\rho \omega)}{\partial t} + \nabla \cdot (\rho \omega \mathbf{V}) &= \nabla \cdot \left( \left( \mu + \frac{\mu_t}{\sigma_\omega} \right) \nabla \omega \right) + \left( 2\rho S_{ij} \cdot S_{ij} - \frac{2}{3} \rho \omega \frac{\partial U_i}{\partial x_j} \delta_{ij} \right) \\ &- \beta_2 \rho \omega^2 + F \frac{2\rho}{\sigma_{\omega,1}} \frac{\partial k}{\partial x_k} \frac{\partial \omega}{\partial x_k} + Q_{SAS} \end{aligned} \quad (79)$$

$$Q_{SAS} = \max \left[ \rho \eta_1 \kappa S^2 \left( \frac{L}{L_{VK}} \right)^2 - C \frac{2\rho k}{\sigma_\Phi} \max \left( \frac{1}{\omega^2} \frac{\partial k}{\partial x_k} \frac{\partial \omega}{\partial x_k}, \frac{1}{k^2} \frac{\partial k}{\partial x_k} \frac{\partial \omega}{\partial x_k} \right), 0 \right] \quad (80)$$

$Q_{SAS}$  is a source term reflecting the SAS character, equation (80). The inspection of the source terms shows that it either goes to a finite number or 0. The  $L$  in the equation is the length scale of modeled turbulence and  $L_{VK}$  is Von Karman length scale.

$$L = \frac{\sqrt{k}}{(c_\mu^{1/4} \omega)} \quad (81)$$

$$L_{VK} = \max \left( \frac{\kappa S}{|U''|}, C_s \sqrt{\frac{\kappa \eta_2}{(\beta/c_\mu) - \alpha}} \cdot \Delta \right) \quad (82)$$

$$\Delta = \Omega_{CV}^{1/3}, S = \sqrt{2S_{ij} \cdot S_{ij}} \text{ and } |U''| = \sqrt{\sum \left( \frac{\partial^2 u_i}{\partial x_j \partial x_j} \right)^2} \quad (83)$$



In the above equation  $S$  is the scalar invariant of the strain rate tensor,  $\Delta$  is the grid cell size. Note that the structure of the Von Karman length scale formulation add up a grid size dependent limiter, this limiter is used to control the damping of the finest resolved turbulent structures created inside the domain.

### 1.2.2.5 Non-Premixed Combustion CFD Model

Fuel and oxidizer mixes after entering the domain in non-premixed combustion. Fluent supplies a special model for modeling non-premixed combustion which is based on the mixture fraction approach. Mixture fraction is the mass fraction of the burnt and unburnt fuel streams in all of the species. Mixture fraction is conserved as a scalar variable in the calculations, which simplifies the complex kinetics significant amount. In non-premixed combustion the species transport equation for each species is not solved. In turn, the mixture fraction among the domain is solved and the concentrations of the species are predicted from that data. In non-premixed combustion the interaction between turbulence and chemistry is solved by using PDF (probability density function) approach.

The mixture fraction can be written in terms of atomic mass fraction.

$$f = \frac{Z_i - Z_{i,ox}}{Z_{i,fuel} - Z_{i,ox}} \quad (84)$$

$f$ : mixture fraction  
 $Z_i$ : elemental mass fraction for element  $i$   
 $_{ox}$ : in oxidizer

If the diffusion coefficient is identical for all of the elements in the fuel then the definition of mixture fraction is unique for the whole system. If there is a secondary fuel stream flow into the system then the following equations should hold.

$$f_{fuel} + f_{secondary} + f_{ox} = 1 \quad (85)$$

$$f_{secondary} = p_{sec}(1 - f_{fuel}) \quad (86)$$

In equation (86),  $p_{sec}$  is the normalized mixture fraction for the second stream. It gets value between 0-1 as the primary fuel mixture fraction

In mixture fraction approach the species equation can be written for the mixture fraction. The assumption of having the same diffusivity for all of the species is an acceptable assumption for turbulent flows, in which the fluid flow by convection dominates the fluid movement by molecular diffusion. The distribution of density averaged mixture fraction is given in equation (87).

$$\frac{\partial(\rho \bar{f})}{\partial t} + \frac{\partial}{\partial x_i}(\rho u_i \bar{f}) = \frac{\partial}{\partial x_i} \left( \frac{\mu_t}{\sigma_t} \nabla \bar{f} \right) + S_m + S_{user} \quad (87)$$

$S_m$ : Source term for mass transfer from liquid droplets or solid reacting particles

$S_{user}$ : User defined source term

Conservation equation can also be written for the variance of the mixture fraction,  $\bar{f}'^2$ . Mixture fraction variance is used for the calculation of the turbulence – chemistry relation in non-premixed combustion model.

$$\frac{\partial(\rho \bar{f}'^2)}{\partial t} + \frac{\partial}{\partial x_i}(\rho u_i \bar{f}'^2) = \frac{\partial}{\partial x_i} \left( \frac{\mu_t}{\sigma_t} \nabla \bar{f}'^2 \right) + C_g \mu_t (\nabla \bar{f})^2 - C_d \rho \frac{\varepsilon}{k} \bar{f}'^2 + S_{user} \quad (88)$$

$$\bar{f}' = f - \bar{f} \quad (89)$$

$$\sigma_t = 0.85, C_g = 2.86, C_d = 2.0 \quad (90)$$

Mixture fraction can be written in terms of equivalence ratio, by this way the stoichiometric, lean or rich mixture modeling can be done.

$$f = \frac{\phi}{\phi + r} \quad (91)$$

r: air-fuel ration in mass terms

$$[\phi F + rO \rightarrow (\phi + r)P]$$

With an assumption of equilibrium species fraction, density and temperature are related to the mixture fraction. For a single mixture fraction and adiabatic system;

$$\phi_i = \phi_i(f) \quad (92)$$

For the system of two streams;

$$\phi_i = \phi_i(f_{fuel}, p_{sec}) \quad (93)$$

For non-adiabatic systems the equivalence ratio is a function mixture fraction and instantaneous enthalpy. Non adiabatic systems including the energy transfer from walls, discrete phase particles or droplets, inlets with different temperature.

$$\phi_i = \phi_i(f, H) \quad (94)$$

For the system of two streams;

$$\phi_i = \phi_i(f_{fuel}, p_{sec}, H) \quad (95)$$

In simulating of the non-equilibrium cases, Fluent offers three different model approaches.

- Rich Flammability Limit (RFL): Rich regions are modeled as a mixed but unburnt mixture of pure fuel and leaner equilibrium burnt mixture.
- Steady Laminar Flamelet model: chemical non-equilibrium can be modeled due to diffusion flame stretching by turbulence.
- Unsteady Laminar Flamelet model: slow forming product species which are far from the chemical equilibrium can be modeled.

## Modeling of Turbulence and Chemistry Interaction

### Probability Density Function

The probability density function,  $p(f)$ , describes the time fraction that spend in the vicinity of state  $f$ . For a point in the flow field the variation of mixture fraction with time is given on Figure 1.6. The value of the PDF function is also given on the left side of the graph.

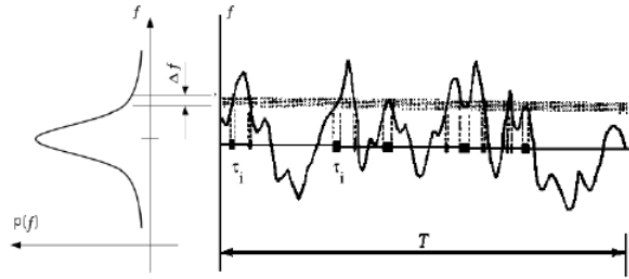


**Figure 1.6** – Graphical description of PDF function

Mathematically the PDF can be written as,

$$p(f)\Delta f = \lim_{T \rightarrow \infty} \frac{1}{T} \sum_i \tau_i \quad (96)$$

The above PDF equation tells that the total time spent for a specified value of  $f$  is equal to the area under the curve of PDF function.  $\tau_i$  term in the equation is the amount of time that spent in the value of  $f$  band.

Mean values for the scalars for a single mixture fraction system;

$$\bar{\phi}_i = \int_0^1 p(f)\phi_i(f)df \quad (97)$$

For the average density value,

$$\frac{1}{\bar{\rho}} = \int_0^1 \frac{p(f)}{\rho(f)} df \quad (98)$$

The shape of the PDF function is described in Fluent by two mathematical functions. The double delta function and the beta function. These functions are dependent on the mean mixture fraction and its variance.

For an equilibrium, adiabatic and single mixture fraction case; the mean temperature, density and species fraction are functions of  $\bar{f}$  and  $\bar{f}'^2$ . The values of these main parameters can be pre calculated and tabulated before the initiation of the analysis and can be called back when needed. This data is tabulated in look up tables. Utilization of this approach significantly reduces the computational time required.



## CHAPTER 2

### NUMERICAL MODELS

#### 2.1 Network Structure

Flow network mapping approach utilized in this study is based on the method described in Greyvenstein et al. [4]. In Figure 2.1, the network schematic for a small system is given.

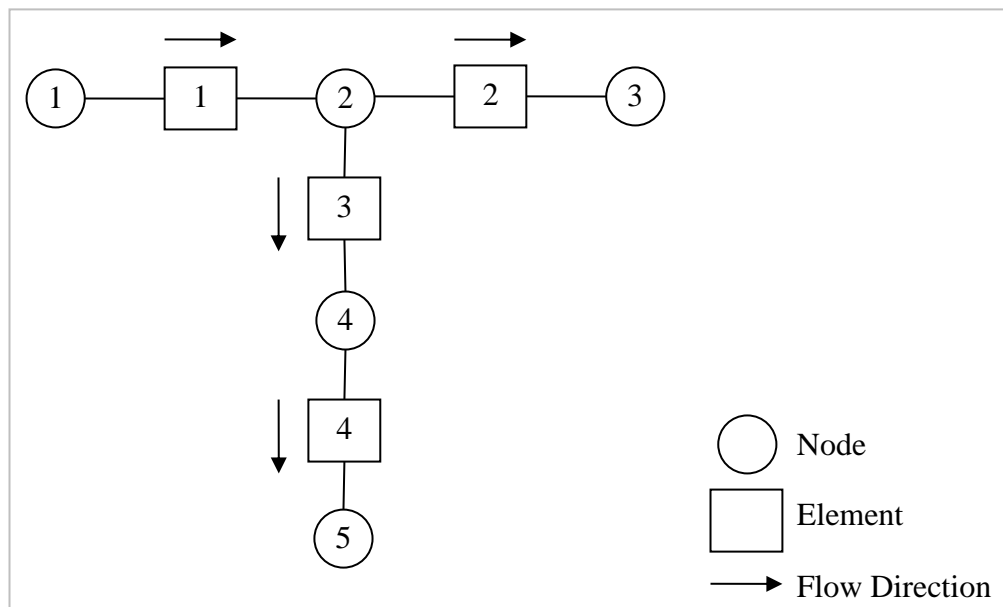


**Figure 2.1** - A sample flow network

Nodes are the element junctions and they are mainly used for storing the pressure data. Elements represent the “pipe” element itself; physically they keep the pipe diameter, length, friction factor, temperature, density, flow rate and any other pipe

related properties. As it can be understood from the figure, flow goes through the elements 1 - 2 and 1 - 3 - 4 both of these paths are active. For solution of the network system at least two boundary conditions are necessary, in the example system the boundary condition nodes are 1, 3 and 5. A general node and element matrix is written for the network, to define the element flow node relation during the calculations. The element and node matrix for the sample system shown in Figure 2.1 are given in equation (99).

$$N = \begin{bmatrix} 2 & 0 & 0 \\ 1 & 3 & 4 \\ 2 & 0 & 0 \\ 2 & 5 & 0 \\ 4 & 0 & 0 \end{bmatrix}, E = \begin{bmatrix} -1 & 0 & 0 \\ 1 & -2 & -3 \\ 2 & 0 & 0 \\ 3 & -4 & 0 \\ 4 & 0 & 0 \end{bmatrix} \quad (99)$$

Figure 2.2 shows a node - element representation for a single node connected to multiple elements. As it can be seen the subscript “i” indicates a node. And it is a global subscript throughout the network. Subscript “j” however is a local one, it indicates the elements connected to a specific node i.

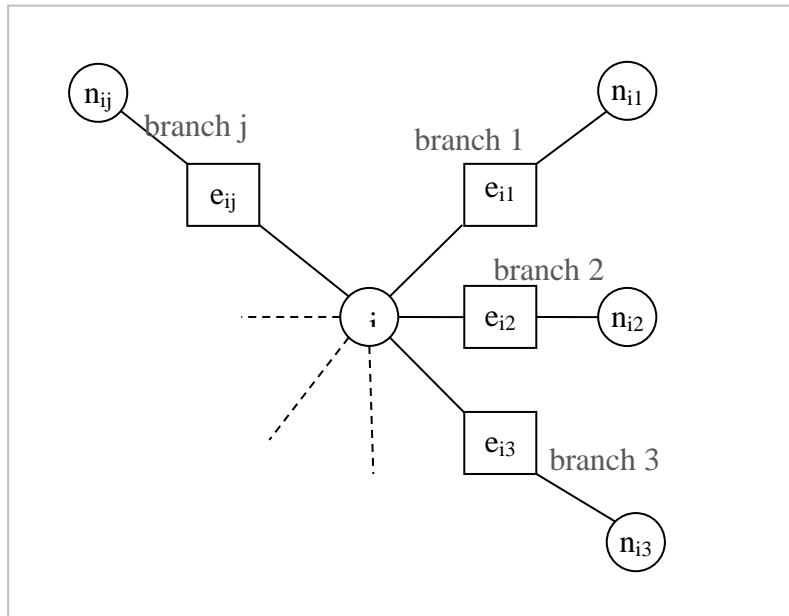


**Figure 2.2** - Notation used to define a network



Three different methods used in this study have distinct numerical solution characters.

## 2.2 Flow Models

### 2.2.1 Linear Method

Linear method is based on the form of the pressure loss equation given in equation (100). If this equation is rearranged for the flow rate, the following form is obtained.

$$Q_{ij} = \sqrt{\frac{P_{ni-1} - P_i}{\left(f_{ij} l_{ij} / d_{ij}\right) (\rho_{ij} \kappa_{ij})}} \quad (100)$$

$$\kappa_{ij} = \frac{8}{\pi^2 D^4} \quad (101)$$

By writing the continuity equation for a single node  $n_i$  which has an input branch element and an output branch element, equation (102) can be obtained. Renaming the constant terms as in equation (103) the final form can be solved iteratively for a system.

$$\frac{P_{ni-1} - P_i}{\sqrt{(P_{ni-1} - P_i) \left(f_{ij} l_{ij} / d_{ij}\right) (\rho_{ij} \kappa_{ij})}} - \frac{P_i - P_{ni+1}}{\sqrt{(P_i - P_{ni+1}) \left(f_{ij+1} l_{ij+1} / d_{ij+1}\right) (\rho_{ij+1} \kappa_{ij+1})}} = 0 \quad (102)$$

$$(P_{ni-1} - P_i) C_{ij} - (P_i - P_{ni+1}) C_{ij+1} = 0 \quad (103)$$

This form of the equation can be written for any network and can be solved with matrix methods. A general set of linear equations can be written as in equation (104).

$$\begin{bmatrix} C_{11} & C_{12} & C_{13} & C_{14} & \dots & C_{1j} \\ C_{21} & C_{22} & C_{23} & C_{24} & \dots & C_{2j} \\ C_{31} & C_{32} & C_{33} & C_{34} & \dots & C_{3j} \\ \dots & \dots & \dots & \dots & \dots & \dots \\ C_{i1} & C_{i2} & C_{i3} & C_{i4} & \dots & C_{ij} \end{bmatrix} \begin{bmatrix} P_1 \\ P_2 \\ P_3 \\ \dots \\ P_{ni} \end{bmatrix} = \begin{bmatrix} b_1 \\ b_2 \\ b_3 \\ \dots \\ b_{ni} \end{bmatrix} \quad (104)$$

This set of linear equations for the flow network system can be solved iteratively until convergence of the major parameters.

### 2.2.2 Segregated Method

This method is also based on the continuity and pressure drop equations [4].

$$\sum_{j=1}^J \rho_{ij} Q_{ij} s_{ij} = -d_i \quad (105)$$

$$\Delta P_{ij} = P_{nij} - P_i = s_{ij} H_{ij} g_{ij} f_{ij} \quad (106)$$

$$f_{ij} = K Q^2, \quad g_{ij} = \rho_{ij} \quad (107)$$

$d_i$  : is the external mass flow into the node i.

$s_{ij}$  : is a direction indicator of the flow inside the element it either gets 1 or -1.

$H_{ij}$  : is another flow direction indicator it counts the change of flow direction into consideration during the iterations.

$f_{ij}$  : is a function of flow rate,  $Q_{ij}$ , and for Darcy-Weisbach equation

$$f_{ij} = K Q^2 \quad (108)$$

$g_{ij}$  : is a function of density and for Darcy-Weisbach equation

$$g_{ij} = \rho_{ij} \quad (109)$$

Density for any element in the network is assumed to be the average of the two neighbor nodes,

$$\rho_{ij} = \frac{P_i + P_{nij}}{2} \frac{1}{RT_{ij}} \quad (110)$$

(49)

By defining  $a_{ij} = \frac{1}{2RT_{ij}}$ ,  $\rho_{ij}$  can be written as follows;

$$\rho_{ij} = a_{ij}(P_i + P_{nij}) \quad (111)$$

$$a_{ij} = \frac{1}{2RT_{ij}} \quad (112)$$

This method principally based on the SIMPLE algorithm of the Patankar and Spalding. By writing the correction equations for pressure, flow rate and density; the iteration rules can be written. Where \* is used for tentative values and ' is used for correction values [4].

$$P = P^* + P' \quad (113)$$

$$Q = Q^* + Q' \quad (114)$$

$$\rho = \rho^* + \rho' \quad (115)$$

The pressure loss equation (106) can be differentiated with respect to  $Q_{ij}$ ;

$$\Delta P_{ij} = P_{nij} - P_i = s_{ij} H_{ij} g_{ij} f_{ij} \quad (116)$$

$$\frac{\partial \Delta P_{ij}}{\partial Q_{ij}} = \frac{\partial P_{nij}}{\partial Q_{ij}} - \frac{\partial P_i}{\partial Q_{ij}} = s_{ij} H_{ij} G_{ij} f_{ij} \frac{\partial \rho_{ij}}{\partial Q_{ij}} + s_{ij} g_{ij} F_{ij} \quad (117)$$

Where;

$$G_{ij} = \frac{\partial g_{ij}}{\partial \rho_{ij}} \quad (118)$$

$$F_{ij} = \frac{\partial f_{ij}}{\partial |Q_{ij}|} \quad (119)$$

$$(56)$$

If differential terms are replaced by the correction terms;

$$\frac{P'_{nij}}{Q'_{ij}} - \frac{P'_i}{Q'_{ij}} = s_{ij} H_{ij} G_{ij} f_{ij} \frac{\rho'_{ij}}{\partial Q'_{ij}} + s_{ij} g_{ij} F_{ij} \quad (120)$$

The density correction can be written according to the pressure correction,

$$\rho'_{ij} = a_{ij} (P'_i + P'_{nij}) \quad (121)$$

If equation (121) is put into equation (120) a flow correction equation can be written:

$$Q'_{ij} = P'_{nij} \left[ \frac{1}{s_{ij} g_{ij}^* F_{ij}^*} - \frac{H_{ij} a_{ij} f_{ij}^* G_{ij}^*}{g_{ij}^* F_{ij}^*} \right] - P'_i \left[ \frac{1}{s_{ij} g_{ij}^* F_{ij}^*} + \frac{H_{ij} a_{ij} f_{ij}^* G_{ij}^*}{g_{ij}^* F_{ij}^*} \right] \quad (122)$$

Going back to the continuity equation, if flow and density terms in equation (105) are replaced by correction versions of equations (114) and (115);

$$\sum_{j=1}^J \rho_{ij} Q_{ij} s_{ij} = -d_i \quad (123)$$

$$\sum_{j=1}^J (\rho_{ij}^* Q_{ij}^* + \rho'_{ij} Q_{ij}^* + \rho_{ij}^* Q'_{ij} + \cancel{\rho'_{ij} Q'_{ij}}) s_{ij} = -d_i \quad (124)$$

Notice that the last term in parenthesis includes two correction terms, this term goes to zero as the iterations advances so it is omitted at this step.

If (121) and (122) are put into equation (124), the pressure correction equation is obtained as follows:

$$p_i' = \frac{\left[ \sum_{j=1}^J (c_{ij} P_{nij}') + b_i \right]}{c_{ii}} \quad (125)$$

$$c_{ii} = \sum_{j=1}^J \left[ \frac{\rho_{ij}^*}{g_{ij}^* F_{ij}^*} + s_{ij} H_{ij} a_{ij} \left( \frac{\rho_{ij}^* f_{ij}^* G_{ij}^*}{g_{ij}^* F_{ij}^*} - |Q_{ij}^*| \right) \right] \quad (126)$$

$$c_{ij} = \frac{\rho_{ij}^*}{g_{ij}^* F_{ij}^*} - s_{ij} H_{ij} a_{ij} \left( \frac{\rho_{ij}^* f_{ij}^* G_{ij}^*}{g_{ij}^* F_{ij}^*} - |Q_{ij}^*| \right) \quad (127)$$

$$b_i = d_i + \sum_{j=1}^J \rho_{ij}^* Q_{ij}^* s_{ij} \quad (128)$$

Equation (125) can be solved to find pressure correction at all nodes. Afterwards the pressure values are updated for the entire network. Next, flow correction equation (122) is solved and all flow values are updated and finally density correction equation (121) is solved for the entire elements and density values are updated. This procedure is carried on until convergence is achieved [4]. The convergence criteria for the network flow model are based on the convergence of the mass flows of the elements and the pressure values of the nodes. The mass flow convergence criterion is given in equation (129) [4].

$$\mathcal{E}_m = \frac{|h_i|_{\max}}{m_{mean}} \quad (129)$$

In equation (129),  $m_{mean}$  is the absolute of the maximum mass flow values of all the elements.  $|h_i|_{\max}$  is the maximum total net flow of every node.  $|h_i|_{\max}$  term is also given in equation (130).

$$|h_i|_{\max} = \sum_{j=1}^J (\rho_{ij} Q_{ij} s_{ij}) + d_i \quad (130)$$

A convergence parameter  $\varepsilon_p$  can be used to check the convergence of the pressure values. The pressure convergence criterion is given in equation (131). In the equation  $\Delta P_1$  is the pressure drop calculated by using the pressure loss equation and  $\Delta P_2$  is the pressure drop calculated by taking the difference of the two nodes connected to each element. The maximum value of  $\varepsilon_p$  is considered for each iteration.

$$\varepsilon_p = \sum_1^J \left| \frac{\Delta P_1 - \Delta P_2}{\Delta P_1} \right| \quad (131)$$

The convergence of the parameters  $\varepsilon_m$  and  $\varepsilon_p$  are followed during the iterations and iterations are continue until these parameters drop below  $10^{-3}$ .

The solution procedure for the segregated method is summarized in Figure 2.3.

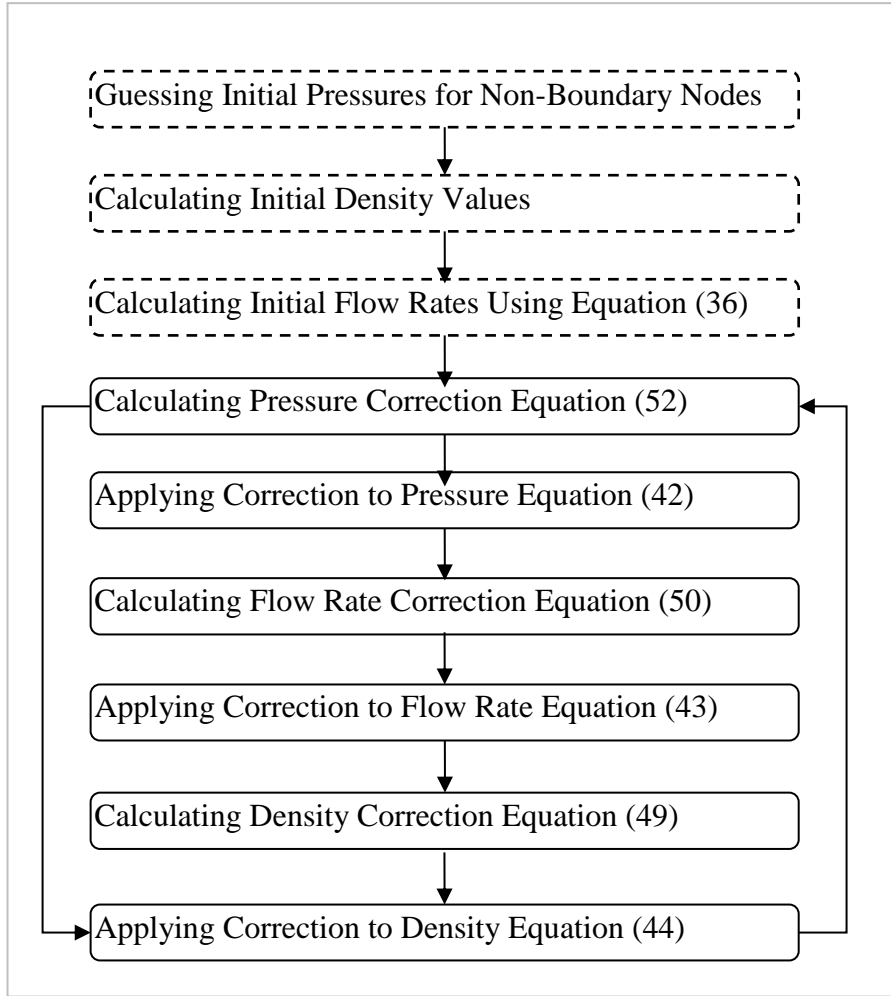


**Figure 2.3** -The Iteration Steps of the Pressure Corrector Scheme

### 2.2.3 Non-linear Method

Non-linear method is based on the form of the pressure loss equation given in equation (28). Pressure loss equation can be written as in equation (132) and rearranged to yield equation (133).

$$P_i^2 - P_{ni+1}^2 = \rho_{ij} P_{ij} V_{ij}^2 \left[ 2 \ln \frac{V_{ni+1}}{V_i} + \frac{f_{ij} l_{ij}}{d_{ij}} \right] \quad (132)$$

$$F_i(P_i, P_{ni+1}) = P_i^2 - P_{ni+1}^2 - C_{ij} Q_{ij}^2 \quad (133)$$

Furthermore, mass flow conservation is written for the nodes of the system as in equation (134). The mass flow equation includes the mass flow incoming to the node, mass flow outgoing from the node and external mass flow to the node.

$$F_i(Q_{ij}, Q_{ij+1}, ws) = ws + \rho_{ij}Q_{ij} - \rho_{ij+1}Q_{ij+1} \quad (134)$$

The equations to solve the network system are the pressure drop equations and the mass flow equations. These equations are listed in  $\hat{F}$  and the following set of equations is obtained in matrix form.

[illegible]

Notice that  $\hat{x}$  is an unknown matrix that is composed of all unknown pressures and flows values. In order to solve this set of equations, Newton-Raphson method can be applied to  $\hat{F}$  as in equation (136).

$$\hat{x}_{new} = \hat{x}_{old} - \hat{J}^{-1} \cdot \hat{F}(\hat{x}_{old}) \quad (136)$$

Notice that  $J$  is the Jacobian of the F matrix. The elements of the Jacobian matrix are the partial derivatives of the F equations for each unknown pressure and flow parameters.



$$\hat{J} = \begin{bmatrix} \frac{\partial F_1}{\partial P_1} & \cdots & \frac{\partial F_1}{\partial P_{ni}} & \frac{\partial F_1}{\partial Q_1} & \cdots & \frac{\partial F_1}{\partial Q_{ij}} \\ \frac{\partial F_2}{\partial P_1} & \cdots & \frac{\partial F_2}{\partial P_{ni}} & \frac{\partial F_2}{\partial Q_1} & \cdots & \frac{\partial F_2}{\partial Q_{ij}} \\ \frac{\partial F_3}{\partial P_1} & \cdots & \frac{\partial F_3}{\partial P_{ni}} & \frac{\partial F_3}{\partial Q_1} & \cdots & \frac{\partial F_3}{\partial Q_{ij}} \\ \cdots & & & & & \\ \frac{\partial F_n}{\partial P_1} & & \frac{\partial F_n}{\partial P_{ni}} & \frac{\partial F_n}{\partial Q_1} & \cdots & \frac{\partial F_n}{\partial Q_{ij}} \end{bmatrix} \quad (137)$$



## **CHAPTER 3**

### **NETWORK MODEL COMBUSTOR APPLICATION**

#### **3.1 Combustor Network Model**

A network model is prepared for an experimental combustor developed in TEI which is shown in Figure 3.1. TEI combustor is a through flow type combustor. The combustor has a pressure swirler structure at the liner front; this structure contains primary and secondary swirler holes. There are also other hole groups on the combustor liner; these are primary hole group, secondary hole group, dilution-1 hole group and dilution-2 hole group. The holes at the swirler structure and the liner are assigned hole elements on the network model. The name of the holes and the corresponding elements are given on Table 1. In the network model, elements also represent other flow regions. These regions are annulus and liner sections. The incoming air flow from element-1 distributed across the annulus elements of the combustor, pass through the hole elements and goes through the liner elements and left the system by the element-31.

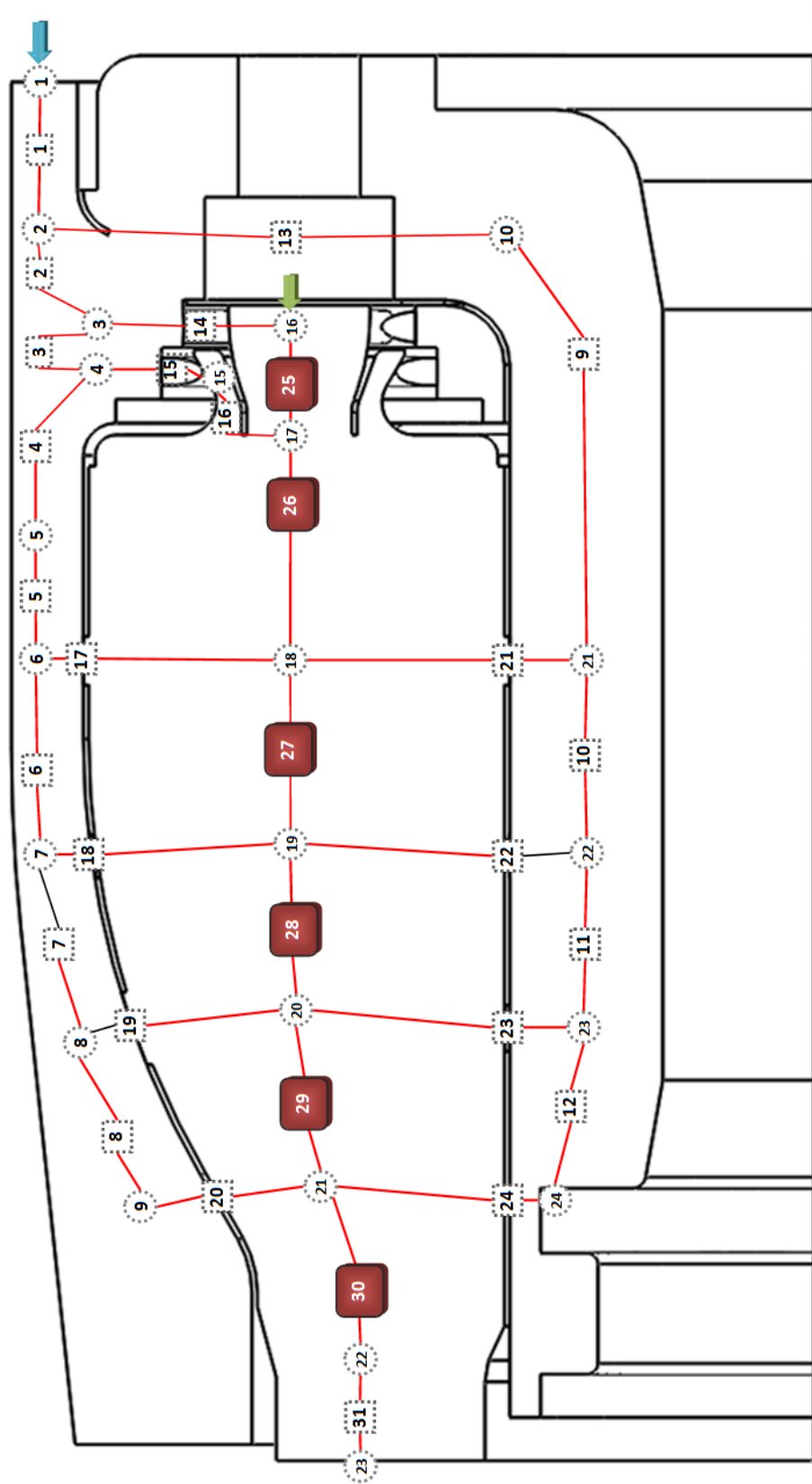


**Figure 3.1** - Network map of the combustor

**Table 3.1** – Hole element numbers and their corresponding location

<b>Element #</b>	<b>Hole Name</b>	<b>Region</b>
<b>14</b>	Primary	Swirler
<b>15</b>	Secondary	Swirler
<b>17</b>	Primary	Outer
<b>18</b>	Secondary	Outer
<b>19</b>	Dilution-1	Outer
<b>20</b>	Dilution-1	Outer
<b>21</b>	Primary	Inner
<b>22</b>	Secondary	Inner
<b>23</b>	Dilution-1	Inner
<b>24</b>	Dilution-2	Inner

Liner elements which are the elements between 25 to 30 are represented with a red frame around are reactor elements. The solution of the flow system gives out information about the pressure-flow-density information for the whole flow field. Afterwards, reactor elements get flow information from the flow network system and calculate the chemical reactor network. Fuel is injected from the node-16 to the element-25 which is also the beginning of the reactor network. Other elements are fed from the previous reactor and hole flow elements.

A general solution procedure is explained in Figure 5. As can be seen from the figure the solution begins with initiation of the model with the initial flow values. Constant loss terms are then calculated using the available geometric data. As the solution proceeds distribution of the flow field, pressure and density throughout the domain is obtained. By re-calculating the constant loss terms second main iteration is initiated. After the convergence, the last main iteration begins in which the reactors are activated. Reactors supply the temperature, density and species concentration data at the corresponding elements. After CRN computation, temperature and density values

are assigned to the related elements and recalculation begins. By the end of the third main loop, the final solution is obtained.

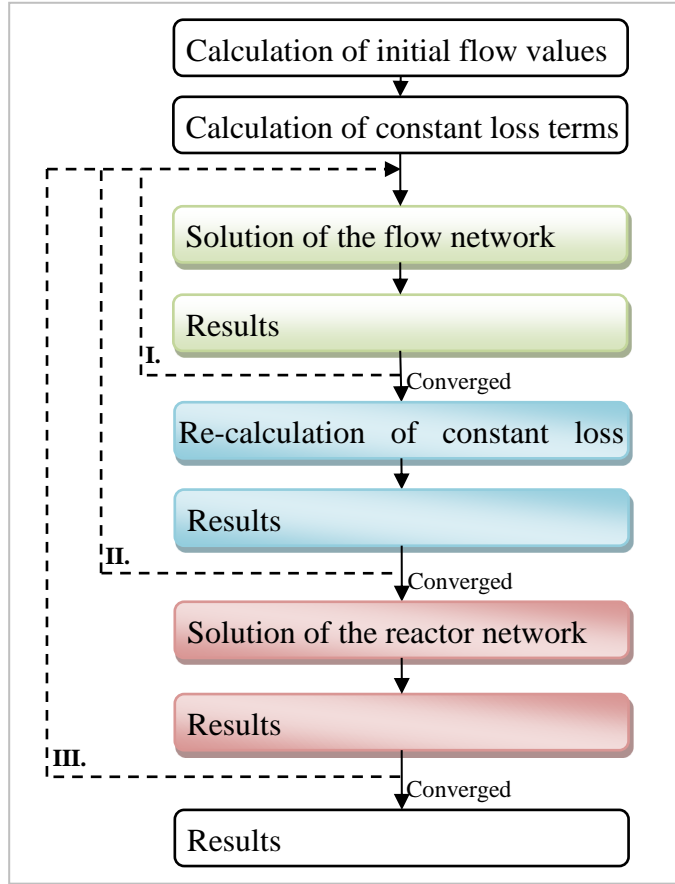


**Figure 3.2 - Solution procedure for the network system**

### 3.2 Loss Models

A 1D flow modeling approach requires utilization of proper loss flow correlations and loss factors. Although it is not possible to model every loss element inside the 3D domain an approximation can be made by using the 2D section shown in Figure 3.1. An important loss element is the liner hole element, the discharge through a liner hole is given as in equation (138), [1].

$$C_D = \frac{1.25(\psi - 1)}{\left[4\psi^2 - \psi(2 - \alpha)^2\right]^{0.5}} \quad (138)$$

$\psi$  : ratio of jet dynamic pressure to the annulus dynamic pressure

$\alpha$  : ratio of hole mass flow rate to annulus mass flow rate

Liner hole element equation is special equation [1], which describes the loss during air flow passing through from a liner hole.  $C_D$  equation is defined by Kaddah [1] for plain circular holes. Liner hole element flow schematic representation is shown in Figure 3.3.

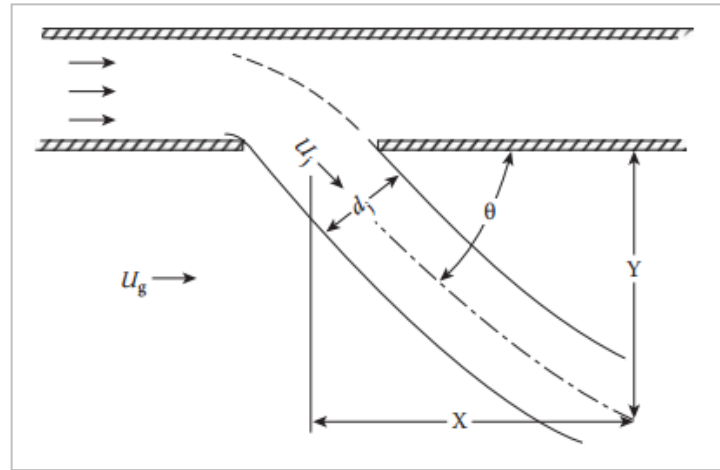


**Figure 3.3** – Flow Through Liner Hole [1]

Sudden expansion and sudden contraction elements are also can be seen in the annulus flow region. Loss coefficients for these regions are given in equations (139) and (140), [28], also can be seen in Figure 3.4.

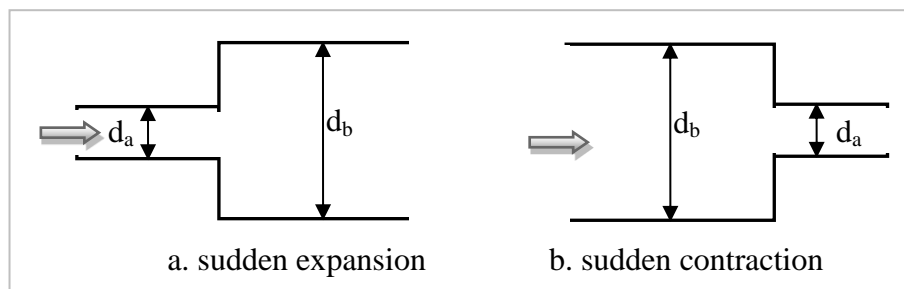


**Figure 3.4** - Sudden expansion and sudden contraction loss elements

$$\text{Sudden expansion element: } k = \left(1 - \frac{d_a^2}{d_b^2}\right)^2 \quad (139)$$

$$\text{Sudden contraction element: } k = 0.42 \left(1 - \frac{d_a^2}{d_b^2}\right) \quad (140)$$

Other loss elements utilized in the modeling are gradual expansion for the expanding regions of the annulus, gradual contraction for the contracting regions of the liner internal elements and 90 degrees round section turn for the turning section of the annulus to inner liner connecting element. These losses can be found tabulated in the literature.

### 3.3 Fuel Surrogate Models

#### 3.3.1 Aviation Fuels General

In aviation several different fuels are utilized. Although these fuels are known as similar there are slight differences among them. The refining industry has an effort to standardize all of these variations under Jet A-1. This fuel is a combination of thousands of hydrocarbons. Because of the "loose" specification of the fuel standards there are significant differences in all Jet A or JP-8 fuels. The difference between the Jet A-1 and JP-8 is an only an performance increasing additive package and this is mentioned by Colket et. al. [29]. The common characteristics of main jet fuels are outlined on the following Table 3.2.

**Table 3.2 – Common Characteristics of Jet Fuels [29]**

Name	Specification	Description	Flash point, C	Freeze point, C
Jet A-1	ASTM D1655, UK DefStan 91-91	Standard commercial jet fuel	>38	<-47
Jet A	ASTM D1655	U.S domestic jet fuel	>38	<-40
JP-8	MIL-DTL-83133	U.S. military jet fuel (Jet A-1 + 3 additives)	>38	<-47
JP-5	MIL-DTL-5624	U.S. Navy high flash jet fuel	>60	<-46
TS-1	GOST 10227-86	Russian jet fuel	>28	<-50*

\* Russian test method for "chilling point"



A better explanation of the fuel surrogates can be understood by examining the results of the "World Fuel Survey" conducted by the University Dayton Research Institute [29]. In which 55 jet fuel samples are analyzed and the contents are presented as a average summary table shown in Table 3.3.

**Table 3.3 – World Survey Composition Results [29]**

	World survey average, vol %	Composite Jet A blend
paraffins ( <i>n-</i> + <i>i-</i> )	58.78	55.2
Monocycloparaffins	10.89	17.2
Dicycloparaffins	9.25	7.8
Tricycloparaffins	1.08	0.6
alkyl benzenes	13.36	12.7
indans+tetralins	4.9	4.9
Naphthalene	0.13	<0.2
substituted naphthalenes	1.55	1.3

For modeling of the fuel combustion in computer environment a common fuel blend should be selected. Before deciding the optimum blend for the modeling surrogate the models surrogate composition in the literature should be examined. For military Jet A fuel two surrogate models are suggested in Oldani [30]. Two alternative surrogate compositions is shown on Table 3.4. A surrogate model is also presented on Table 3.5 for JP-8 fuel. And finally a fuel blend used for modeling of the JP-8 fuel is presented by the Honnet [30] and shown on Table 3.6.

**Table 3.4** – Jet A Surrogates [30]

Surrogate Components	#1 Mol%	#2 Mol%
n-dodecane	0.0	40.41
iso-octane	33.0	29.48
n-propylbenzene	0.0	22.83
1,3,5-trimethylbenzene	0.0	7.28
n-decane	42.7	0.0
toluene	24.3	0.0

**Table 3.5** – JP-8 Surrogates [30]

Surrogate Component	Vol%
n-dodecane	73.5
iso-octane	5.5
toluene	10.0
methycyclohexane	10.0
benzene	1.0

**Table 3.6** – JP-8 Surrogates - Aachen [30]

Surrogate Component	Mass%
n-decane	80.0
1,2,4-trimethylbenzene	20.0

### 3.3.2 Chemical Modeling of Jet Fuels

For modeling of the Jet Fuels detailed chemical mechanisms are required. These mechanisms can be directly or indirectly used to calculate the combustion products and temperature inside the combustion chambers. In this study 2 different detailed chemical mechanisms will be utilized. The 1<sup>st</sup> model is the Aachen University mechanism which utilizes 118 species and 527 reactions, the 2<sup>nd</sup> one is the Creck

mechanism of Politecnico di Milano for Kerosene combustion which has 121 species and 2673 reactions.

First of all, it is planned to utilize a surrogate that is the same as the Aachen blend of JP-8 fuel mentioned in the above section. This blend includes 80 % n-decane ( $C_{10}H_{22}$ ) and 20% trimethylbenzene ( $C_9H_{12}$ - $C_9H_{11}$ ). Utilizing of different fuel surrogates are also possible however for being consistent this composition will be tried to be conserved for the two mechanisms.

### **3.4 Combustor Results**

The results of the study are presented here for three different network flow solvers. All of them have the same CRN structure and two different chemical mechanisms are utilized for reactor networks. For comparison purposes, a chemical mechanism is selected for all three different versions of the network codes, furthermore the solution of the network codes are compared with the CFD analysis which is solved by using the same mechanism.

#### ***Aachen Mechanism***

First the results solved by utilizing the Aachen chemical mechanism are presented. Pressure distribution inside the combustor is given for three different regions of the combustor separately. Outer annulus total pressure distribution is presented in Figure 3.5. It can be seen that at the outer annulus, LTM and segregated models predicted a lower pressure distribution with the CFD results however; non-linear model predicts a higher distribution. Figure 3.6 represents the distribution of total pressure along the inner annulus nodes, the pressure values are higher than the CFD predictions for all the three models, especially the non-linear model predicts larger deviations.

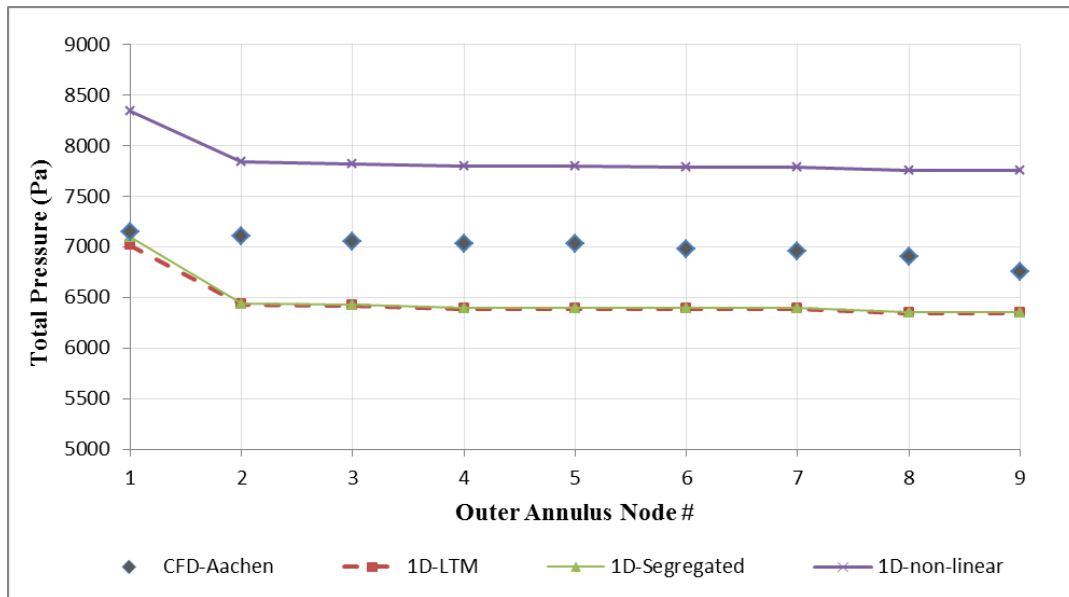


**Figure 3.5** - Total pressure distribution outer annulus nodes -Aachen mechanism

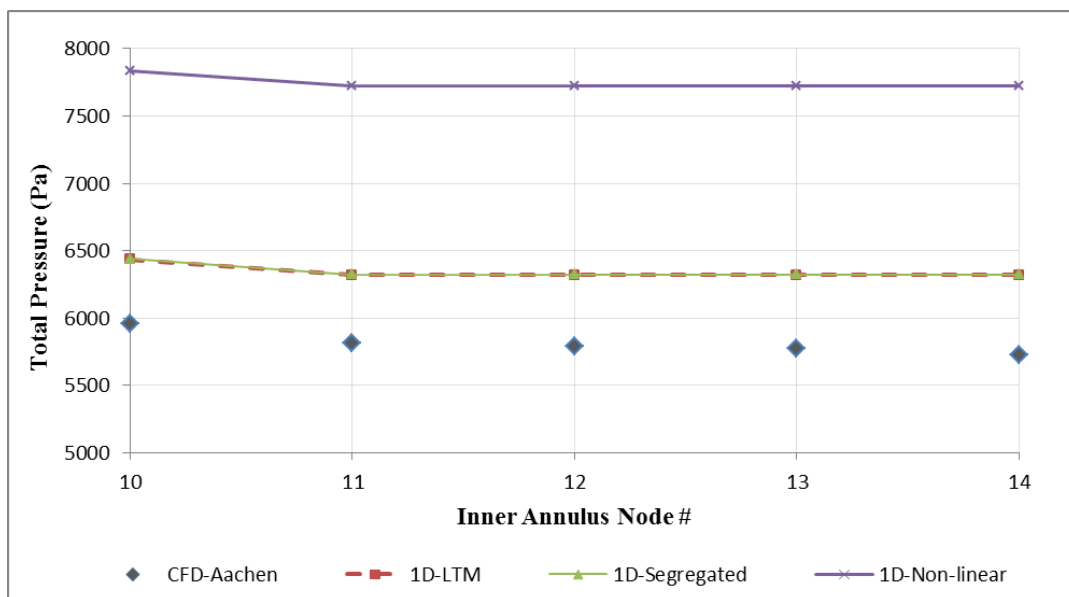


**Figure 3.6** - Total pressure distribution inner annulus nodes -Aachen mechanism

Total pressure distribution inside the liner nodes are better predicted with all of the models and results seem close to the CFD results as shown in Figure 3.7.

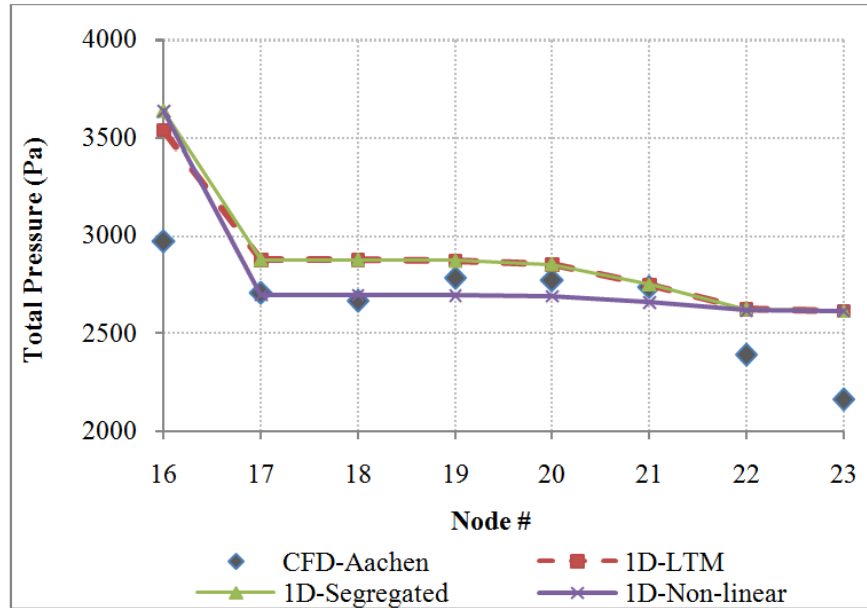


**Figure 3.7** - Total pressure distribution liner inner nodes - Aachen mechanism

A final comparison about pressure predictions can be made for the total pressure drop of the combustor. As can be examined in Figure 3.8 pressure drop predictions are close to the experimental values however, CFD predictions are lower than the experimental predictions. LTM method especially predicted a lower pressure loss compared with the other methods.

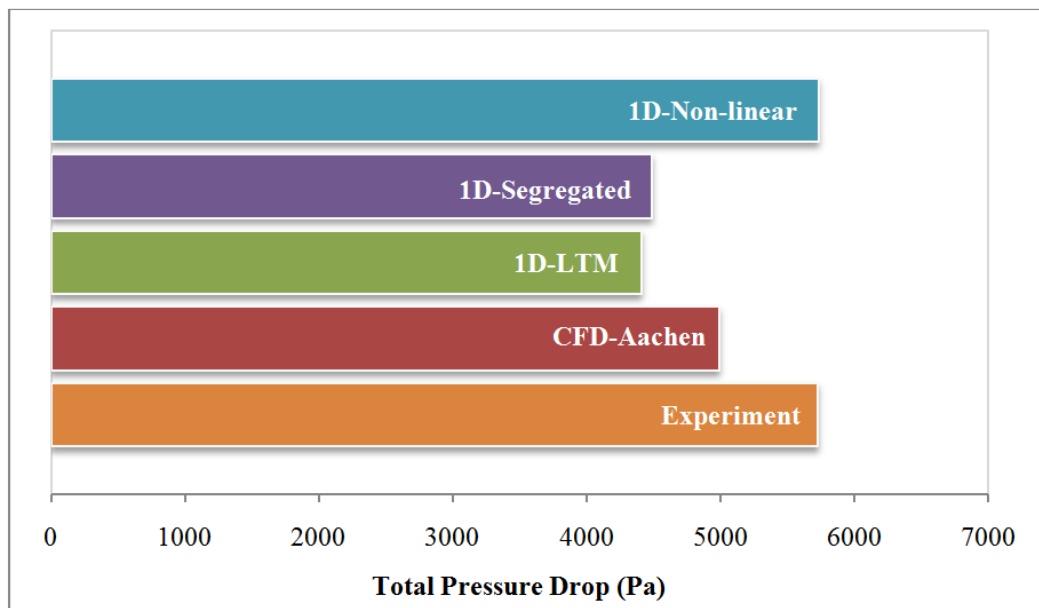


**Figure 3.8** - Total pressure drop - Aachen mechanism

Temperature distribution is given for the inner liner elements of the combustor, which are the direct output of the each reactor element. As the Figure 3.9 indicates temperature predictions are quite large at the primary and secondary zones, however they converge to reasonable values at the elements close to the combustor exit.

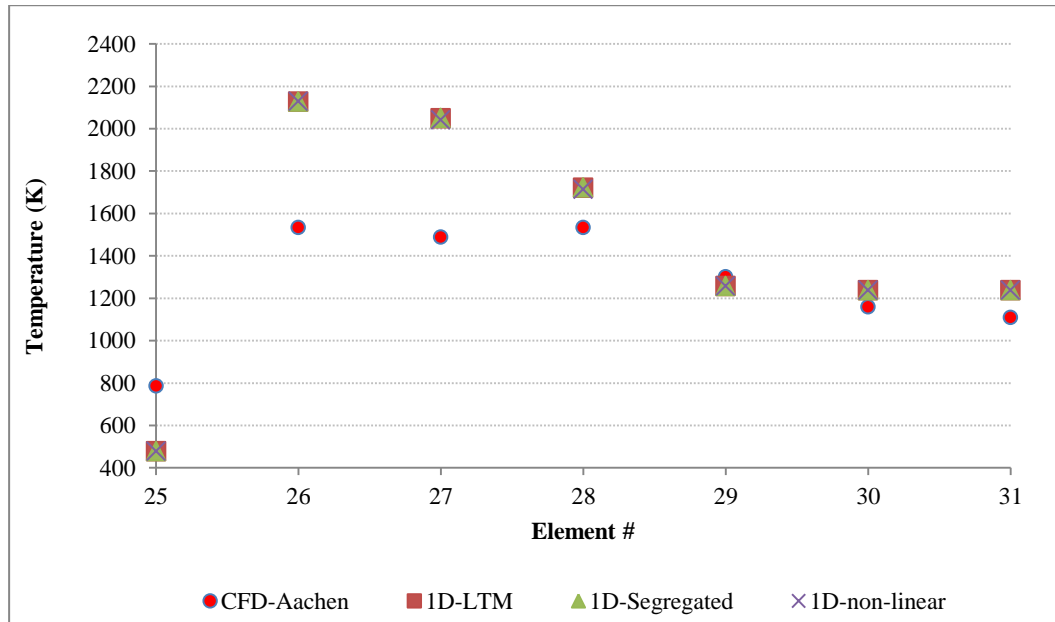


**Figure 3.9 - Temperature distribution - liner elements - Aachen mechanism**

Another important outcome of the code is the average exit temperature. Figure 3.10 represents that reactor models predict a higher temperature predictions when compared with the CFD and experimental outcomes.

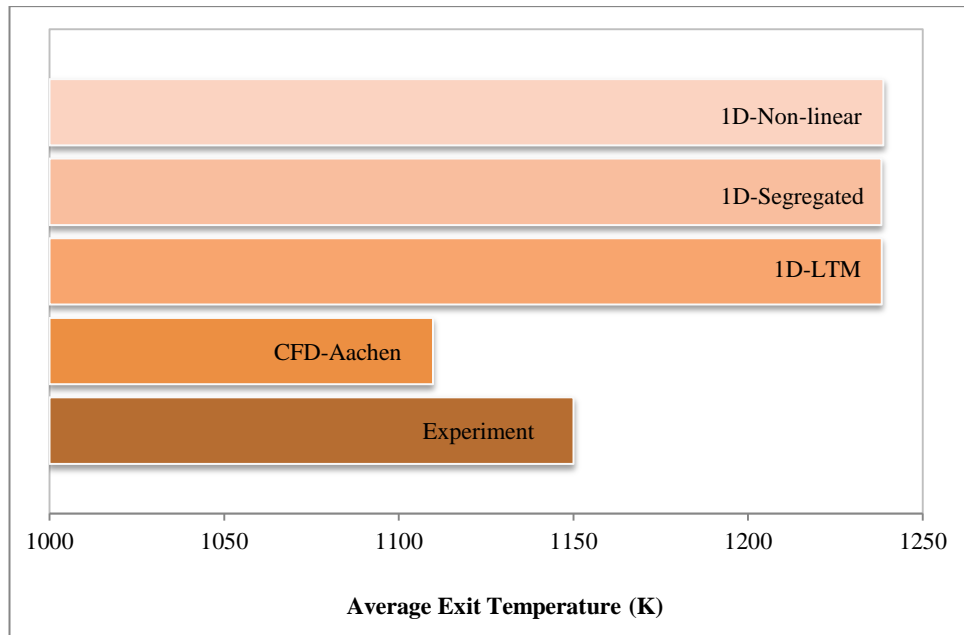


**Figure 3.10** - Average exit temperature - Aachen mechanism

Mass flow distribution across the holes of the combustor is presented on Table 3.7. As can be seen from the table, mass percentages passing through the combustor liner holes comply with each other in network models. However they show some deviance when compared with the CFD results.

**Table 3.7** – Hole mass flow distribution in percentage - Aachen Mechanism

Hole name	% CFD Aachen	% 1D-LTM	% 1D-Segregated	% 1D-Non-linear
Primary swirler	7.9	8.9	8.8	9.6
Secondary swirler	14.5	15.9	15.9	15.9
Primary outer	5.4	6.5	6.5	6.5
Primary inner	5.2	4.6	4.6	4.6
Secondary outer	12.8	11.5	11.5	11.5
Secondary inner	5.9	6.8	6.8	6.7
Dilution 1 outer	32.2	27.3	27.3	27.0
Dilution 1 inner	11.5	15.1	15.1	14.9
Dilution 2 outer	4.0	2.4	2.4	2.3
Dilution 2 inner	0.7	1.1	1.1	1.1

### *Creck Mechanism*

Results for the second mechanism are also presented. Figure 3.11 shows the total pressure distribution along the outer liner. Figure 3.12 shows the total pressure distribution along the inner liner for Creck mechanism. The results are similar with the previous mechanism's pressure results. In outer annulus LTM and segregated models predict lower pressure levels and non-linear model predicts a higher pressure levels compared with the CFD case. As for the inner annulus total pressure levels, 1D codes again predicts higher pressure distribution in comparison with the CFD results.

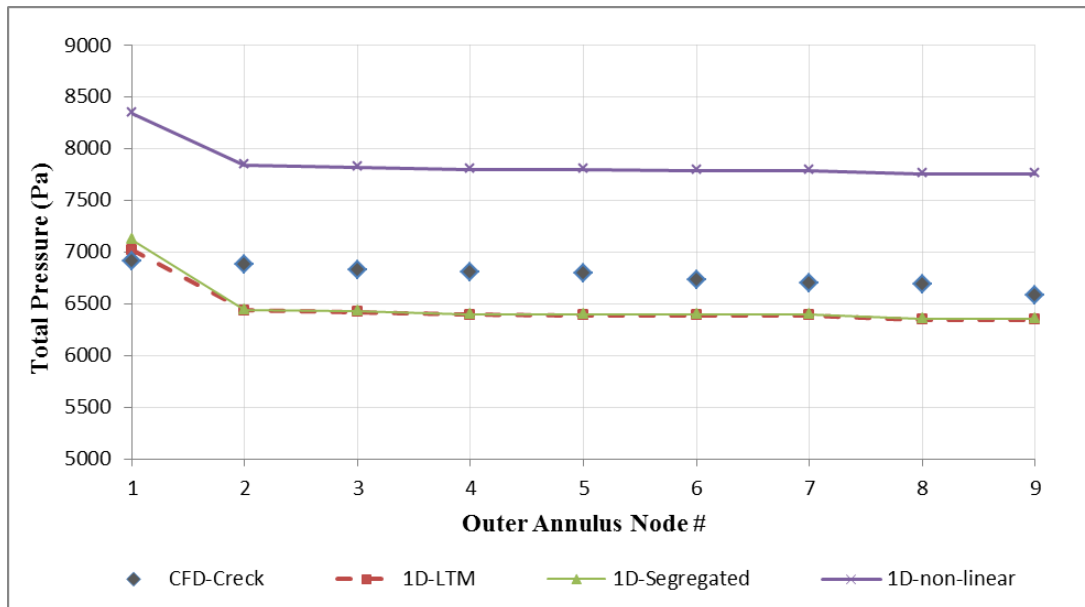


**Figure 3.11** - Total pressure distribution outer annulus nodes -Creck mechanism



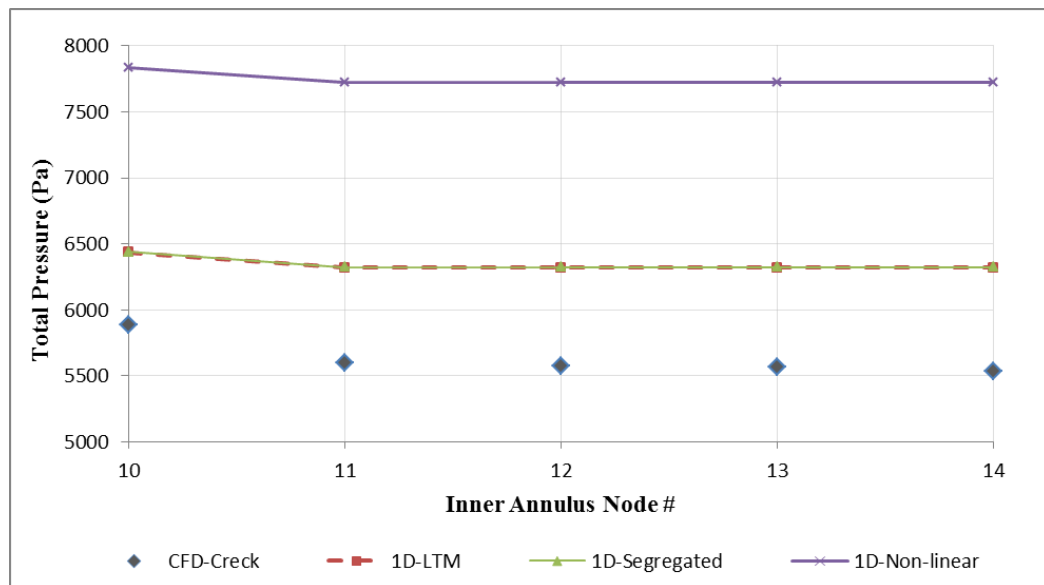


**Figure 3.12** - Total pressure distribution inner annulus nodes -Creck mechanism

Inner liner total pressure distribution shown in Figure 3.13, indicates similar pressure levels with the CFD results.

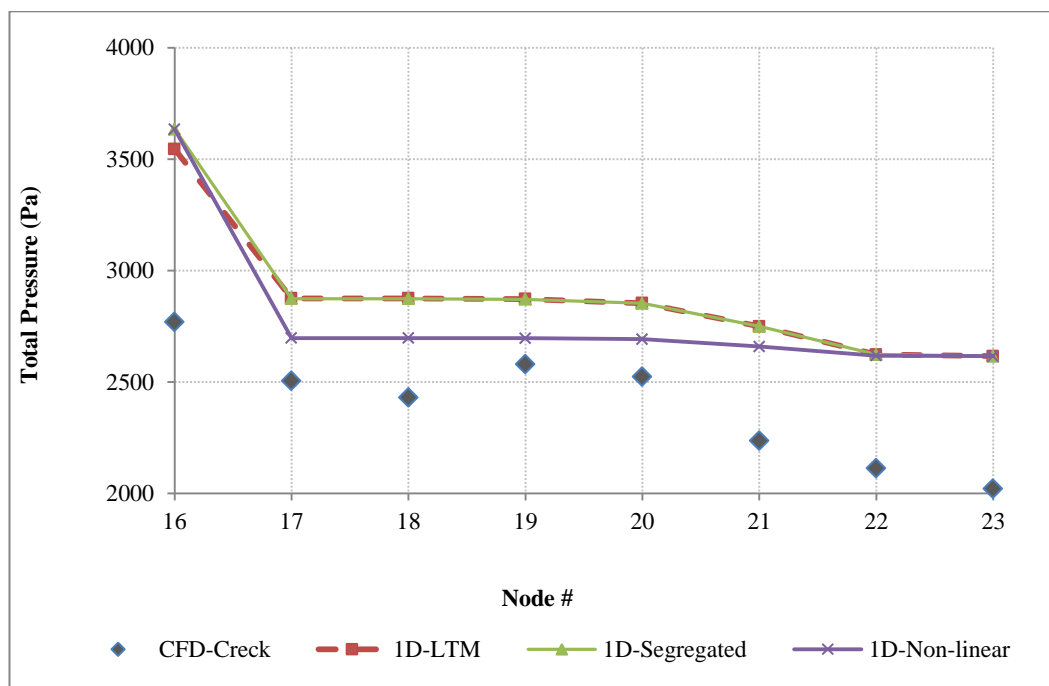


**Figure 3.13** - Total pressure distribution - liner inner nodes - Creck mechanism

Total pressure drop given in Figure 3.14 is also very similar with the previous results. Again LTM model predicts the lower pressure drop among the other models.

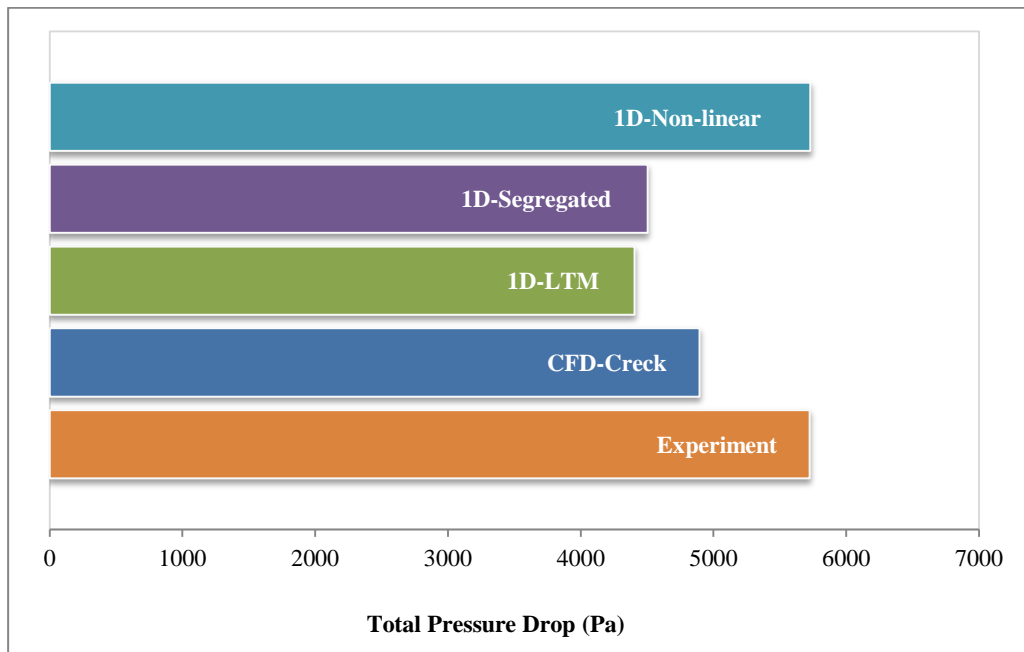


**Figure 3.14** - Total pressure drop - Creck mechanism

Temperature distribution along the liner inner elements are also given in Figure 3.15 for Creck mechanism. Temperature predictions are similar with the Aachen results; a significant amount of over-prediction can be seen in primary and secondary zones and came to reasonable values at the following elements.

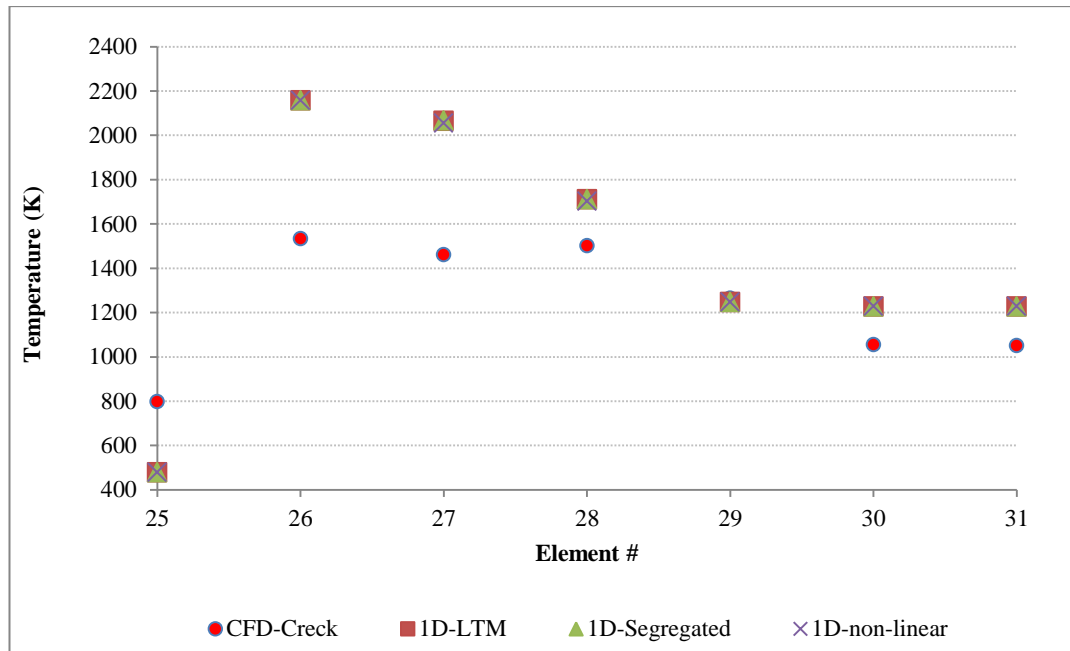


**Figure 3.15** - Temperature distribution - liner elements - Creck mechanism

Average exit temperature given in Figure 3.16 shows the 1D code predicts higher exit temperature whereas CFD analysis predicts a significantly lower temperature at the exit when compared with the experiment results.

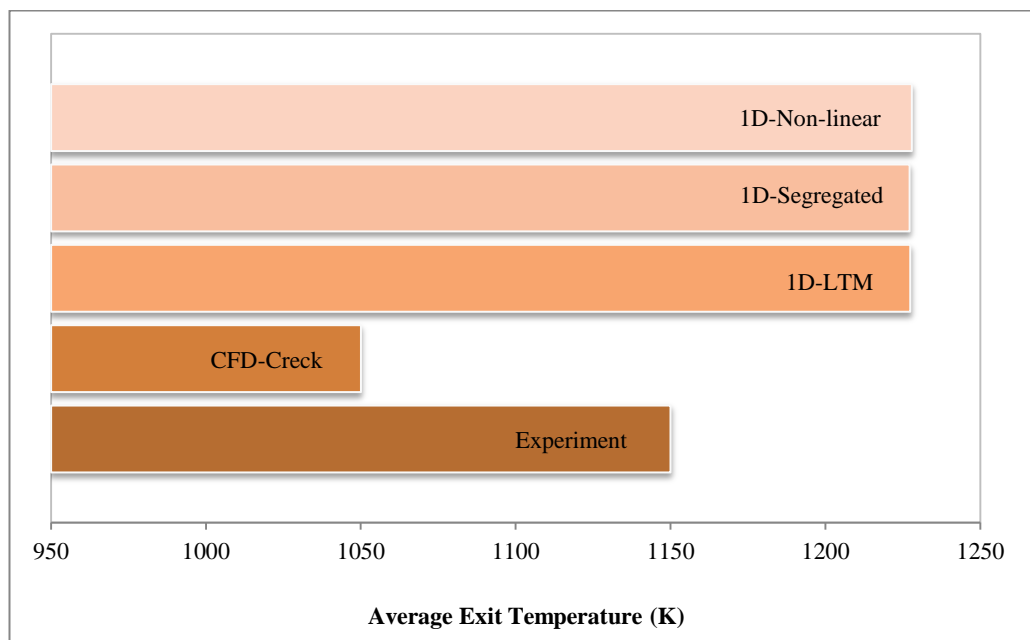


**Figure 3.16** - Average exit temperature - Creck mechanism

Mass flow distributions given on Table 3.8 shows similar results with the Aachen mechanism's results, 1D codes are comply with each other but they have relatively small deviances when compared with the CFD results in general.

**Table 3.8** – Hole mass flow distribution in percentage - Creck Mechanism

Hole name	% CFD Creck	% 1D-LTM	% 1D-Segregated	% 1D-Non-linear
Primary swirler	7.8	8.9	8.8	9.6
Secondary swirler	14.4	15.9	15.9	15.9
Primary outer	5.4	6.5	6.5	6.5
Primary inner	5.2	4.6	4.6	4.6
Secondary outer	12.8	11.5	11.5	11.5
Secondary inner	5.9	6.8	6.8	6.7
Dilution 1 outer	32.3	27.3	27.3	27.0
Dilution 1 inner	11.6	15.1	15.1	14.9
Dilution 2 outer	4.0	2.4	2.4	2.3
Dilution 2 inner	0.7	1.1	1.1	1.1

## CHAPTER 4

### COMBUSTOR PERFORMANCE VERIFICATION DATA

#### 4.1 CFD Verification

##### 4.1.1 Model Description

Verification of the models are made by performing 3D CFD analysis of TEI combustor and also by using the experimental results obtained in TEI combustor test facility. TEI experimental combustor is a through flow type annular combustor. The combustor has seven sectors, it is shown in Figure 4.1 [34].



**Figure 4.1** - TEI experimental through flow combustor [34]

The cut section of the combustor is shown in Figure 4.2; it should be noted that the drawing is a CFD type of model, so it only represents the air volumes. Air enters from the inlet of the casing section (shown in dark green), then it enters into the liner section from the holes on the outer of the liner. Air entrance holes are: primary and secondary swirler holes, primary holes, secondary holes and dilution holes. Actually

there is no distinct difference between the secondary and dilution holes. They are basically used for cooling of the combustion products to get a stable target exit temperature. Homogenous mixture of combustion products and dilution air left the combustion chamber from the exit section. In the engine, turbine inlet guide vanes come after the combustion chamber; however in the experimental configuration the exit section is opened to the atmosphere.

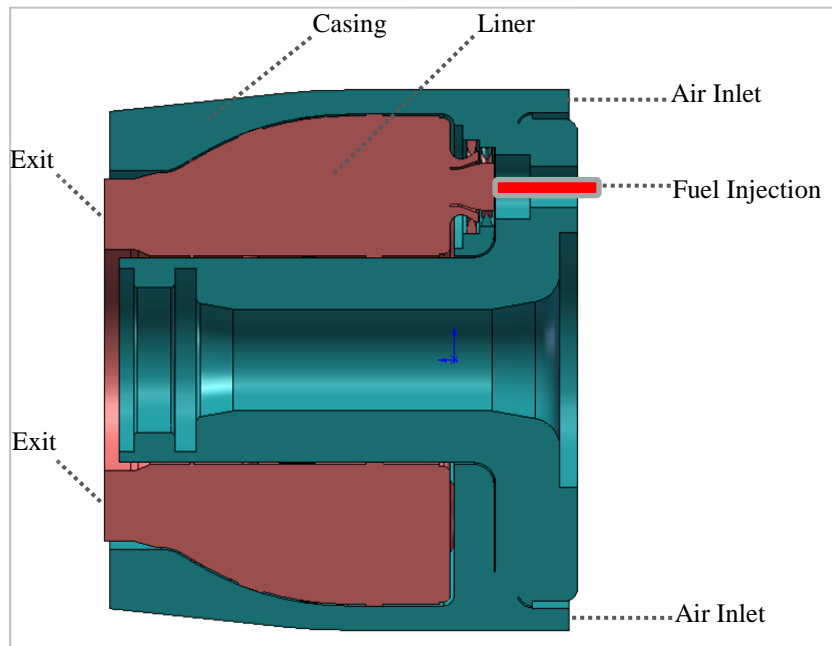


**Figure 4.2 - Cut Section of the TEI Combustor**

The hole configuration on the liner is shown in Figure 4.3 in detail. Swirler holes inject the air onto the fuel injection zone and a fuel-air mixture near stoichiometry is obtained at the swirler exit of each sector.

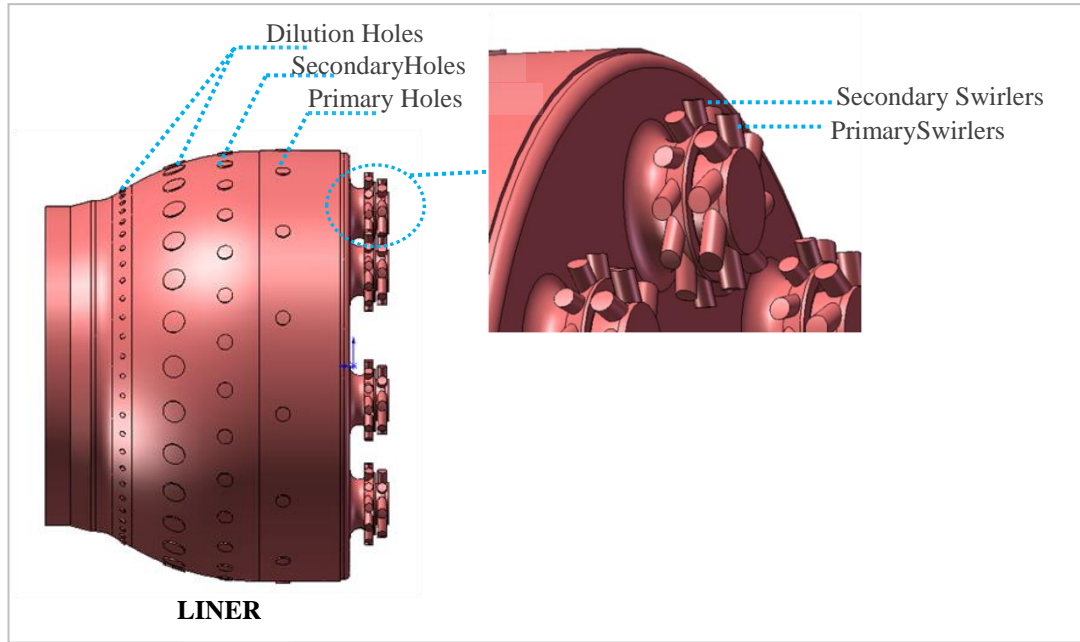


**Figure 4.3 - Liner Air Flow Hole Configuration**

#### **4.1.2 Boundary Conditions**

Combustor performance tests are performed for the boundary conditions given on Table 4.1. The inlet of the combustor is given mass flow boundary condition. The outlet is open to atmosphere as in the combustor test conditions. The fuel is injected into the domain at the exact place of the fuel injector. Fuel is injected from a 3mm opening and is forming a cone sheet with a cone angle of 30 degrees. The injected particles mix with the incoming air from the primary and secondary swirler air to form a combustible mixture. The sides of the combustor are given symmetric boundary condition. Furthermore in order to measure the amount of air passing through the liner holes internal hole boundaries are added on the model. These hole elements are of the type interior and don't have any effect on the flow field. The experimental performance tests supply data for the chamber inlet temperature, inlet total pressure, chamber exit temperature, chamber exit pressure and chamber exit species concentration. For the other internal state parameters of the combustor such as hole flow distribution, internal temperature distribution and internal pressure distribution detailed CFD analysis are utilized.

**Table 4.1** – Combustion chamber test boundary conditions

Air mass flow rate (kg/s)	0.18
Fuel mass flow rate (kg/s)	0.0037
Combustor inlet temperature (K)	478
Combustor exit pressure	Open to atm.
Air/Fuel Ratio	49

### 4.1.3 Numerical Settings

In CFD analysis only a single sector of the flow domain is modeled and a total of 19M tetrahedral elements and 3.1M nodes are utilized, computational mesh is shown in Figure 4.4. The mesh is created to guarantee a  $y^+ \sim 60$  for the wall regions. ANSYS FLUENT is utilized for performing the simulations. RANS model with realizable  $k-\epsilon$  turbulence model are selected. The analysis settings are summarized on Table 4.2.

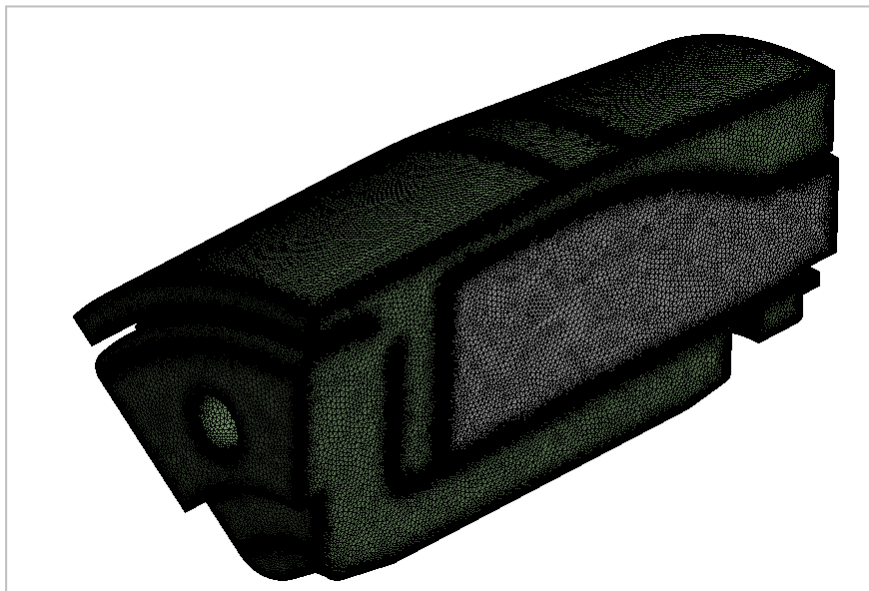


**Figure 4.4** - Combustor solution grid

Liquid fuel is injected into the domain as a discrete phase. No physical injector is modeled inside the combustor, instead discrete phase (liquid fuel mixture) is injected



into the domain from a point with a predefined shape of a cone. The entrance of the cone is given the diameter of the typical injector used in the real combustor. The injection velocity and cone angle information are given according to the fuel injector tests performed previously. After the liquid fuel is introduced into domain as a discrete phase, liquid fuel droplet group interact with the flow field and move accordingly. At the same time they are heated up and evaporate and finally form a mixture of air-gaseous fuel. After this point the solver handles the combusting mixture as by the primary mixture fraction parameter.

**Table 4.2** – Analysis Settings

Analysis Settings			
	Main Setting	1st Setting	2nd Setting
<b>Solver</b>	Pressure Based		
<b>Turbulence Model</b>	k- $\epsilon$ realizable	standart wall functions	
<b>Radiation</b>	off		
<b>Combustion Model</b>	Non-Premixed Combustion	Steady diffusion flamelet Pre-Calculated chemistry table	
<b>Discrete Phase Model</b>	Interaction with continuous phase	Two-way turbulence coupling	
<b>Liquid Droplet Injection</b>	Injection type	Solid Cone Multicomponent liquid fuel Velocity magnitude: 50 m/s	
<b>Material</b>	Air-combustion species mixture	PDF Mixture	
	Liquid kerosene model	YC10H22	0.8
		YC9H12	0.2
<b>Boundary Conditions</b>	Inlet	Mass flow inlet	
	Outlet	Pressure outlet	
	Side Walls	Periodic Interface	
	Liner holes	interior surface	
<b>Solution Methods</b>	Pressure Velocity Coupling	SIMPLE/COUPLED	
	Spatial Discretization	Gradient	Green-Gause node based
		Pressure outlet	PRESTO
		Density	Second order upwind
		Momentum	Second order upwind
		Turbulent Kinetic Energy	Second order upwind
		Turbulent Dissipation Rate	Second order upwind
		Energy	Second order upwind
		Mean Mixture Fraction	Second order upwind
		Mixture Fraction Variance	Second order upwind

For modeling of the combustion, non-premixed modeling approach is preferred. In non-premixed combustion fuel and oxidizer are mixed after entering the domain. A mixture fraction based approach is utilized, by this way solution of the complex mechanism during the solution of the domain is bypassed. Instead, a preliminary chemistry calculation stage is performed and it is used to generate flamelet library. Flamelet modeling method based on the fact that, a small flame structure inside the combustor domain reflects the character of an equivalent flamelet. Flamelet library supply information about the temperature and species distribution inside the domain, they are given as a function of mixture fraction and scalar dissipation [35-36]. In this study, two flamelet libraries are generated in mixture fraction space one for Aachen mechanism [31] and the other is for the Creck mechanism [32-33] by using detailed chemistry solver COSILAB. For large mechanism it is difficult to achieve convergence at higher dissipation rates near extinction limit, hence for both of the mechanisms flamelets are generated between 0.01 - 120 1/s. An example data from the generated flamelet data set is shown in Figure 4.5 for dissipation rate 1 (1/s).

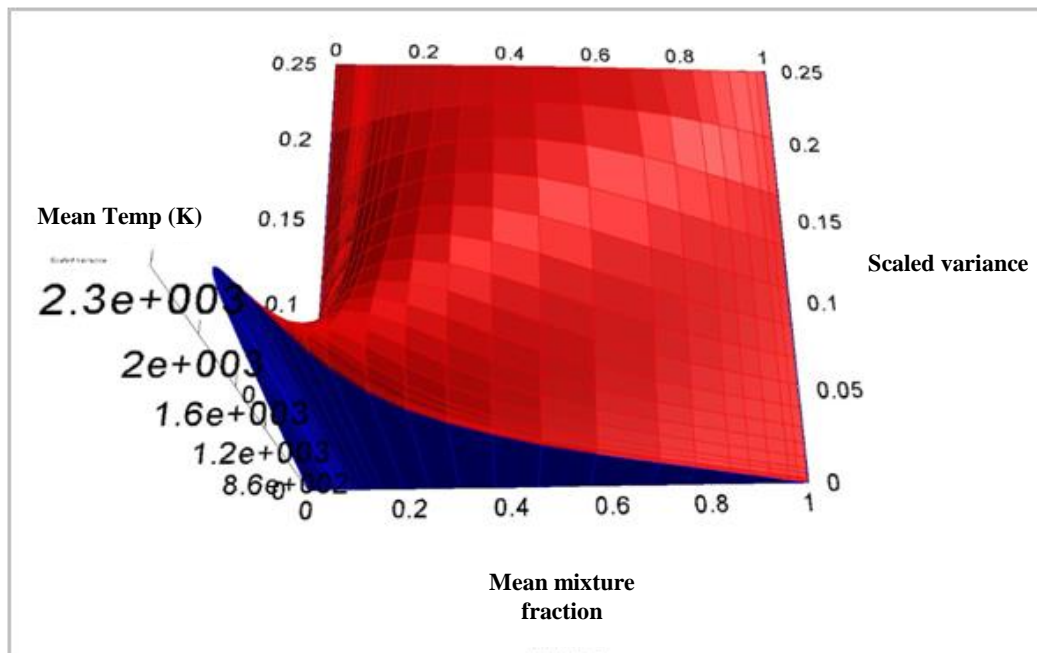


**Figure 4.5** - Change of temperature for aachen mechanism for scalar dissipation  $s=1(1/s)$

After formation of the flamelets, they are imported into CFD solver and a combustion solution can be obtained. Numerical analysis are performed for the same boundary conditions with the experiments.

The analysis is iterated until steady convergence is achieved. For the convergence of the flow field the residuals of the flow field parameters are monitored and solution is continued until the all of the residuals are dropped below the convergence limits. The limits of convergence for the flow parameters are given on Table 4.3. The convergence criteria shown on Table 4.3 are selected in the upper limit, they may be selected lower values however in a steady combustion simulation the main convergence parameters are the time-wise tracked combustor parameters such as exit temperature and flow values (such as pressure or velocity) near the critical regions. The analysis is iterated until steady convergence is achieved.

**Table 4.3 – Convergence Criteria for the Analysis**

<b>Residuals</b>	<b>Residual based on</b>	<b>Criteria</b>
continuity	rate of mass creation in cells	1.00E-03
x-velocity	x-velocity parameter	1.00E-03
y-velocity	y-velocity parameter	1.00E-03
z-velocity	z-velocity parameter	1.00E-03
energy	energy parameter	1.00E-06
k	turbulence k parameter	1.00E-03
epsilon	turbulence epsilon parameter	1.00E-03
fmean	mass fraction residual of fuel	1.00E-03
fvar	variance of mass fraction of fuel	1.00E-03

#### **4.1.4 RANS-CFD Results**

The results of the CFD analysis are presented in this section. As it is mentioned in previous section, two different mechanisms are utilized in the analysis; hence the results are presented separately for the analysis of these mechanisms. The basic performance parameters are presented here as the output. These are the temperature,

total pressure and species distributions. These data are also available as an experimental output in the next section, and for this reason the values obtained from the CFD can be used as a comparison tool for the results of the 1D code.

#### 4.1.4.1 Velocity Results

##### *Aachen Mechanism*

Velocity figures are the important performance indications. It can be seen in Figure 4.6 that the velocity distribution is dominated by the primary hole flow. The air jet is flowing through the primary and dilution hole groups with an average velocity of 90 m/s and forms a barrier in front of the centerline flow inside which hot gases are recirculating. The low velocity region at the primary zone is the recirculation region which can also be seen in Figure 4.7. The incoming air flow from different hole groups combines with the hot gases and leaves the combustor with an average Mach number of 0.2.

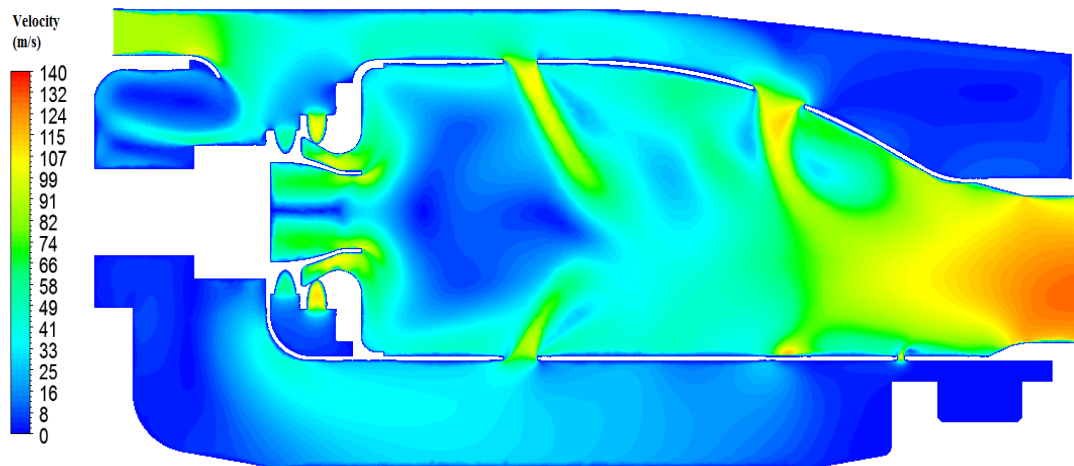


**Figure 4.6** - Velocity distribution along centerline section

Velocity vector distribution along the centerline section shows the uniform recirculation zone at the combustion region. It also shows the weak recirculation region that is occurring at the end of the outer annulus region.

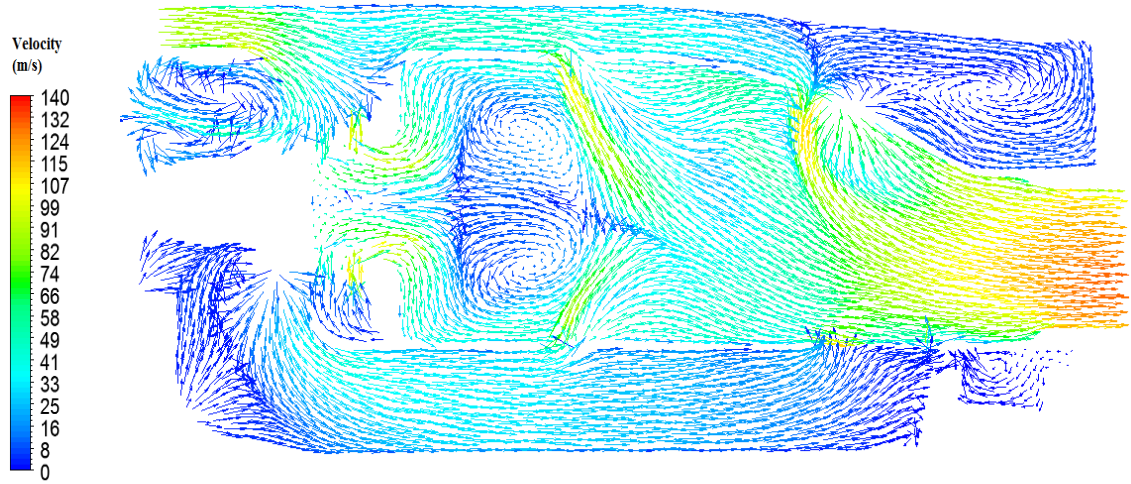


**Figure 4.7** - Velocity vector distribution along centerline section

Mach number characteristic of the combustion chamber, shown in Figure 4.8, shows the critical Mach number values at the important locations, such as liner inlet, exit, and hole passages. The inlet and exit of the combustor has Mach number value around 0.2, at the annulus section it is around 0.1, and at the hole regions it reaches 0.3.

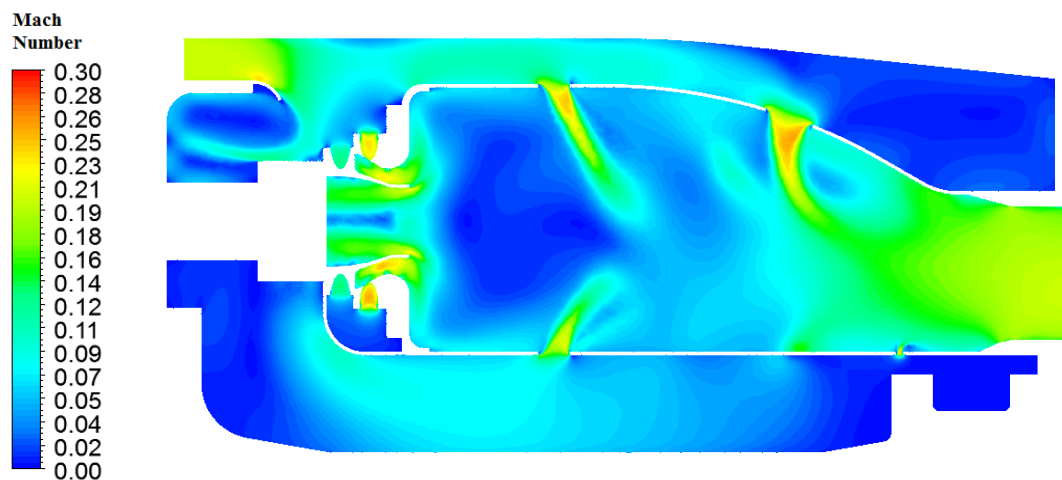


**Figure 4.8** - Mach number distribution along centerline section

The exit temperature velocity and Mach number distribution are shown in Figures 4.9 and 4.10. The magnitude of the velocity increases towards the inner liner region. The Mach number value is nearly homogenously distributed at the exit, and its maximum value at the exit section is 0.21.

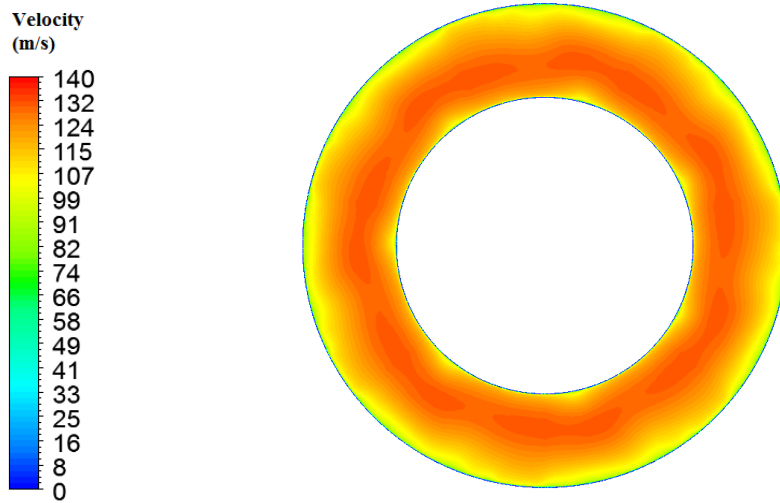


**Figure 4.9** - Velocity distribution at the exit plane

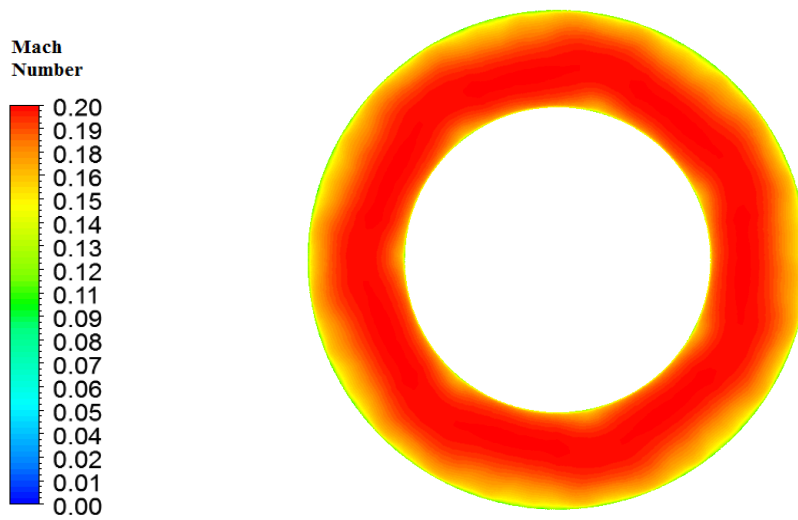


**Figure 4.10** - Mach number distribution at the exit plane

### ***Creck Mechanism***

The velocity figures for the analysis performed by using Creck detailed chemical mechanism shows similar characteristics with the Aachen results. The air jet is flowing through the primary and dilution hole groups with an average velocity of 90 m/s and forms a barrier in front of the centerline flow inside which hot gases are recirculating.

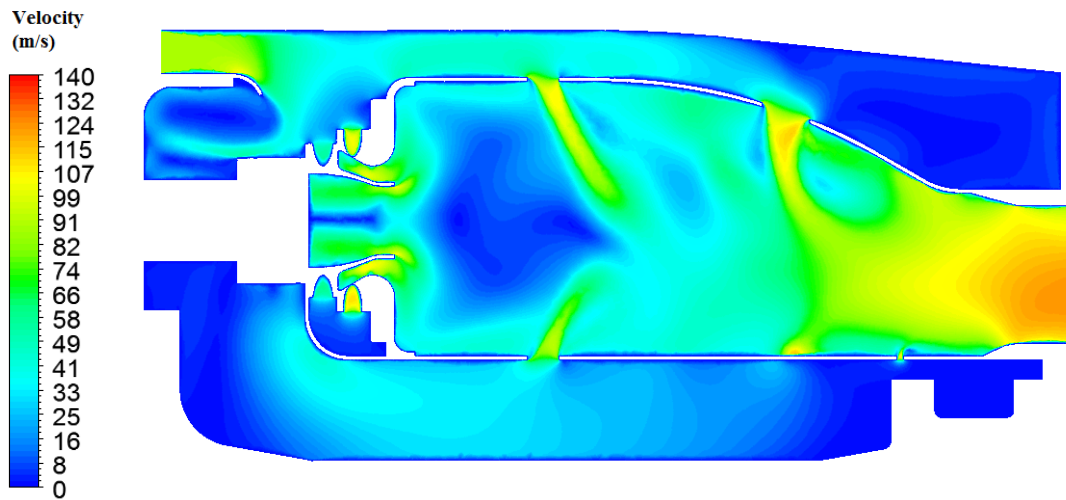


**Figure 4.11** - Velocity distribution along centerline section

Velocity vector distribution along the centerline section in Figure 4.12 shows the two recirculation zones mentioned in Aachen analysis results.

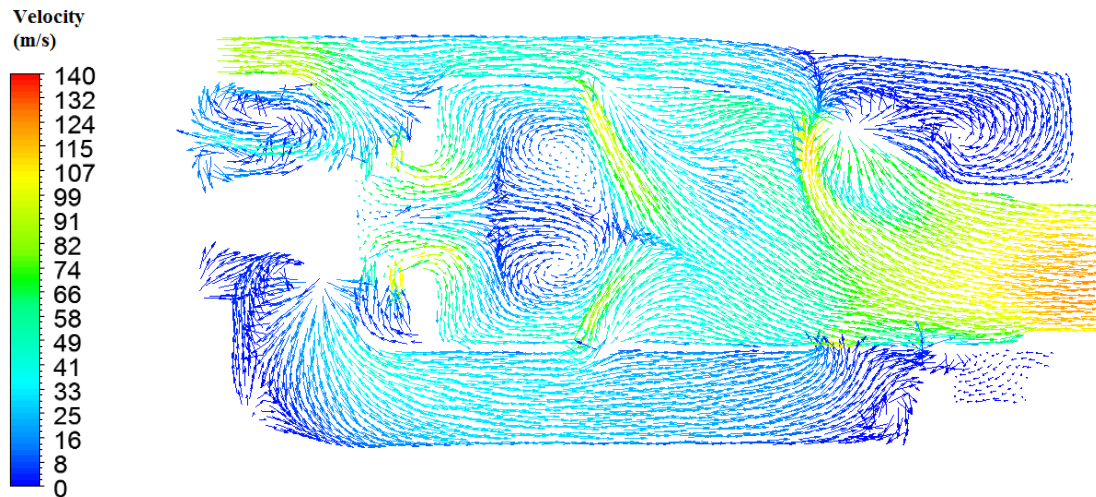


**Figure 4.12** - Velocity vector distribution along centerline section

Mach number distribution for Creck mechanism's analysis is shown in Figure 4.13. The inlet and exit of the combustor is around 0.2, at the annulus section it is around 0.1, and at the hole regions it reaches 0.3.

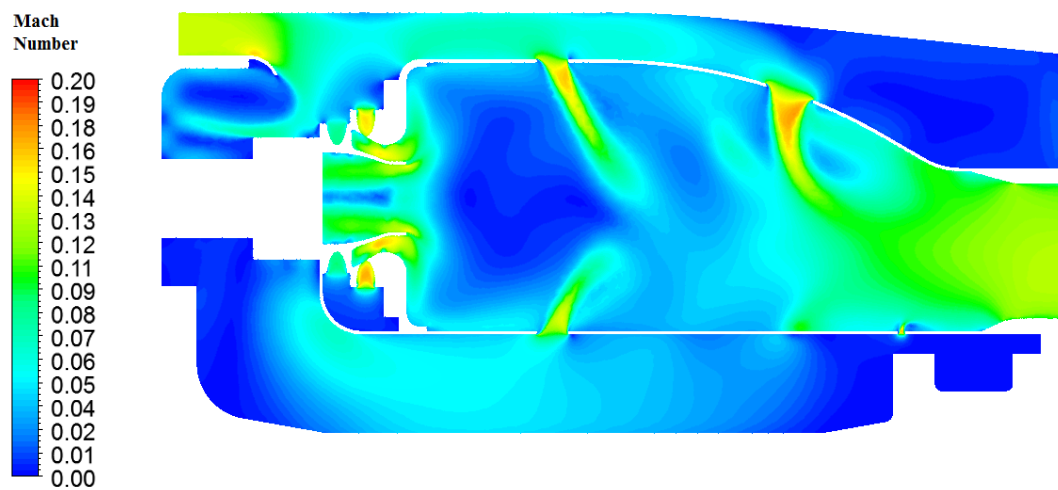


**Figure 4.13** - Mach number distribution along centerline section

The exit temperature velocity and Mach number distributions for the analysis with the Creck mechanism are shown in Figures 4.14 and 4.15. The magnitude of the velocity increases towards the inner liner region as in the Aachen case. The only difference is that the velocity values are slightly lower than the Aachen case. It is



approximately 120 m/s at maximum. Mach number is nearly homogenously distributed at the exit, and its maximum value at the exit section is around 0.21.

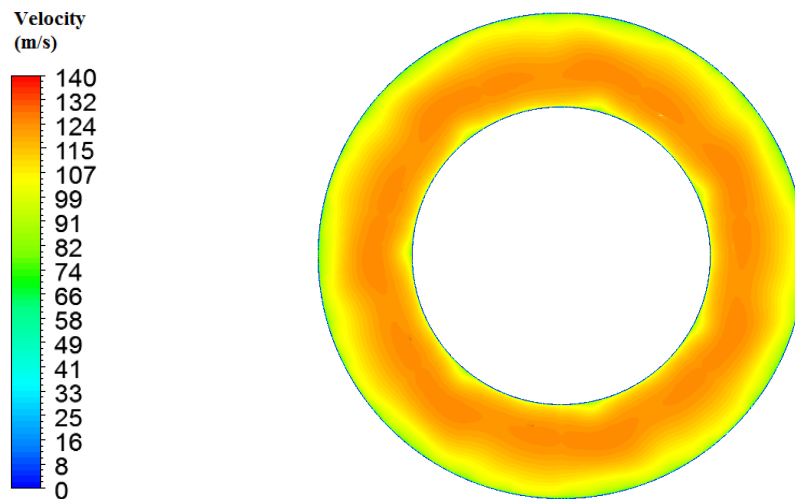


**Figure 4.14** - Velocity distribution at the exit plane

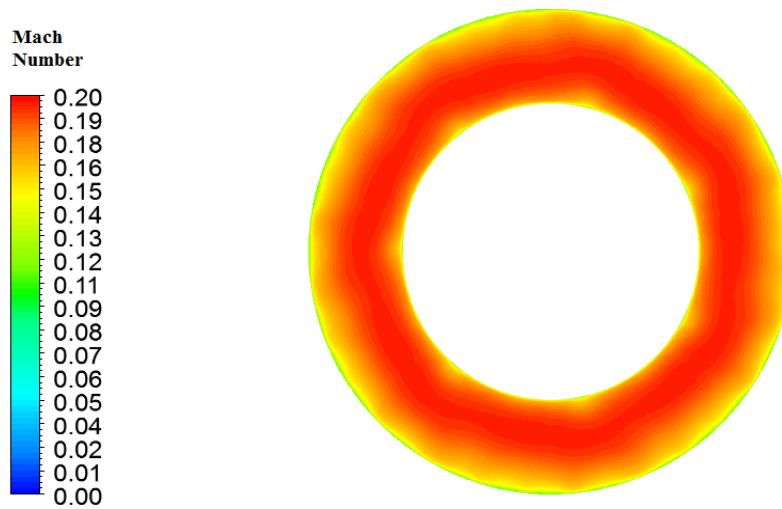


**Figure 4.15** - Mach number distribution at the exit plane

#### 4.1.4.2 Flow Streamlines

##### *Aachen Mechanism*

Streamlines of the flow particles released from the inlet of the flow field is given in Figure 4.16. The swirler region and outer-inner flow distribution can be seen in the figure. The swirler flow causes a low velocity region in the primary zone of the combustor, in which the particles are following radial paths.

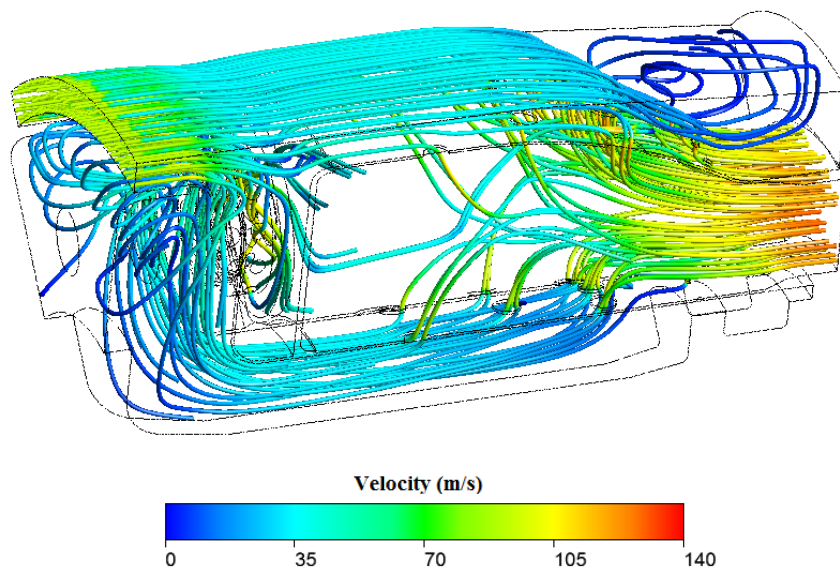


**Figure 4.16** – Streamlines emanating from the inlet

Figure 4.17 shows the particles emanated from the swirler holes. Most of the streamlines are headed towards the combustor exit, some of the streamlines passes through the side regions at the exit of the swirler. Particles released from the other hole groups (primary, secondary, dilution 1 and dilution 2) are shown in Figure 4.18. They are mixed with the corresponding inner-outer liner flow and joined to the main stream.

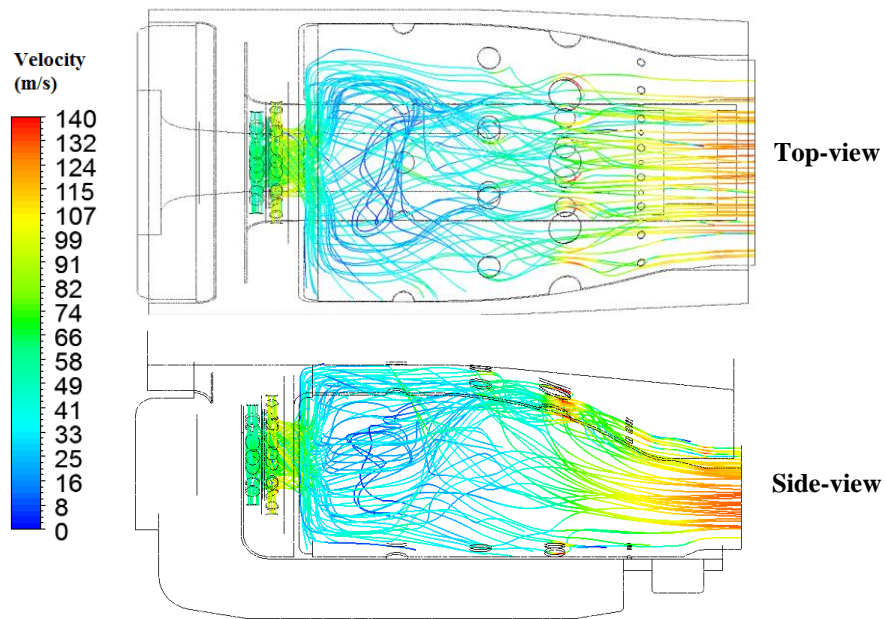


**Figure 4.17** – Streamlines emanating from the swirler holes

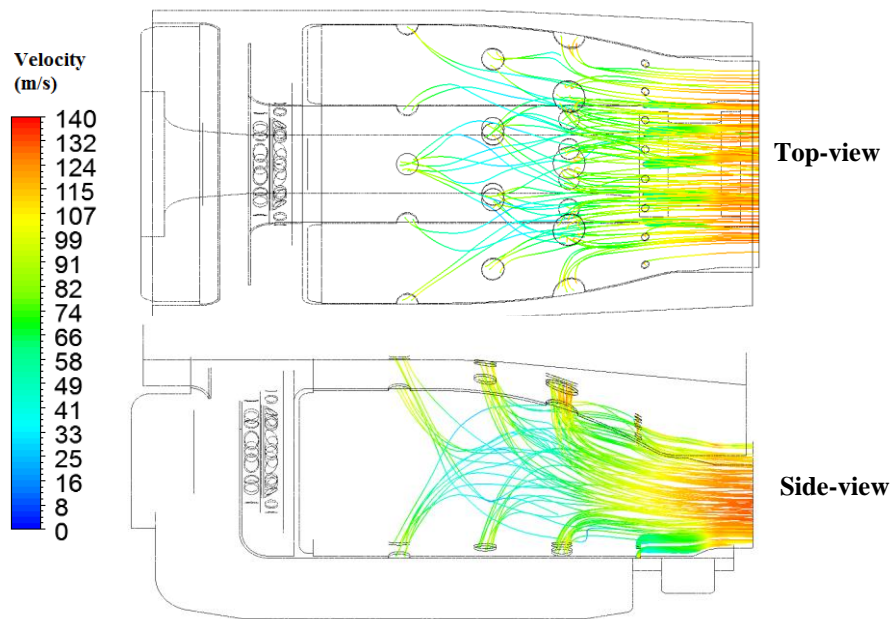


**Figure 4.18** – Streamlines emanating from liner holes

### ***Creck Mechanism***

Streamlines of the flow particles released from the inlet of the flow field for Creck mechanism's result is given in Figure 4.19. Streamlines again helps to define the radial particle movement and the recirculation zone.

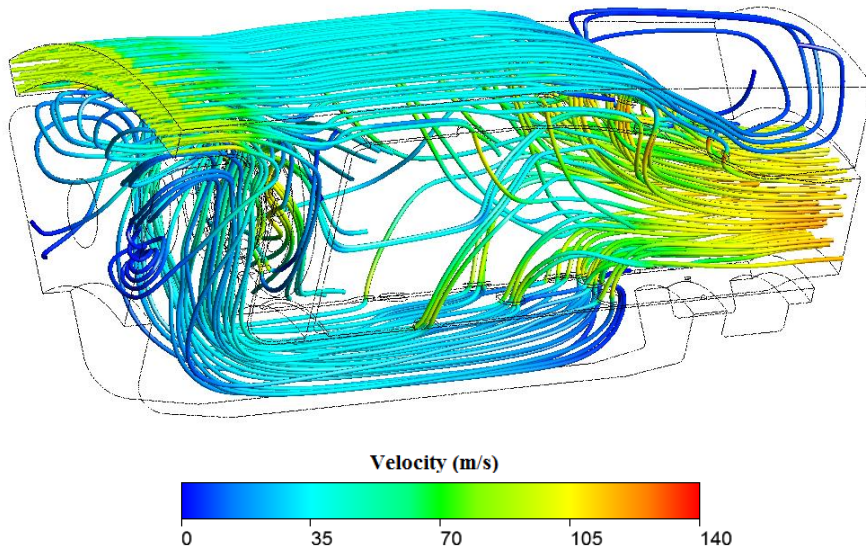


**Figure 4.19** – Streamlines emanating from the inlet

Figure 4.20 shows the particles emanated from the swirler holes. Most of the streamlines are headed towards the combustor exit, some of the streamlines passes through the side regions at the exit of the swirler. Particles released from the other hole groups (primary, secondary, dilution 1 and dilution 2) are shown in Figure 4.21. They are mixed with the corresponding inner-outer liner flow and joined to the main stream.

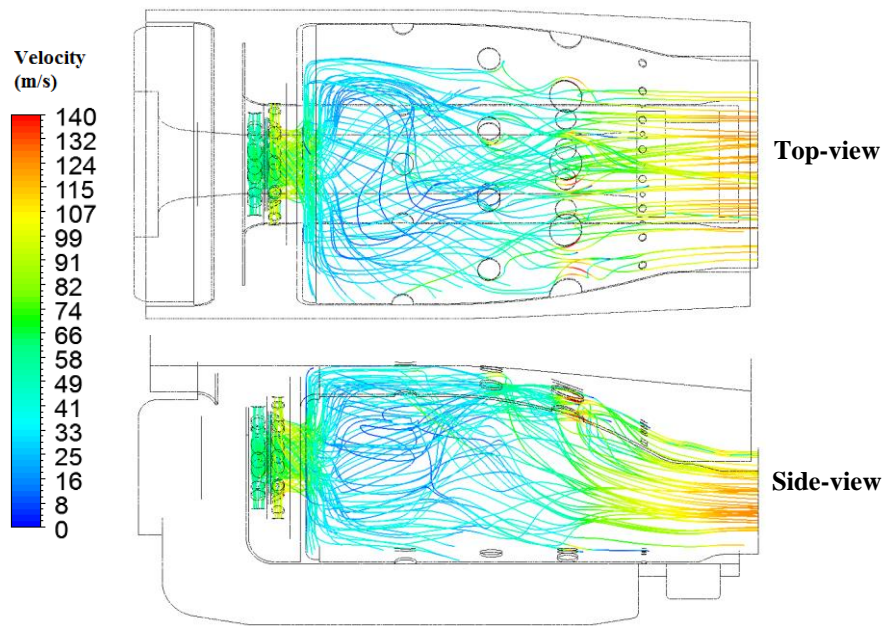


**Figure 4.20** – Streamlines emanating from the swirler holes

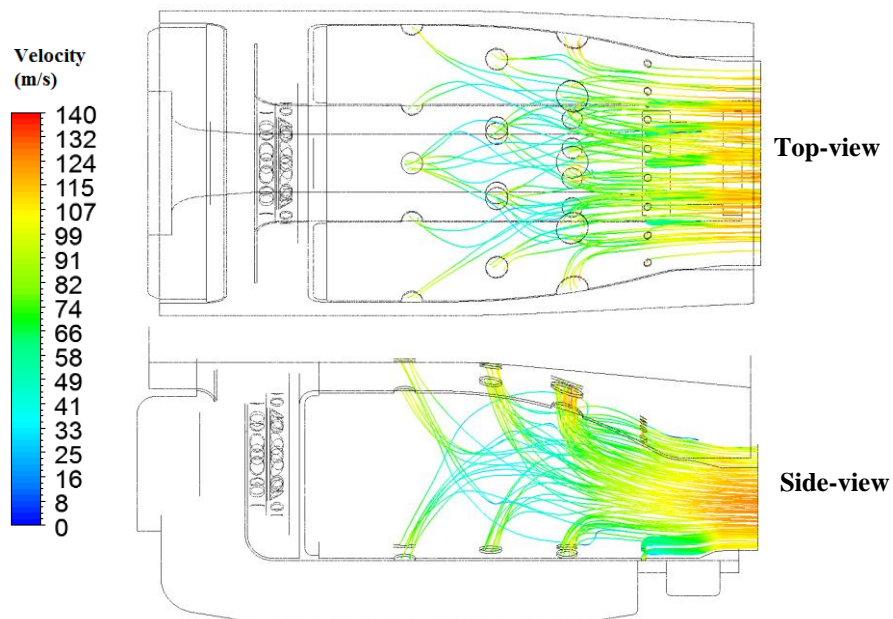


**Figure 4.21** – Streamlines emanating from liner holes

#### 4.1.4.3 Temperature Results

##### *Aachen Mechanism*

When the CFD results are processed, the temperature values of the combustion chamber at various planes are obtained. For understanding the 3D character of the combustion field, distribution of temperature at central section of the combustor and the exit plane presented here. As can be seen from the central section in Figure 4.22, the combustion core couldn't be held at the primary zone, it attached to the outer walls of the liner at the secondary zone this character of the combustor reduces the mixing in the chamber. The exit temperature distribution shown in Figure 4.23, it can be seen that a high temperature zone stretched till the end of the liner along the liner centerline section. The average exit temperature of the combustor is found to be 1109.8 K. The temperature gets a peak value of around 1350 K at the exit plane, close to the outer liner walls. This high spot is undesirable and may cause failure of turbine blade tips.

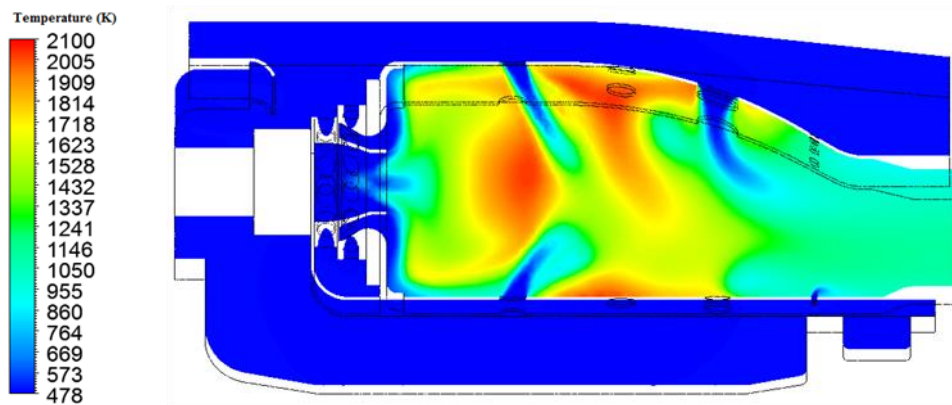


**Figure 4.22** - Temperature distribution along centerline



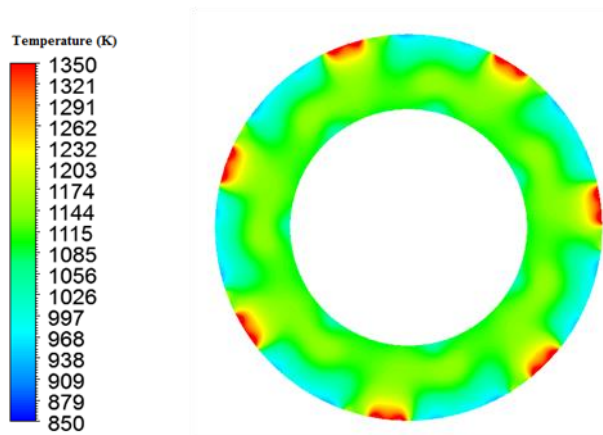


**Figure 4.23** - Exit plane temperature distribution

### *Creck Mechanism*

When the same planes are investigated for the Creck mechanism's result, it can be seen that the centerline section temperature distribution is quite similar. However the exit plane temperature at Figure 4.25 shows relatively lower temperatures when compared with the Aachen mechanism's results. This is also revealed in average exit temperature values, the average exit temperature is 1050 K when the creck mechanism is utilized. It is also observable that the peak hotspots at the exit plane are still there but they are modeled less pronounced by this model.

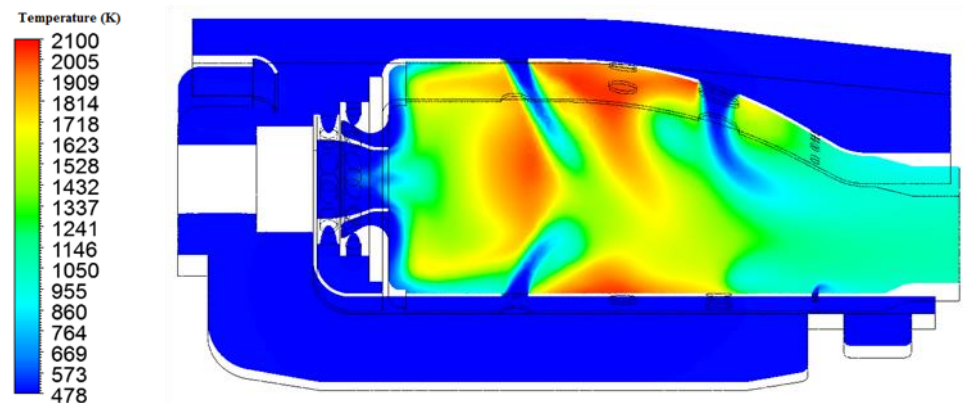


**Figure 4.24** - Temperature distribution along centerline

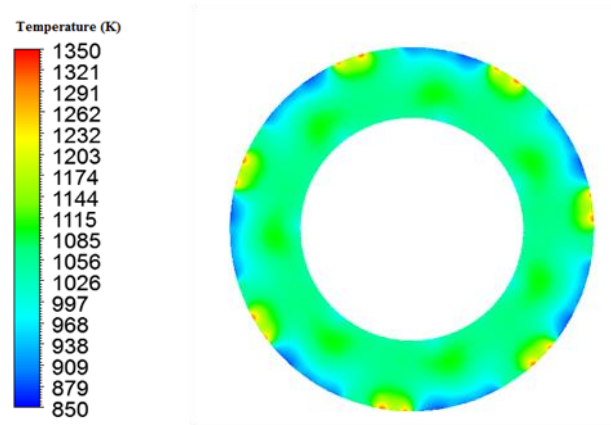


**Figure 4.25** - Exit plane temperature distribution

#### **4.1.4.4 Total Pressure Results**

##### ***Aachen Mechanism***

Total pressure gives information about the chamber pressure distribution inside the chamber. It is important because it reveals the pressure drop across the chamber boundaries. A general total pressure distribution along the chamber centerline can be seen in Figure 4.26. Average total pressure value at the inlet is 7150 Pa (gage) as can be seen from the figure pressure is lost dramatically while passing through the liner holes and the pressure decreases until the end of the liner exit where it gets the average value of 2162 Pa. The average pressure drop from inlet to exit of the combustor for Aachen mechanism's case is calculated as 4988 Pa.



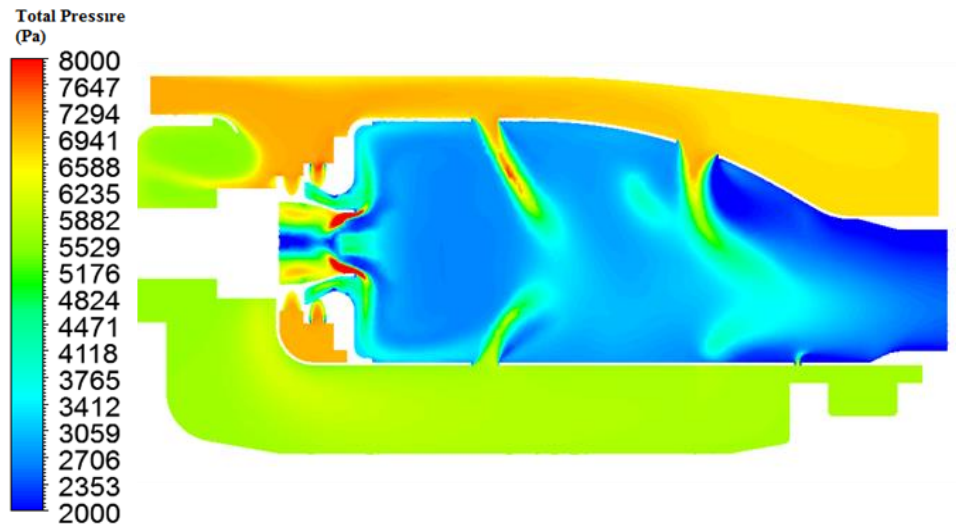


**Figure 4.26** - Total pressure distribution along centerline

Total pressure drop distribution here is given based on the inlet total pressure. The pressure drop values at the exit plane are calculated in percentages by utilizing the average inlet total pressure. The percentages of the total exit pressure values are given on Figure 4.27.

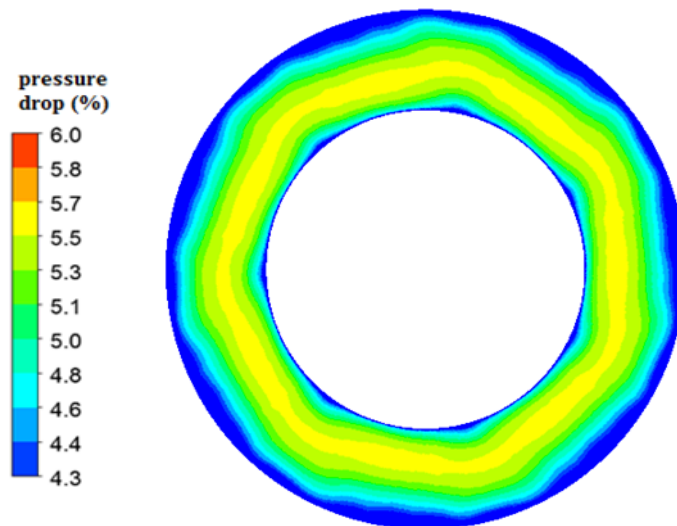


**Figure 4.27** - Pressure drop distribution at the exit plane

### ***Creck Mechanism***

A general total pressure distribution along the chamber centerline can be seen in Figure 4.28. Average total pressure value at the inlet is 6917 Pa as can be seen from the figure pressure is lost dramatically while passing through the liner holes and the pressure decreases until the end of the liner exit where it gets the average value of 2020 Pa. The average pressure drop from inlet to exit of the combustor for Creck mechanism's case is calculated as 4897 Pa. On average, the Creck mechanism predicts lower pressure drop that is consistent with the lower temperature prediction of the mechanism.

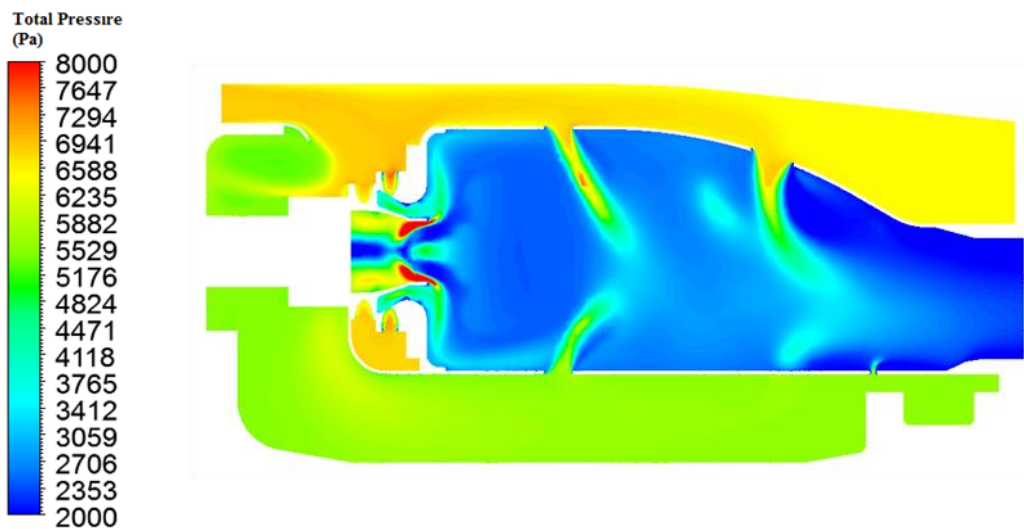


**Figure 4.28** - Total pressure distribution along centerline section

The pressure drop values at the exit plane are calculated in percentages by utilizing the average inlet total pressure. The percentages of the total exit pressure values are given on Figure 4.29.

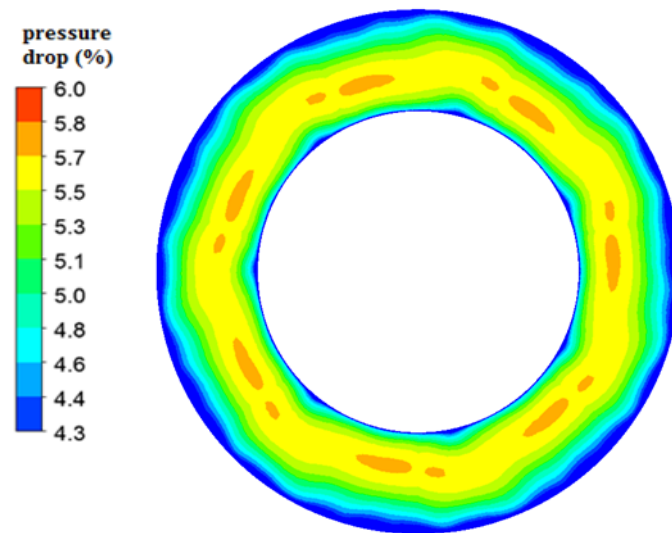


**Figure 4.29** - Pressure drop distribution at the exit plane

#### 4.1.4.5 Species Distribution Results

##### *Aachen Mechanism*

CFD analysis supplied data for the mass fraction distribution of the species inside the chamber. Here only the distribution of the  $O_2$  and  $CO_2$  are presented in Figure 4.30 for Aachen mechanism. These points are taken from the exit plane of the combustor for the single sector, so the data is limited from  $-25.7^\circ$  to  $+25.7^\circ$  angular positions. The distribution of these 2 species shows similar character with each other according to the chemistry; in the  $O_2$  rich regions  $CO_2$  levels are poor which is expected.

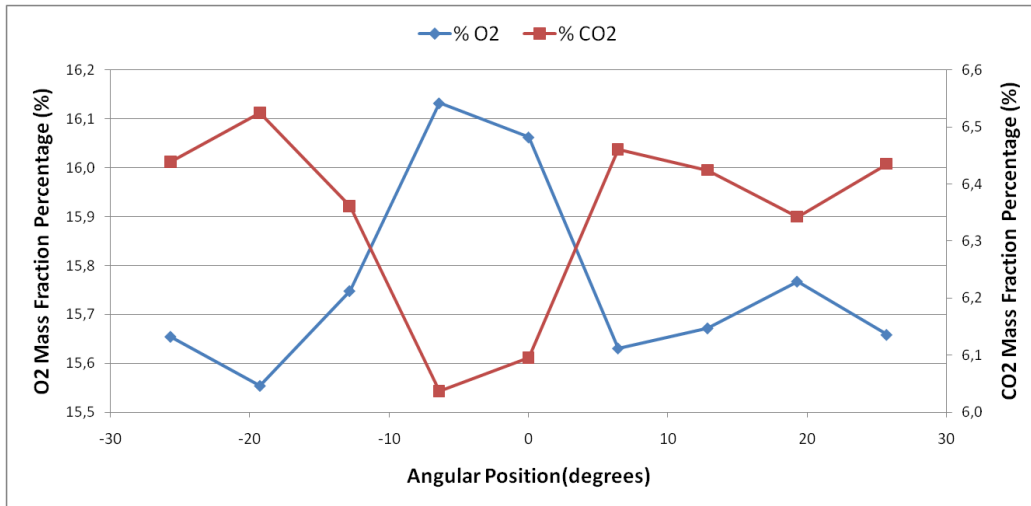


**Figure 4.30** - O<sub>2</sub> and CO<sub>2</sub> mass fraction percentage along centerline exit plane

Figure 4.31 and 4.32 show the distribution of mass fraction of fuel components C<sub>10</sub>H<sub>22</sub> and C<sub>9</sub>H<sub>12</sub>. Both of the figures shows a similar distribution, because liquid fuel is injected to the domain as a single liquid but it contains 2 different fuels having different mass fractions. Injected fuel mixes and evaporates inside the swirler and leaves the swirler by mixing with more amount of air coming from the secondary swirler exit.

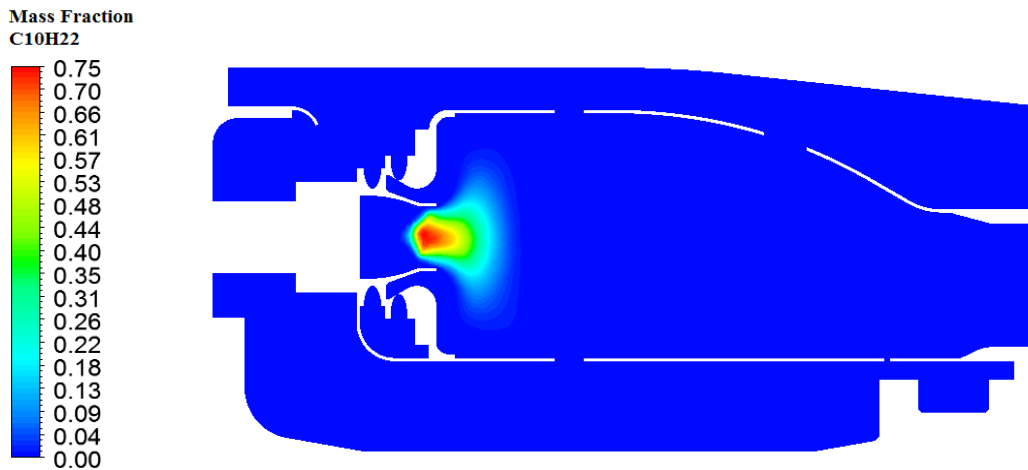


**Figure 4.31** – C<sub>10</sub>H<sub>22</sub> Mass fraction distribution along centerline section

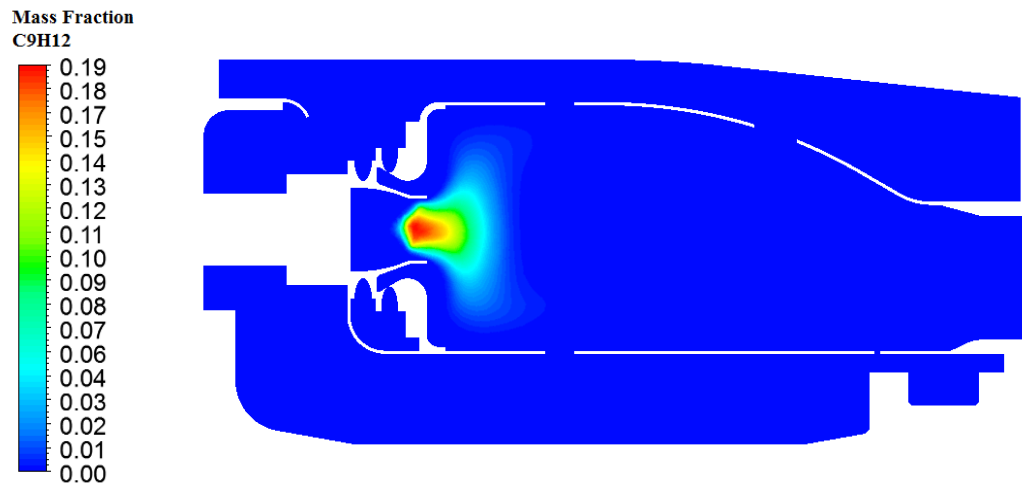


**Figure 4.32** –  $C_9H_{12}$  Mass fraction distribution along centerline section

$CO_2$  and  $H_2O$  distribution shown in Figures 4.33 and 4.34 indicates the distribution of combustion products inside domain. Although these species are the main products of the hydrocarbon combustion process, they show different character inside the chamber, this is due to the combustion rate of these products.  $H_2O$  is seem dominantly in the primary zone; conversely  $CO_2$  is more concentrated in secondary zone.

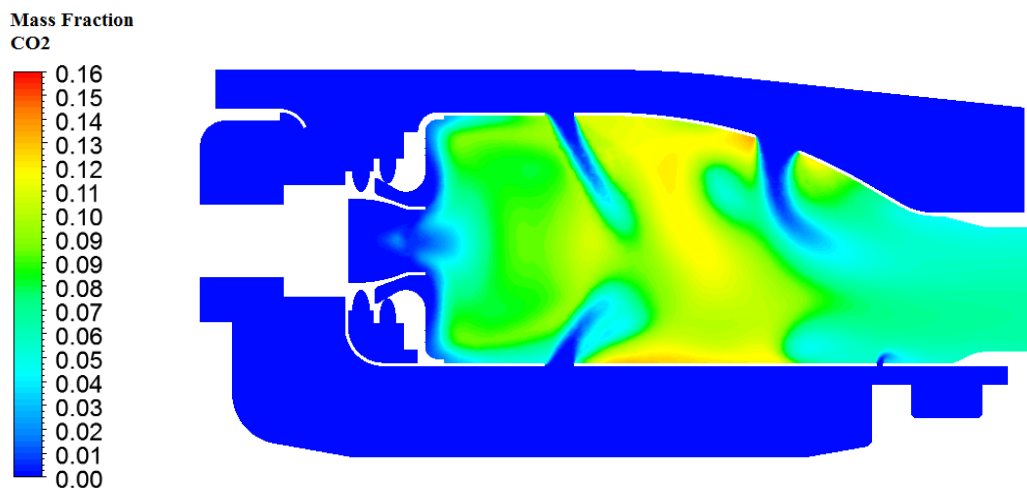


**Figure 4.33** –  $CO_2$  Mass fraction distribution along centerline section

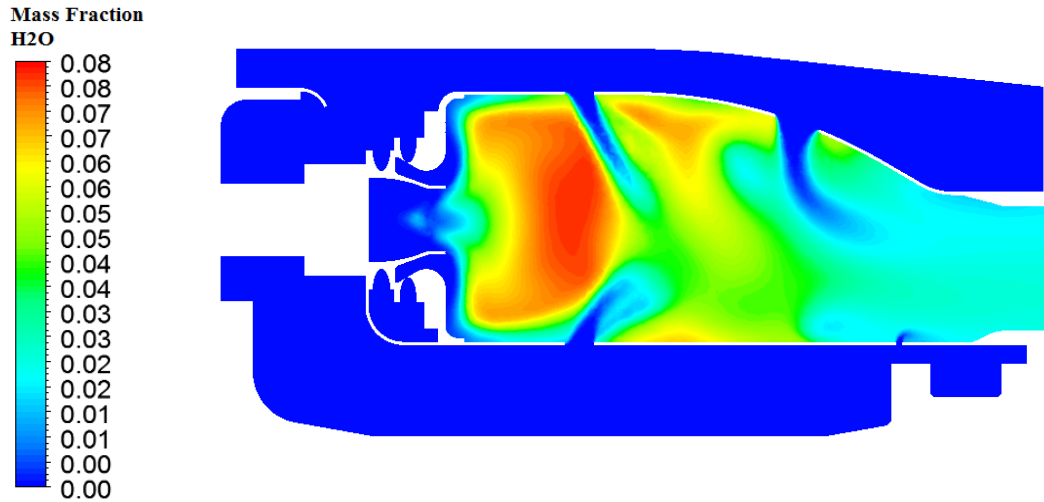


**Figure 4.34** – H<sub>2</sub>O Mass fraction distribution along centerline section

A final figure of the combustion zone is the CO isosurface for the mass fraction value of 0.1. CO concentration isosurface highlights the active regions of combustion, because it is an intermediate product of combustion. CO should be disappeared at the end of the combustor and this can be seen clearly in Figure 4.35. Figure also shows that most of the CO is found inside the primary combustion zone, which explains the lack of CO<sub>2</sub> in the primary combustion zone.

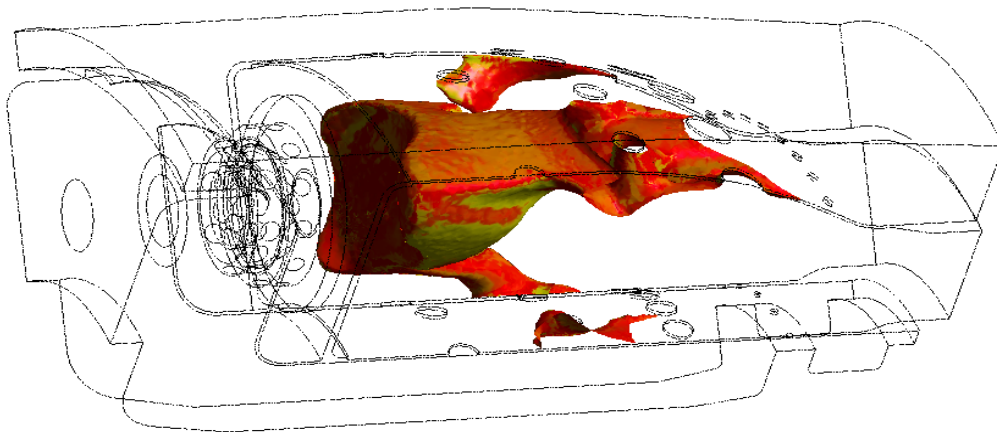


**Figure 4.35** – CO Mass fraction isosurface,  $Y_{CO}=0.1$

### ***Creck Mechanism***

The distribution of the O<sub>2</sub> and CO<sub>2</sub> are presented in Figure 4.36 for Creck mechanism. These points are taken from the exit plane of the combustor for the single sector, so the data is limited from -25.7° to +25.7° angular positions. The distribution of these 2 species shows similar character with each other according to the chemistry, in the O<sub>2</sub> rich regions CO<sub>2</sub> levels are poor which is expected.

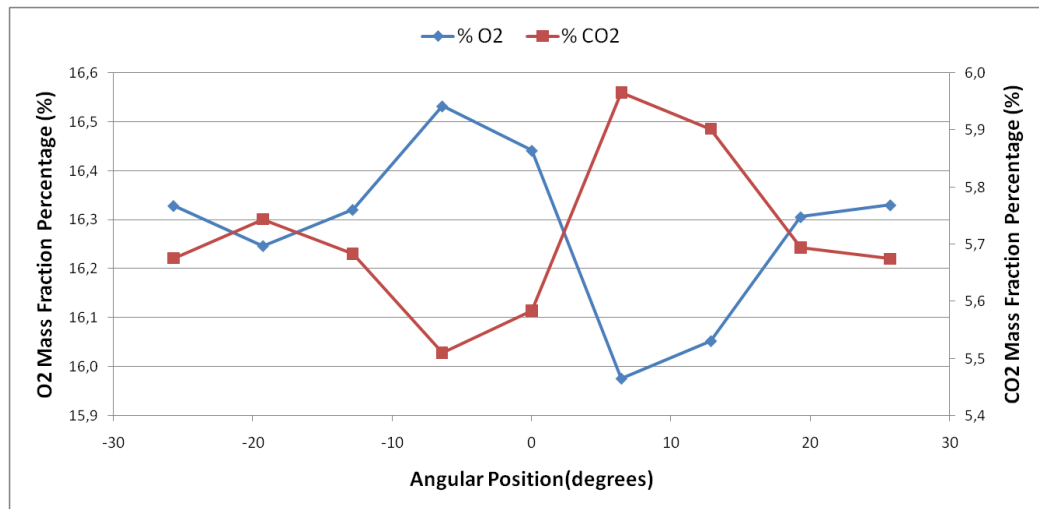


**Figure 4.36** - O<sub>2</sub> and CO<sub>2</sub> mass fraction percentage along centerline exit plane

Figure 4.37 and 4.38 show the distribution of mass fraction of fuel components C<sub>10</sub>H<sub>22</sub> and C<sub>9</sub>H<sub>12</sub> for Creck mechanism's analysis. Both of the figures shows a similar distribution, because liquid fuel is injected to the domain as a single liquid but it contains 2 different fuels having different mass fractions. Injected fuel mixes and evaporates inside the swirler and leaves the swirler by mixing with more amount of air coming from the secondary swirler exit.

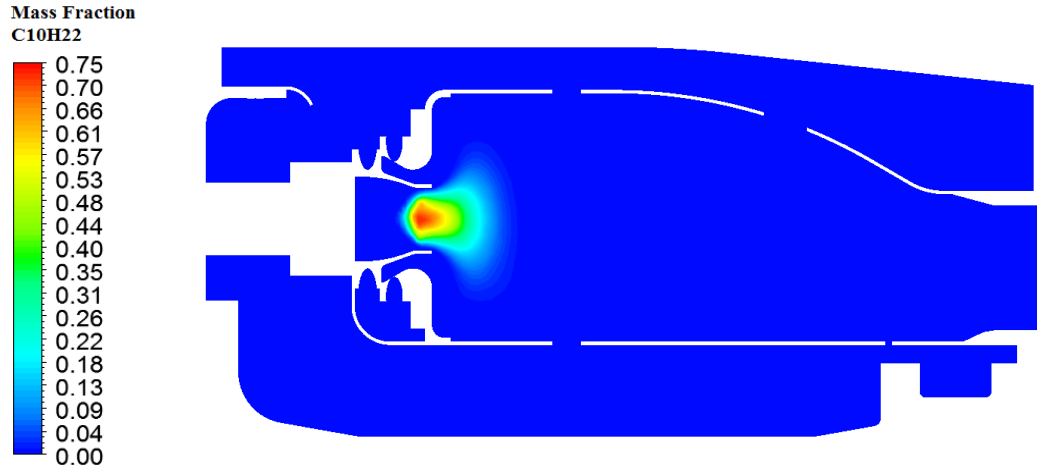


**Figure 4.37** –  $C_{10}H_{22}$  Mass fraction distribution along centerline section

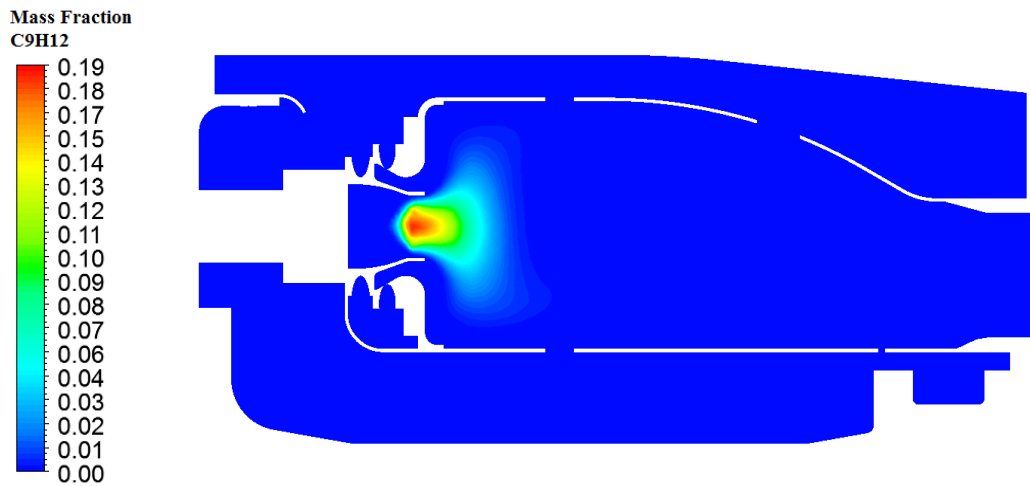


**Figure 4.38** –  $C_9H_{12}$  Mass fraction distribution along centerline section

$CO_2$  and  $H_2O$  distribution shown in Figures 4.39 and 4.40 indicates the distribution of combustion products inside domain. Their distribution is very similar with the results of the Aachen mechanism's analysis. There is no distinct difference among the results for the product distribution.



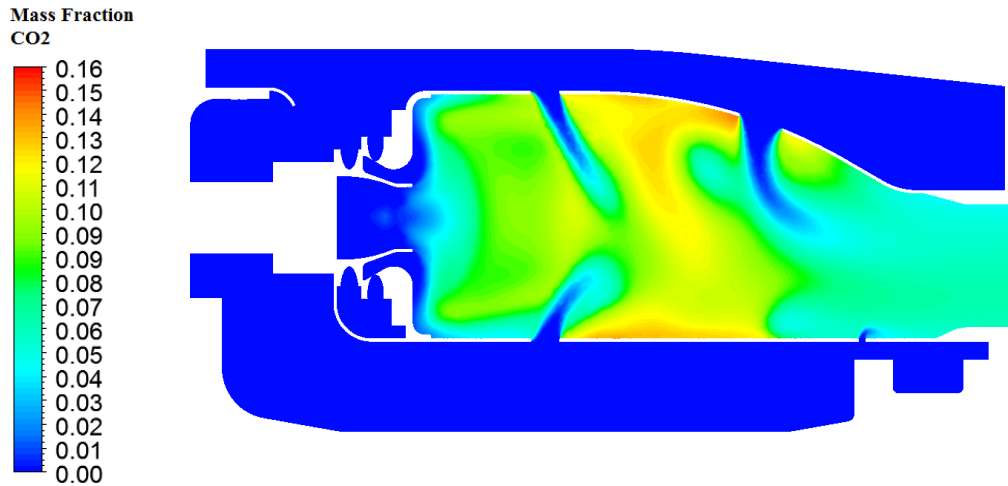


**Figure 4.39** – CO<sub>2</sub> Mass fraction distribution along centerline section

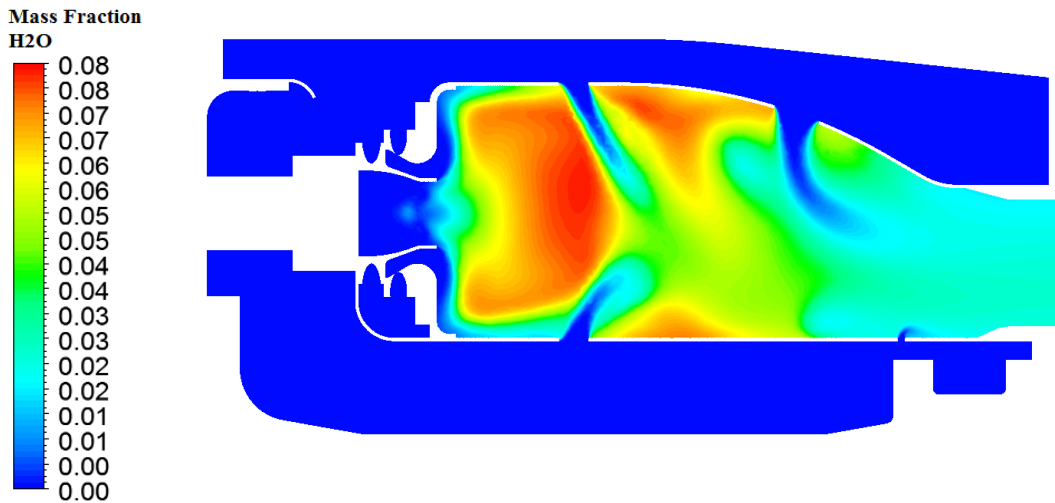


**Figure 4.40** – H<sub>2</sub>O Mass fraction distribution along centerline section

CO isosurface for the mass fraction value of 0.1. CO concentration is given in Figure 4.41 for Creck mechanism. The isosurface highlights the active regions of combustion, because it is an intermediate product of combustion. CO should be disappeared at the end of the combustor and this can be seen clearly in Figure 4.41. The appearance of high concentration of CO also shows that the reaction continues at the primary and secondary regions.

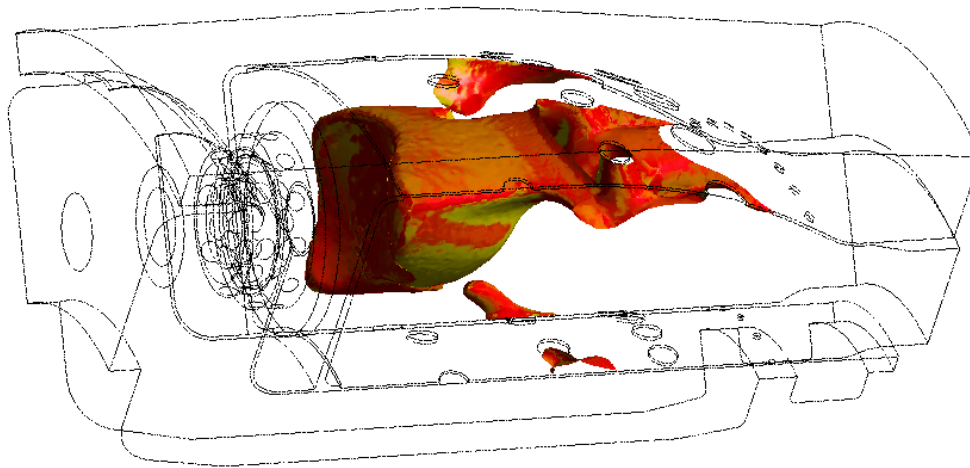


**Figure 4.41** – CO Mass fraction isosurface,  $Y_{CO}=0.1$

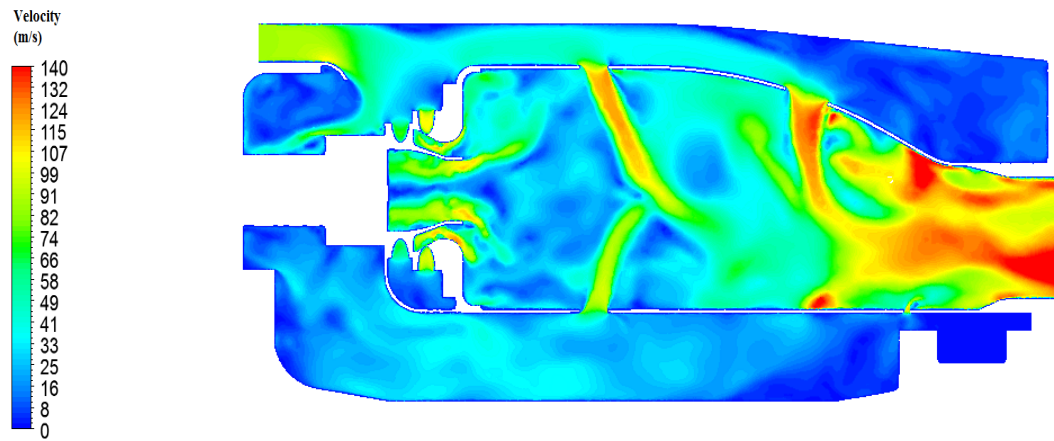
#### **4.1.5 SAS-CFD Results**

Unsteady analysis of the combustor are also performed and presented here. The unsteady results are conducted by using Scaled Adaptive Simulation method. The method is relatively new and an alternative to the computationally costly methods like LES and DES. The details of the method are presented in Chapter 1. The same settings in the analysis are used except that SAS method is utilized for handling of the turbulence. A time step of  $10^{-5}$  sec is utilized to guarantee Courant condition inside the domain. The results presented here show the instantaneous and time averaged values. Note that the presented results for SAS analysis are obtained by utilizing Aachen mechanism only.

##### **4.1.5.1 Velocity Results**

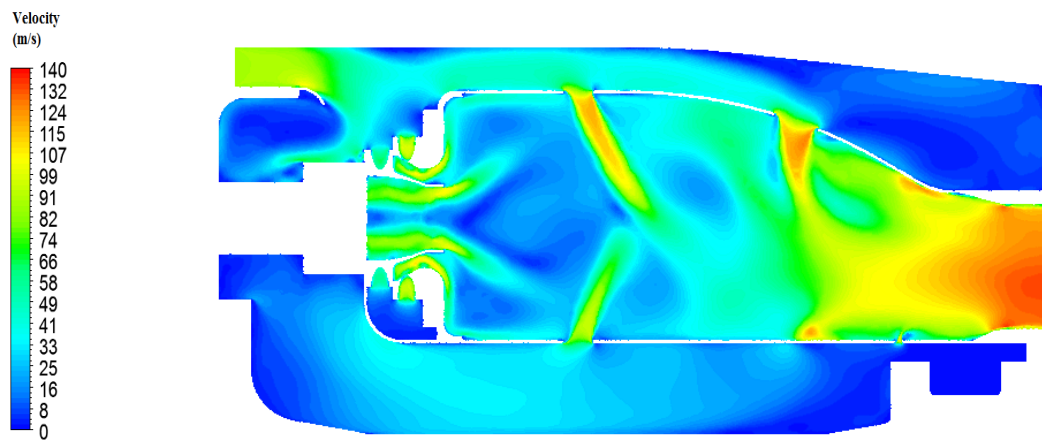
Instantaneous velocity distribution is shown in Figure 4.42 for the centerline section of the combustor. Although instantaneous figures don't give an overall character presenting data, they reveal different flow patterns and instantaneous flow figures that cannot be seen in an averaged analysis. They can also show short time velocity

and pressure waves moving inside the chamber. Moreover, changing localized flow characteristics give a more realistic distribution at the exit.



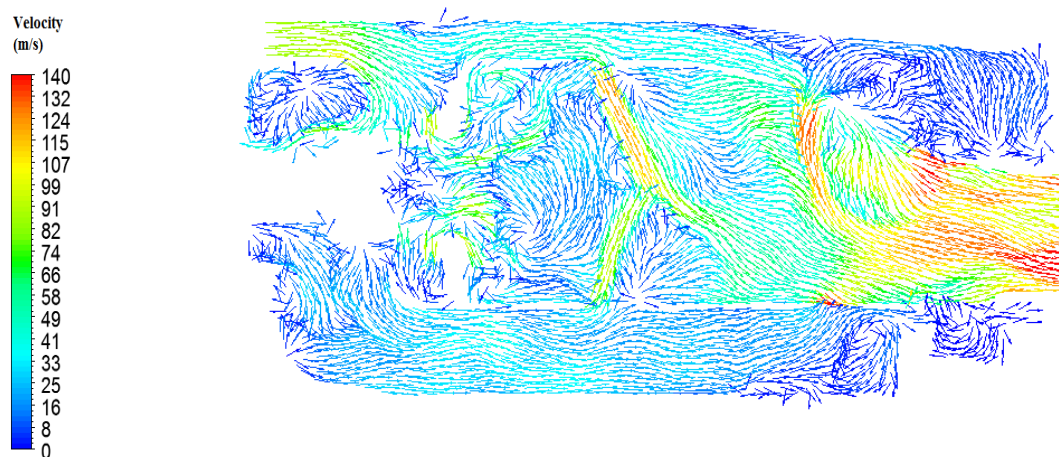
**Figure 4.42** - Velocity distribution along centerline section - instantaneous values at  $t=0.02$  sec

Figure 4.7 shows the time averaged mean of the data for 0.02 second which is approximately 2000 iterations. The average data is comparable with the RANS results and draw representative performance figures. The figures are not very different from the RANS results given in Section 4.1.4. This means the results shown are approaching to RANS results by average.



**Figure 4.43** - Velocity distribution along centerline section - time averaged velocity distribution

Velocity vector distribution along the centerline section in Figure 4.44 shows the instantaneous vectors and as can be seen they are not regular and swirling movement cannot be clearly observed. This is also more realistic and expected.



**Figure 4.44** - Velocity vector distribution along centerline section- instantaneous values at  $t=0.02$  sec

The exit velocity values at the instantaneous figure shows higher magnitudes of velocity however when the average values are inspected in Figure 4.46, they are

lower in average. This means that the velocity values are changing at the exit region and higher and lower velocity cycles comes after each other. This reveals the unsteady character inside the chamber.

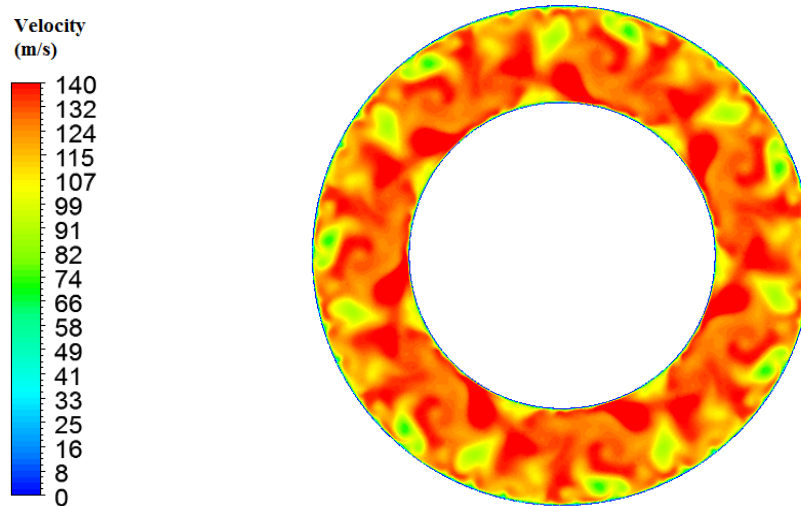


**Figure 4.45** - Velocity distribution at the exit plane - instantaneous values at  $t=0.02$  sec

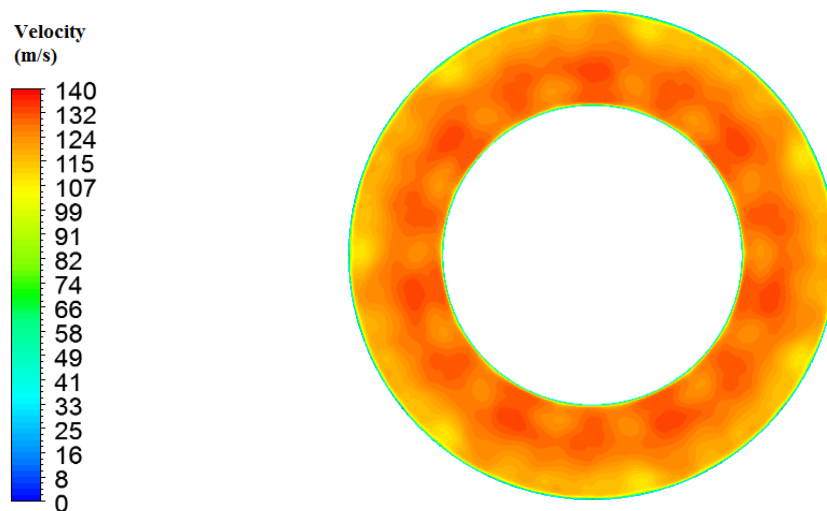


**Figure 4.46** - Velocity distribution at the exit plane - time averaged velocity distribution

#### 4.1.5.2 Flow Streamlines

Streamlines of the flow particles released from the inlet of the flow field is given in Figure 4.47. As can be seen from the figure the streamlines are not uniform and a lot of directional variety can be observed in the combustion zone. The directional behavior is different from the averaged results that are presented in RANS results.

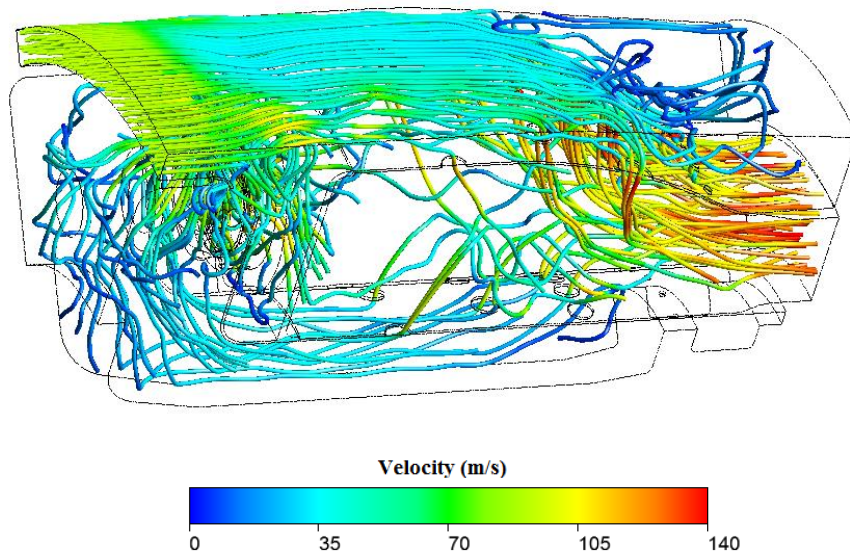


**Figure 4.47-** Streamlines emanating from the inlet - instantaneous values at  $t=0.02$  sec

#### 4.1.5.3 Temperature Results

Temperature figures shown in Figure 4.48 and 4.49 shows the distribution of temperature along the centerline section for instantaneous and time-averaged data respectively. Instantaneous figure shows higher temperature compared to the time averaged value this proves the time dependent fluctuating character of the chamber. The trend of hot zones and combustion character is principally the same as the RANS results. However exit temperature prediction for the time averaged SAS result is 1140 K

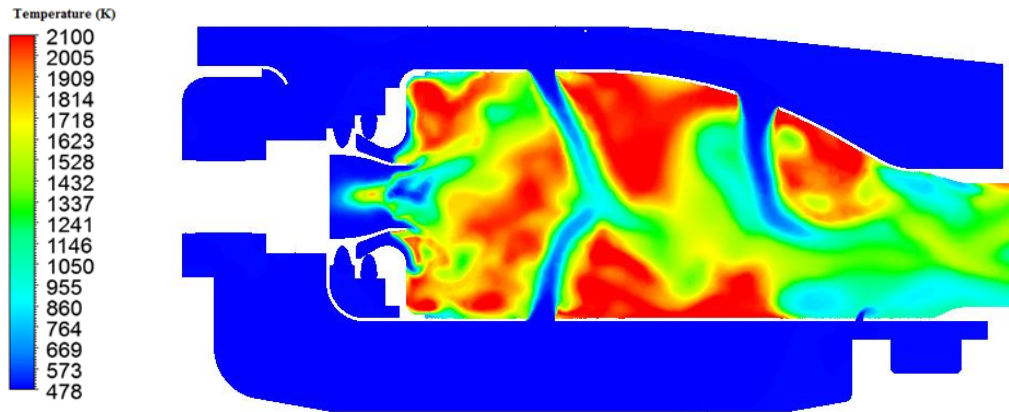


**Figure 4.48** - Temperature distribution along centerline- instantaneous values at  $t=0.02$  sec

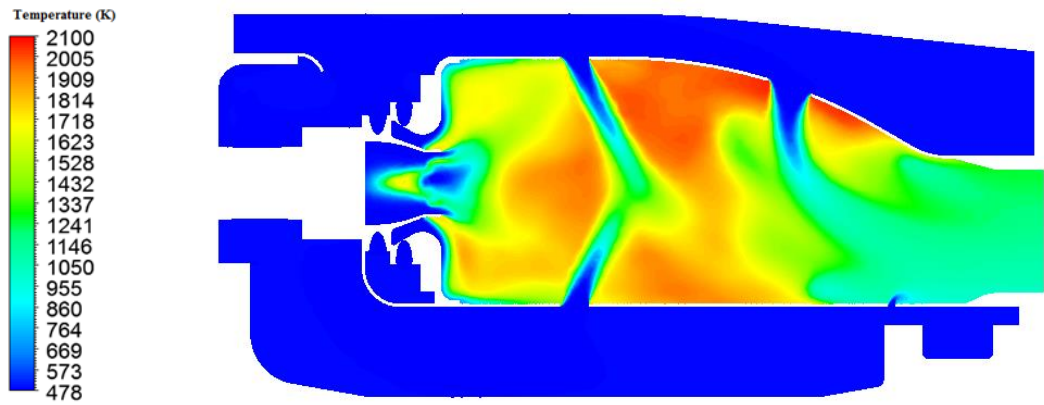


**Figure 4.49** - Temperature distribution along centerline- time averaged values

The exit temperature fluctuation can be seen in Figure 4.50. High temperature values are spread along the chamber in the radial direction. In average, they are concentrated near the outer liner of the chamber as it is shown in Figure 4.51.



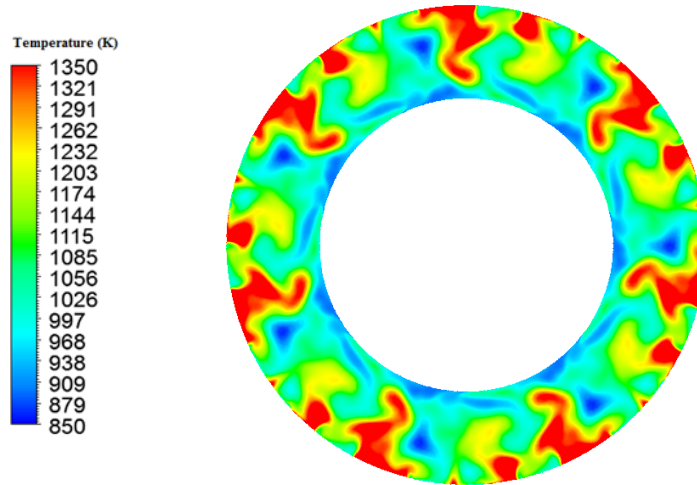


**Figure 4.50** - Exit plane temperature distribution- instantaneous values at  $t=0.02$  sec

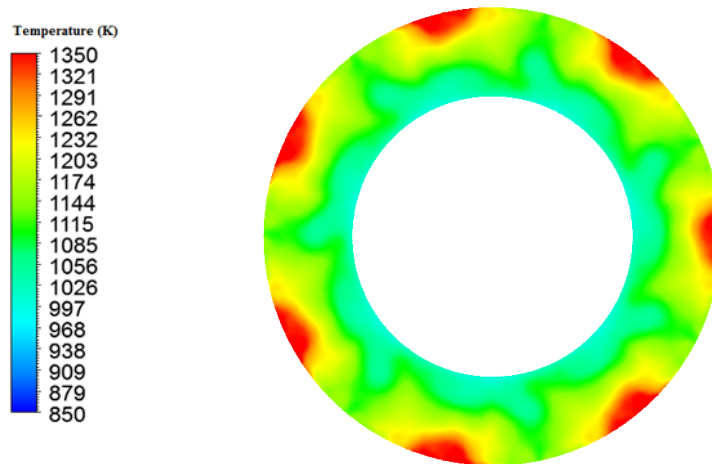


**Figure 4.51** - Exit plane temperature distribution- instantaneous values at  $t=0.02$  sec

A final figure of instantaneous CO isosurface for the mass fraction value of 0.1 is presented in Figure 4.52. As it is mentioned previously the high concentration CO regions defines the reaction zones and gives the boundary of active combustion regions. The instantaneous figure differs from the RANS figure in terms of the spread of the isosurface more inside the chamber. This means a larger zone of combustion instantaneously. And this also reveals the transient character of the chamber.



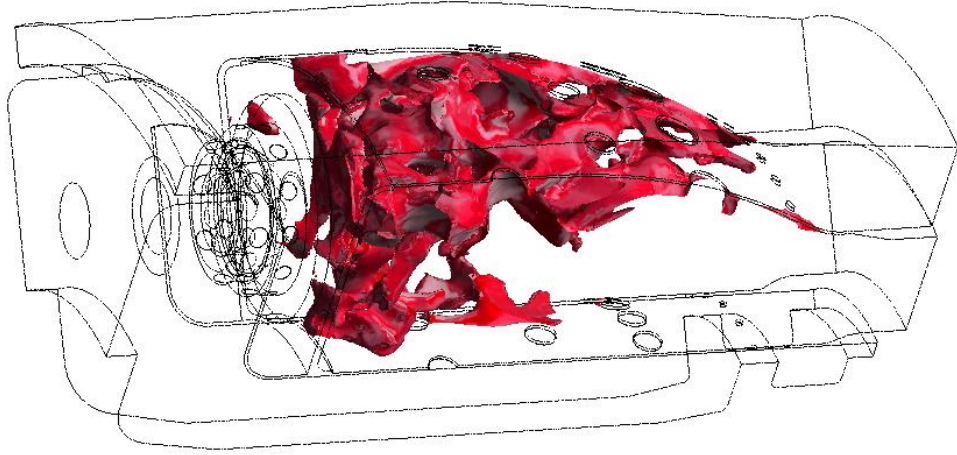


**Figure 4.52** – CO Mass fraction isosurface,  $Y_{CO}=0.1$

## 4.2 Experimental Verification

### 4.2.1 Experiment Set-up

#### 4.2.1.1 General

Combustor test facility located in TEI headquarters is consists of a compressor, heater, plenum, fuel system, test section and exhaust system. The sketch of the test system is shown in Figure 4.53.

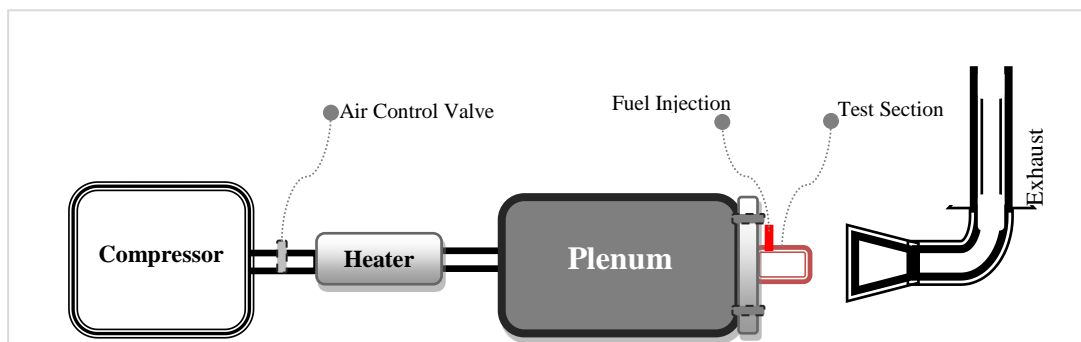


**Figure 4.53 - Combustion Chamber Performance Test Set-up Sketch**

The facility is an atmospheric test facility which means that the exit of the combustor is directly opened to the atmosphere and there is no physical link between the combustor exit and the exhaust system. This kind of test systems doesn't require high compressor pressures. And they allow scanning the exit section parameters. It is also possible to scan inside sections of combustors buy using special laser probe heads and camera systems however these equipment are not readily available yet. Hence, in this study only exit section measurements are presented.

Air pressurized and injected into the system by the compressor. The compressor has a capacity of 1.6 kg/s with a max pressure of 10 bars. There is a valve at the air line for controlling of the air flow, heater section is a cylindrical pipe section with a heater inside. After the heater section air is well mixed and temperature distribution is homogenous at the section exit. The plenum section is a large volume chamber which decelerates the airflow and very low air velocities are obtained, in other

words, the plenum can be assumed as a static chamber. The low velocities at the plenum exit causes a purely pressure injection from the entrance of the combustor. This prevents the non-uniform flow distribution from the holes of the combustor due to high speed flow. The photos of the major parts of the test set-up are shown in Figure 4.54.

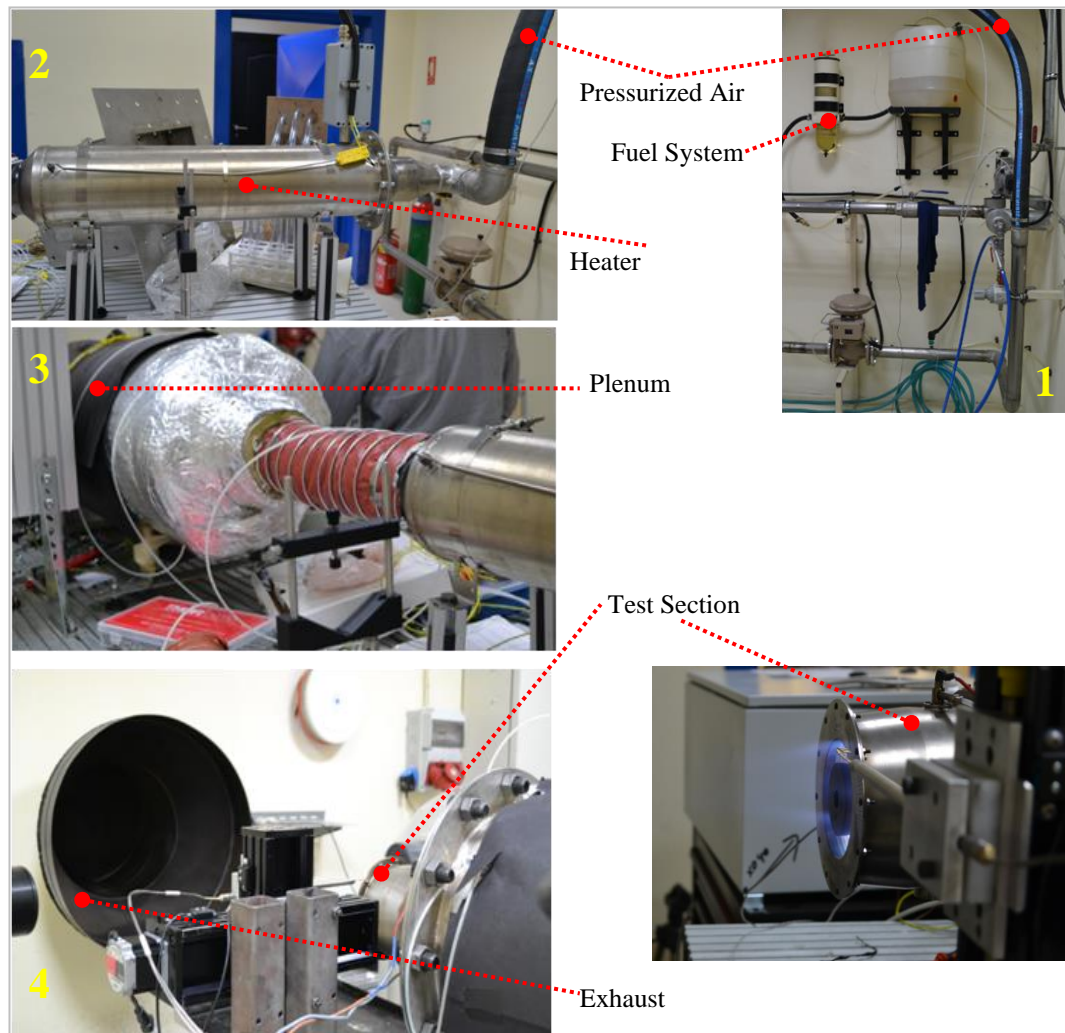


**Figure 4.54 - Test Set-up Photos**

Test section resembles the combustion chamber as in the engine. It includes the liner and casing. The casing includes ports for standard engine equipment which are the fuel line main entrance and the igniter port. In addition to this casing includes the instrumentation pieces on it. The instrumentation ports measures static pressure, total pressure and temperature at circumferential position of the chamber inlet. Multiple

measurement ports (three and four probes) are utilized to obtain average inlet temperature and pressure. Utilization of multiple probes at a single point increases the measurement accuracy by averaging. The test section and instrumentation at chamber inlet are shown in Figure 4.55.

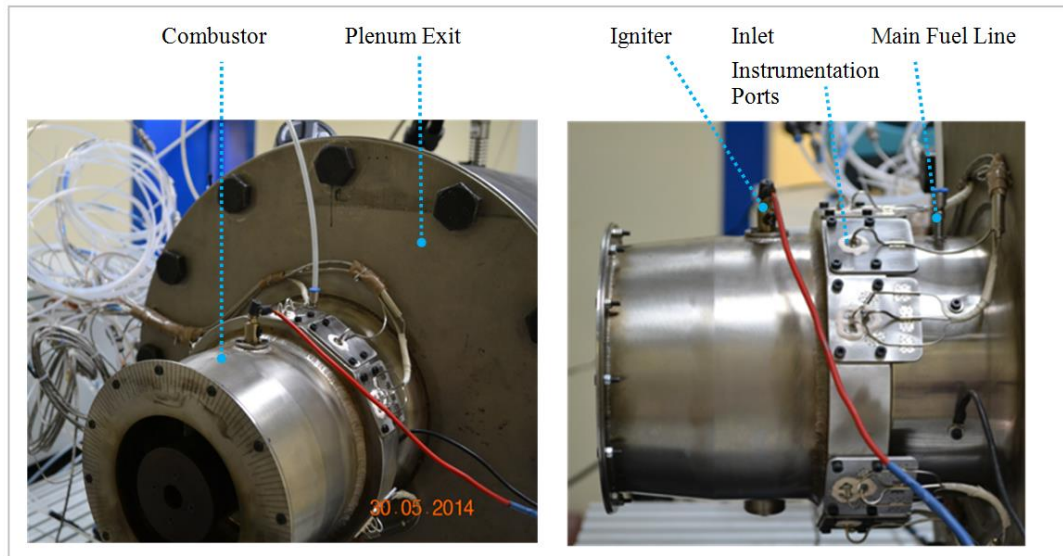


**Figure 4.55 - Test Section and Instrumentation**

The exit of the combustion chamber is scanned by the help of the traverse mechanism as shown in Figure 4.56. The minimum step of the traverse is  $1/200$  mm. Traverse mechanism moves the measurement probe in x and y directions only. Pre-defined coordinates of the exit section is given into the computer and during the tests traverse moves the probes in these locations. For increasing measurement accuracy, rakes composed of three and four probes are utilized for temperature and pressure measurements respectively. For a point measurement at a location multiple readings are taken by the rakes. Afterwards, the average of these measurements is taken for the value of that point.

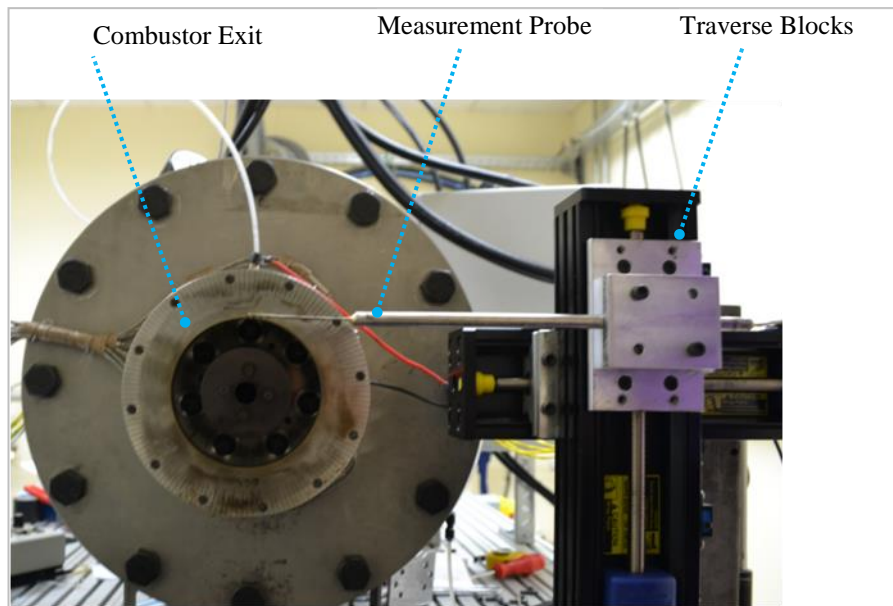


**Figure 4.56 - Traverse Blocks and Measurement Probe**

#### **4.2.1.2 Measurement Instrumentation**

As it is mentioned in the previous section, combustor basic performance test rig measures the fundamental chamber parameters. These are chamber inlet and exit temperature, pressure and chamber exit section species distribution. Following sensors are used for measuring these parameters:

#### **4.2.2 Test Objective**

Combustion chamber test facility focused on the performance of the combustion chamber. During the tests some of the parameters are fixed and by this way the test system is set to a specific operation condition. Other parameters are measured and the performance evaluation is applied. The parameters that are fixed to an operating point are the fuel mass flow rate, air mass flow rate, inlet pressure and inlet temperature. The basic measurements taken from the inlet of the combustor are the inlet static pressure, total pressure and temperature. From the exit of the combustor temperature, total pressure and species concentration are taken by the help of a traverse system. These basic data gives information about the combustor pressure loss, exit section temperature distribution, exit section total pressure distribution and

exit section species distribution. By using the temperature and exit species data it is possible to obtain the chamber efficiency indirectly. A final method used for evaluating the performance of the combustion chambers is the thermal paint application. Thermal paint is applied on the outer walls of the liner by this way the steady temperature distribution on the liner walls is obtained. Thermal paint application is especially useful to determine the hotspot on the combustor surface.

### 4.2.3 Test Methodology

During the performance tests firstly the operating conditions of the test rig is set up. The fixed parameters during the test are given on Table 4.4, these parameters can be named as boundary conditions as well. Combustion chamber boundary conditions are shown on the table.

**Table 4.4 – Combustion Chamber Operating Conditions**

Air mass flow rate (kg/s)	0.202
Fuel mass flow rate (kg/s)	0.00406
Combustor inlet temperature (K)	481.7
Combustor inlet pressure (Bar)	1.15
Air/Fuel Ratio	49.7

Ignition of the combustion chamber begins with heating of the incoming pressurized air. After the temperature of the incoming air reach to the desired operating point. The fuel main control valve is opened, just at the same time the igniter is activated. To guarantee the ignition at the beginning, the air mass flow is set to a lower level during start up. By this way it is possible to obtain a rich mixture inside the main combustion zone. The rich ignition condition and the lag between the fuel injection and ignition cause the flame to elongate out of the chamber but for a very short time. This situation is shown in Figure 4.57.



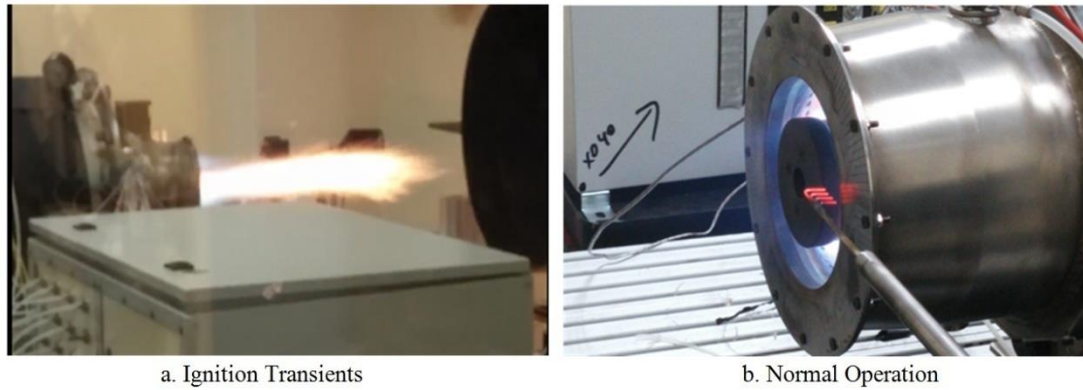


**Figure 4.57 - Ignition Operation and Normal Operation of the Chamber**

After the ignition the air mass flow rate is set to the normal operation level. And chamber is left operating during several minutes for the test system come to thermal equilibrium. After the temperature values from several locations of the chamber come to the equilibrium position, the data recording period begins.

During the tests the data system records according to the position of the traverse system. When the traverse system is operational it goes to its 1<sup>st</sup> position and the data recording begins and lasts for 1 minute during this time data is taken simultaneously by all of the probes attached. After 1 minute traverse goes to the 2<sup>nd</sup> position and the process goes on this way. The following parameters are recorded during the tests:

- Chamber inlet temperature
- Chamber inlet static pressure
- Chamber inlet total pressure
- Chamber exit temperature profile
- Chamber exit total pressure loss profile
- Chamber exit species concentration profile

Chamber inlet measurements are taken from 3 different circumferential positions. Actually 1 location could be enough for an ideal system, but increasing the number of measurement points will allow averaging of the inlet data and also provides back up in case of a sensor failure. Chamber outlet is scanned by utilizing a traverse mechanism as mentioned before.

#### 4.2.4 Test Results

Exit section measurements are taken by the help of the traverse system. Traverse system scans the exit of the combustion chamber by moving in x and y directions. Traverse first moved to a reference position which is the zero of the measurement grid. This point is shown in Figure 4.58. The other points are defined with respect to the zero. The list of measurement points are given on Table 4.5.

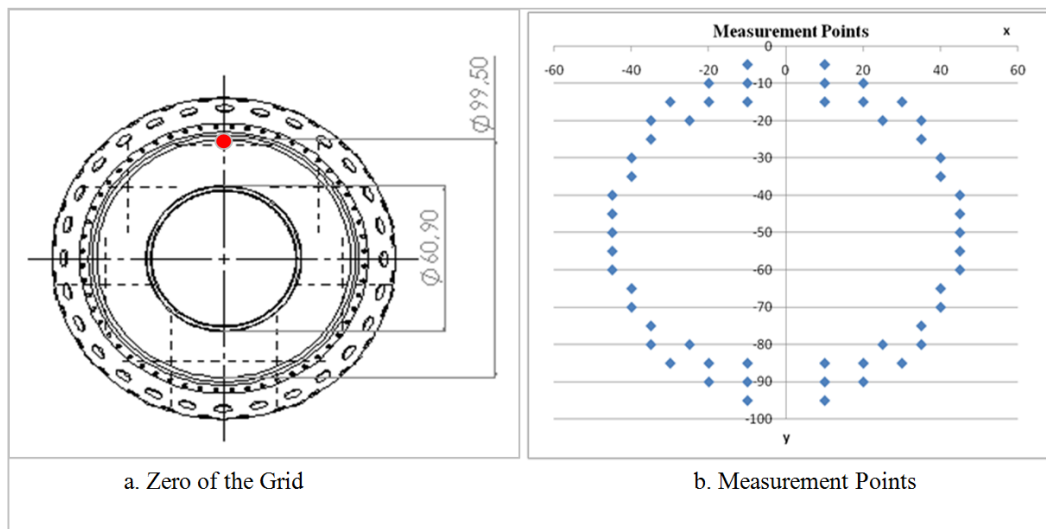


**Figure 4.58** - a. Zero of the Measurement Grid b. Measurement Points



**Table 4.5** – The List of Measurement Points at the Chamber Exit

Position	x (mm)	y(mm)	
0	-10	5	Right Hand Side Points
1	-10	-5	
2	-10	-10	
3	-10	-15	
4	-20	-10	
5	-20	-15	
6	-25	-20	
7	-30	-15	
8	-35	-20	
9	-35	-25	
10	-40	-30	
11	-40	-35	
12	-45	-40	
13	-45	-45	
14	-45	-50	
15	-45	-55	
16	-45	-60	
17	-40	-65	
18	-40	-70	
19	-35	-75	
20	-35	-80	
21	-30	-85	
22	-25	-80	
23	-20	-85	
24	-20	-90	
25	-10	-85	
26	-10	-90	
27	-10	-95	
54	10	-5	Left Hand Side Points
53	10	-10	
52	10	-15	
51	20	-10	
50	20	-15	
49	25	-20	
48	30	-15	
47	35	-20	
46	35	-25	
45	40	-30	
44	40	-35	
43	45	-40	
42	45	-45	
41	45	-50	
40	45	-55	
39	45	-60	
38	40	-65	
37	40	-70	
36	35	-75	
35	35	-80	
34	30	-85	
33	25	-80	
32	20	-85	
31	20	-90	
30	10	-85	
29	10	-90	
28	10	-95	

#### 4.2.4.1 Temperature Measurements

Temperature measurements are taken by utilizing single rake composed of 3 measurement heads. The distance between each probe is about 5 mm. By utilizing 3 heads, a total of  $54 \times 3 = 162$  points are scanned. At each location traverse waits for 1 minute and time average of the data is utilized. After applying correction to the temperature data set the exit temperature profile can be obtained as in Figure 4.59. The average exit temperature is obtained as 1130 K.

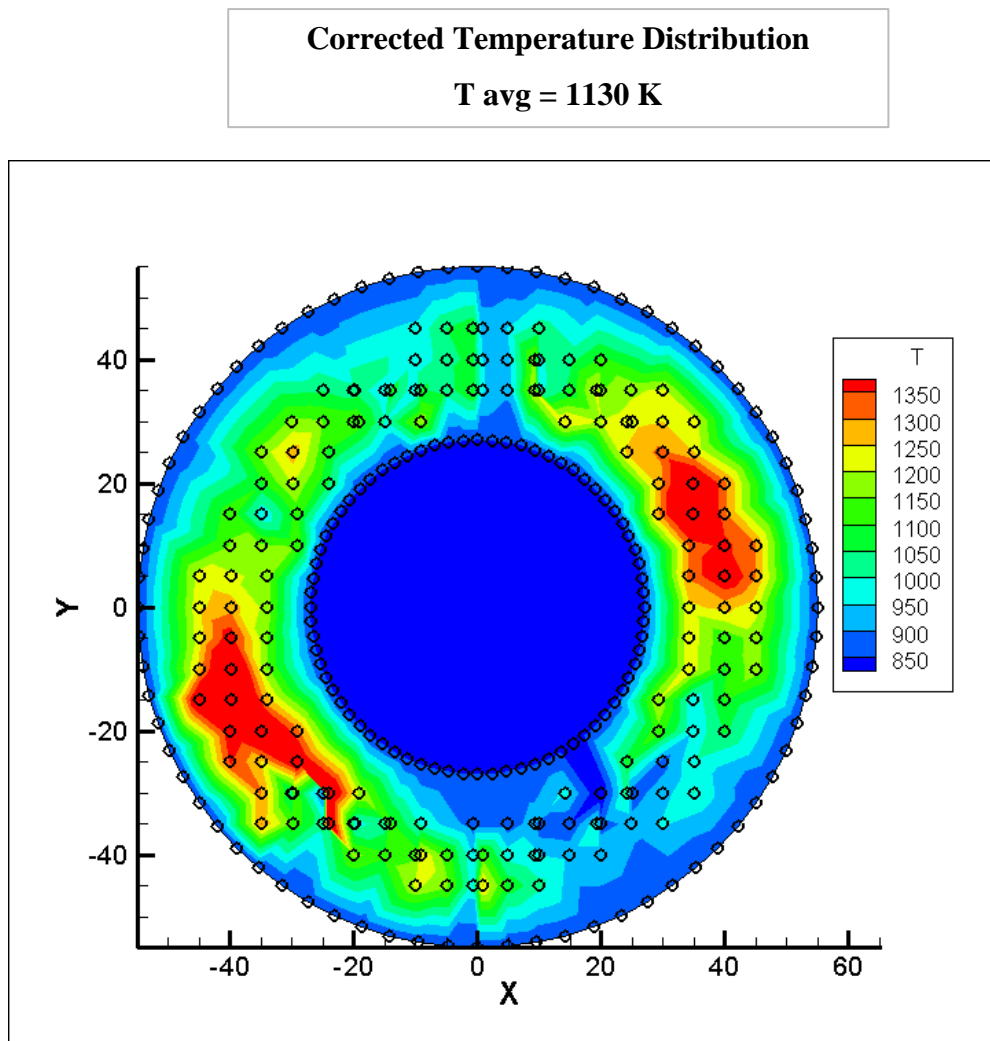


**Figure 4.59 - Experimental Exit Temperature Distribution**

#### 4.2.4.2 Total Pressure Loss Measurements

Total Pressure measurements are taken by utilizing single rake composed of 3 measurement heads. The distance between each probe is about 5 mm. By utilizing 3 heads total of  $54 \times 3 = 162$  points are scanned. At each location traverse waits 1 minute and time average of the data is utilized. The total pressure drop profile in percentage can be obtained as in Figure 4.60. The average exit pressure drop percentage is obtained as 5.65 .

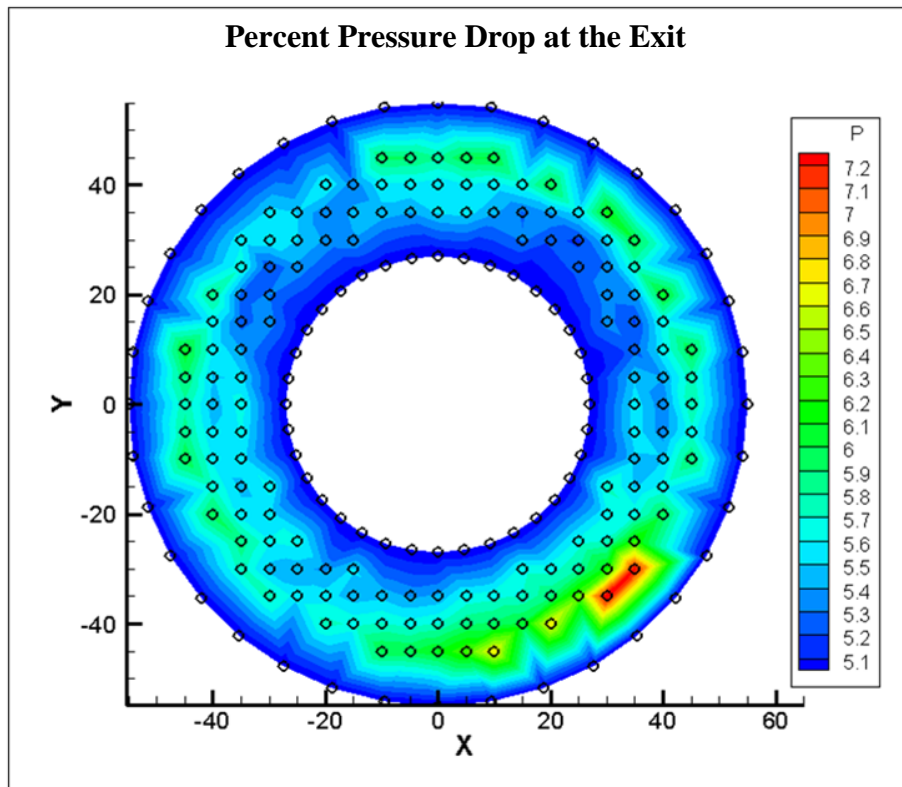


**Figure 4.60** - Percent Pressure Drop at Combustion Chamber Exit

#### 4.2.4.3 Species Measurements

Species concentration distribution is measured by using the traverse system. It differs from the previous measurements by only considering the centerline position. The probe moves along the centerline of the exit section at angular steps of  $10^\circ$ . At each location traverse waits 1 minute and time average of the data is utilized.  $O_2$ ,  $CO_2$ ,  $CO$ ,  $NO_x$ ,  $C_xH_y$  and temperature can be measured by the probe of the species measurement system. Gas analyzer is a separate unit and it is a compact model of TESTO. It can store and print the measurement by getting the average internally. In Figure 4.61 distribution of  $O_2$  and  $CO_2$  are plotted against angular position. In Figure 4.62 temperature and  $NO_x$  values are plotted against angular position. Finally in Figure 4.63 distribution of  $CO$ , Hydrocarbon and  $NO_x$  values are plotted against angular position.

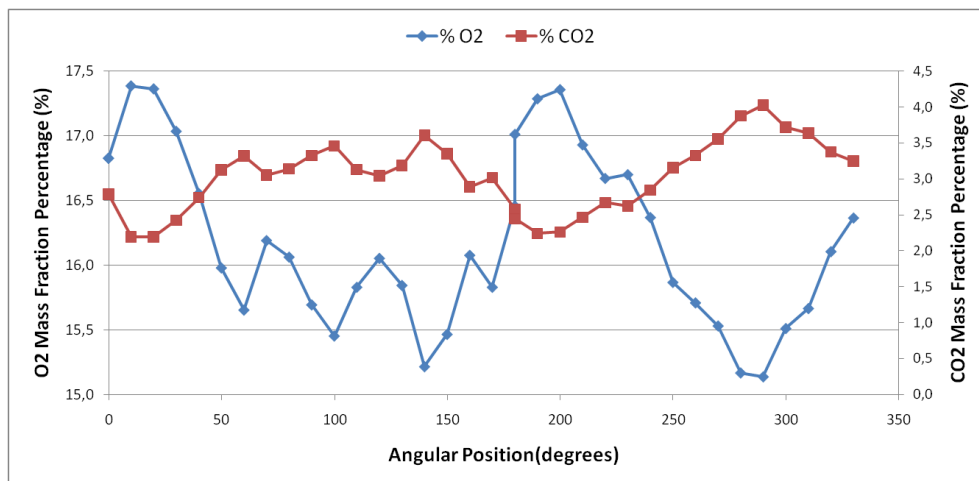


**Figure 4.61** -  $O_2$  and  $CO_2$  Mass Fraction Percentage wrt. Angular Position

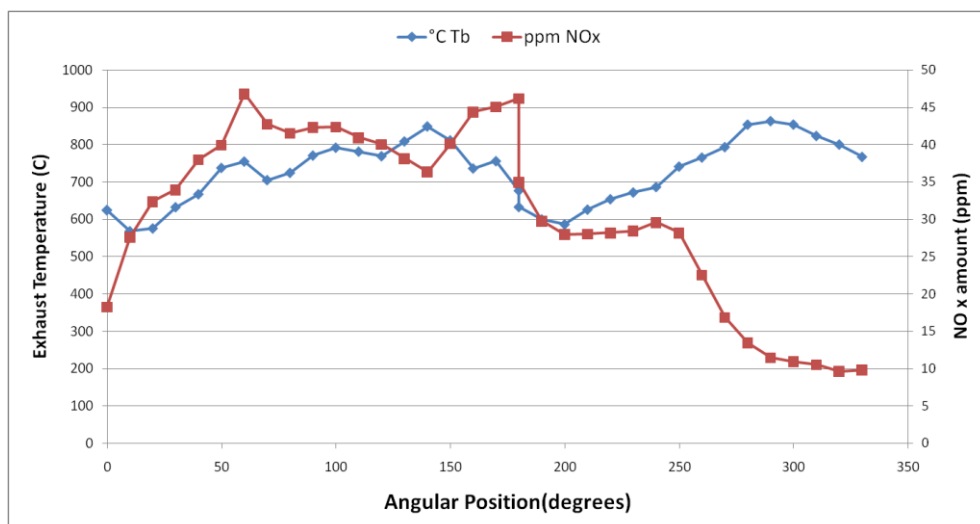


**Figure 4.62** - Centerline Temperature and NO<sub>x</sub> amount in ppm wrt. Angular Position

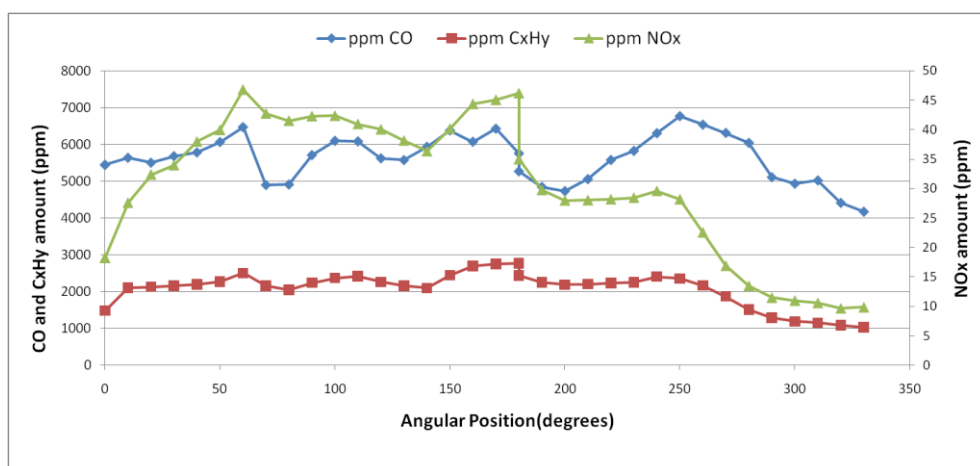


**Figure 4.63** - CO, C<sub>x</sub>H<sub>y</sub>, NO<sub>x</sub> amount in ppm wrt. Angular Position



## CHAPTER 5

### APPLICATION: A COMBUSTOR DESIGN TOOL

#### 5.1 Combustor Design Methodology

Combustion chamber design is a complex task to achieve; the complexity comes from the highly non-linear character of the combustor. Desirable characteristics of a gas turbine combustor are having high combustion efficiency, high stability character, low pressure loss and an exit temperature profile that has a convenient pattern to extend the life of the turbine blades. Unlike the traditional aerodynamic bodies the internal structure of the combustor is complex and composed of many tiny details. By adding the combustion phenomena as an additional source of complexity, the flow field distribution and flow split through the combustor holes becomes hard to predict. However, the design of a gas turbine combustor from scratch starts from the prediction of the combustion volume and then all other details are built on top of it.

#### 5.2 Basic Combustor Design Parameters

In order to decide the combustor dimensions combustor volume related parameters are used. The volume of the combustor mentioned in these calculations is the main combustion volume that is the liner or the flame tube. Annulus region between the liner and casing are not counted as the combustor volume.

*Combustor Loading:* Combustor loading is an empirical formula that is given in equation (141), [2].

$$CL = \frac{\dot{m}_{31}}{V \cdot P_{31}^{1.8} \cdot 10^4 (0.00145 \cdot (T_{31} - 400))} \quad (141)$$

CL: combustor loading (kg/(s atm<sup>1.8</sup>m<sup>3</sup>))

$\dot{m}_{31}$ : mass flow entering to the combustor (kg/s)

$P_{31}$ : inlet pressure of the combustor (atm)

$T_{31}$ : inlet temperature (K)

$V$ : liner volume (m<sup>3</sup>)

According to Walsh et al. [2] combustor loading at sea level static rating should be less than 10 kg/s atm<sup>1.8</sup>m<sup>3</sup>, and it also added that lower values than the limit are preferred. As can be seen from the formula combustor loading relates the basic performance parameters like mass flow, inlet temperature, inlet pressure with the volume. And the volume is the key parameter for setting the level of combustor loading. Because all other parameters are cycle related and barely can be changed. A high combustor loading means large amount of energy is released in a small volume, which is problematic and undesirable.

*Combustion Intensity:* Another important design parameter is the combustor intensity. This parameter also sets a restriction for combustor volume. However the basic parameters utilized are different than combustor loading. Empirical formula for combustion intensity is given in equation (142) [2].

$$I = \frac{\dot{m}_f \cdot \eta_c \cdot LHV}{(P_{31} \cdot V)} \quad (142)$$

$I$ : combustion intensity (MW/m<sup>3</sup> atm)

$\dot{m}_f$ : fuel mass flow rate (kg/s)

$\eta_c$ : combustion efficiency

$LHV$ : fuel lower calorific value (MJ/kg)

$P_{31}$ : inlet pressure of the combustor (atm)

$V$ : liner volume (m<sup>3</sup>)



Combustion intensity upper limit is 60 MW/m<sup>3</sup> atm. Intensity is a combination more fuel related parameters like fuel mass flow, fuel lower heating value and combustion efficiency. Combustion efficiency is one of the most difficult characteristic property to be predicted at preliminary design stage. So for the initial sizing calculations it is taken as a desired value which is above 99.9 %.

Combustor volume should be selected such that it should both satisfy the combustor loading and combustion intensity limits. Furthermore it should fit the physical limits of the engine.

*Residence Time:* It is the time that is required one air molecule to pass through combustor. As the residence time increases the combustion efficiency increases. Residence time is again a volume dependent parameter and its lower limit is 3 ms. Formula for residence time is given in formula (143).

$$t_{res} = \frac{L}{v_{ref}} = \frac{\rho_{31} \cdot A_{ref} \cdot L}{\dot{m}_{31}} \quad (143)$$

$t_{res}$ : residence time (s)

$L$ : length of the main burner (m)

$\rho_{31}$ : combustor inlet density (kg/s)

$A_{ref}$ : characteristic cross sectional area of the combustor (m<sup>2</sup>)

$\dot{m}_{31}$ : mass flow entering to the combustor (kg/s)

*Outlet Temperature Distributions:* Exit temperature is one of the important performance parameters of the combustor. Although it is easy to calculate average exit temperature in preliminary design stage, it is not possible to get the pointwise maximum and radial maximum temperature values at the exit plane before doing a comprehensive CFD analysis or a performance test. Two important exit temperature related parameters are overall temperature distribution factor (OTDF) and radial temperature distribution factor. They are given in equations (144) and (145).

$$OTDF = \frac{T_{4\max} - T_{4\text{mean}}}{T_{4\text{mean}} - T_{31}} \quad (144)$$

$$RTDF = \frac{T_{4\max C} - T_{4\text{mean}}}{T_{4\text{mean}} - T_{31}} \quad (145)$$

In OTDF,  $T_{4\max}$  is the maximum temperature encountered in the exit plane. However, in RTDF formula  $T_{4\max C}$  represents the maximum circumferential mean value of temperature at the exit plane. In short, to calculate RTDF a mean radial temperature profile should be calculated. RTDF is a basic performance parameter for turbine design.

After deciding the volume of the combustor flow details should be decided. An important figure of general flow distribution inside a gas turbine combustor is the Mach number distribution inside combustion chamber. And generally accepted numbers are shown in Figure 5.1 [2]. According to the figure the annulus flow Mach number should be around 0.1 and hole flow Mach numbers should be around 0.3 and 0.2. And finally the main liner flow should be around 0.02.

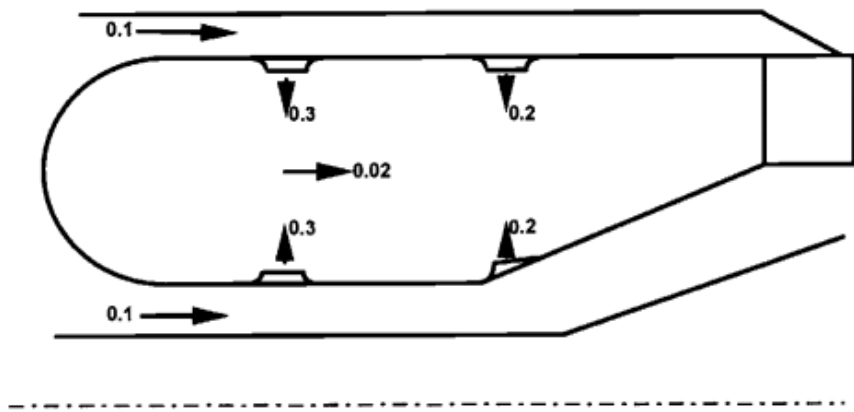


**Figure 5.1** – Mach number limits inside the combustor [2]

Another important figure helping the design of combustors is the fuel-air equivalence ratio general accepted distribution. This distribution is shown in Figure 5.2. According to the figure in primary zone where the main combustion takes place, the fuel-air equivalence ratio should be one or two percent higher than the stoichiometric

value; which is actually desirable because by this way, a complete combustion character is achieved at the primary zone. Furthermore, keeping the amount of fuel at the primary zone slightly over the stoichiometric value guarantees the combustion. If the amount of fuel in the primary zone is increased further, the combustion operational limits can be extended but this time the combustion temperature is going to be increased which causes release of unwanted  $\text{NO}_x$  emissions and overheating of the combustor walls. Another important limits shown in Figure 5.2 is the percentage of the wall cooling air, in primary and secondary zones of the combustor. It is recommended to set the cooling air around 4% for each of the wall cooling structures.

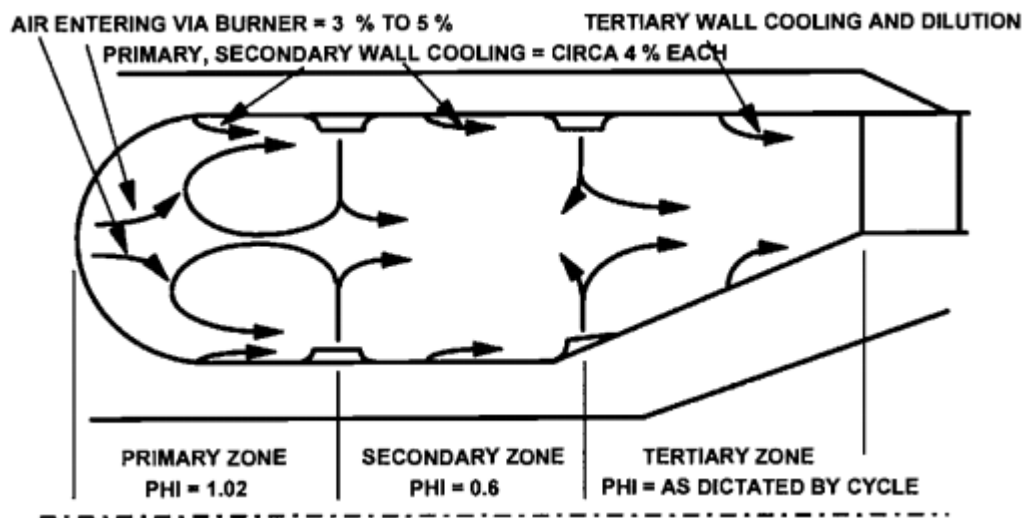


**Figure 5.2** – Fuel-air equivalence ratio limits inside the combustor [2]

In combustor design it is better to start the design by scaling an existing combustion chamber. By considering the above limits it is possible to improve an existing combustor. While making scaling in a combustion chamber, a geometric scale factor should be defined. Flow scale factor is proportional to the square of the geometric scale factor. While doing this, fuel air ratio should be kept constant. In addition, the above fundamental design parameters should be taken into consideration. In the next section by using these principles a new combustor will be designed which is based on the TEI's test combustor presented in Chapter 4.

### **5.3 Thermal Design**

In gas turbine combustor design keeping wall temperature under control is one of the major design challenges. The most common liner materials used in combustor design are Inconel, Nimonic-75, Hastelloy-X and Hayness-188. These materials are all superalloys and they have increased mechanical strength, creep resistance and resistance to corrosion. These alloys are mostly nickel and cobalt based alloys. Although their capacity to withstand high temperature and corrosive environments makes them perfect match for the gas turbine combustors, their mechanical strength deteriorate beyond 1100 K, which is a critical design limit used in the industry. Although it is possible to increase this limit by coating the exposed surfaces, this limit is widely accepted and also be used as a design restriction in this study.

In order to add a design capacity to the coupled flow and chemical reactor network modelling code a comprehensive thermal analysis is included. In this section a detailed thermal analysis is presented and this methodology is also added to the main design code to extend its capacity for predicting combustor liner thermal control.

#### **5.3.1 Heat Transfer Model**

Heat transfer to the combustor liner is composed of the thermal flows from the combustion core region to the colder annulus flow region and to the casing of the engine. Thermal flow through the combustion liner wall is presented in Figure 5.3 [1]. Heat generated as a result of the combustion inside the liner is transmitted to the liner walls by convection and radiation. By passing through the liner via conduction it is transmitted to the engine casing from annulus region by convection and radiation.

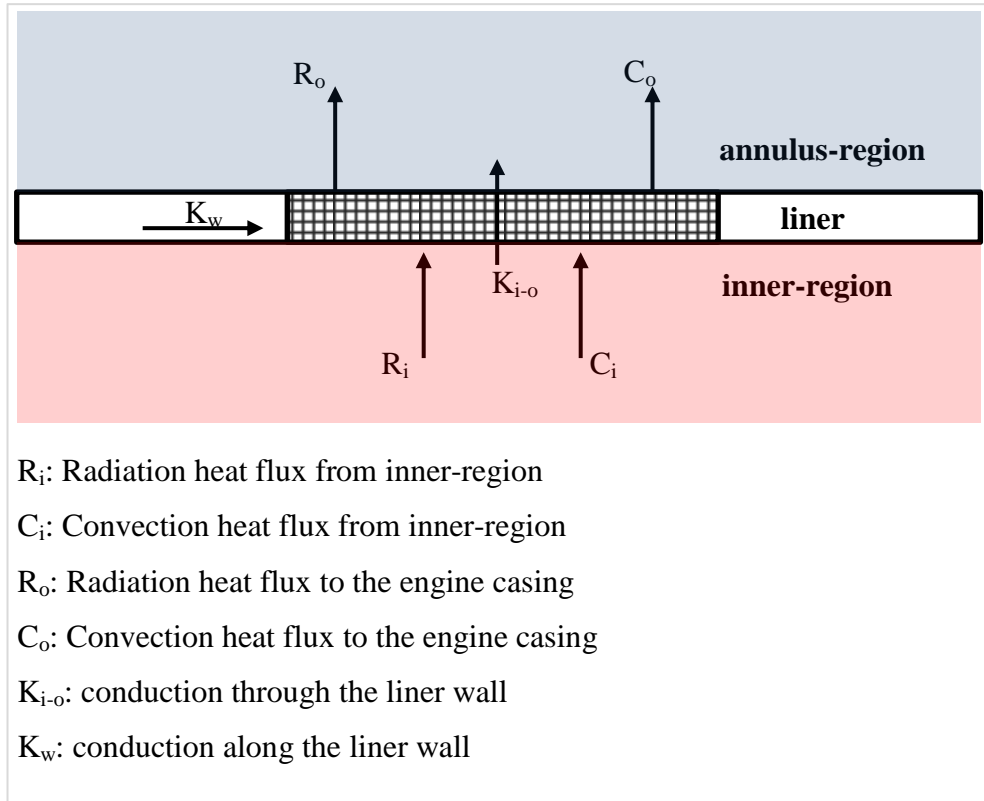


**Figure 5.3** – Thermal flow through combustion liner [1]

The model presented here gives the steady heat balance between conduction, convection and radiation terms [1]. At each axial point of calculation on the liner, the properties are assumed to be constant. By taking an element on the surface of the liner with an area of  $A_i$  on the inner surface and  $A_o$  on the outer surface, the following energy equilibrium can be written.

$$(R_i + C_i)A_i + K_w A_s = (R_o + C_o)A_o = K_{i-o}A_i \quad (146)$$

In equation (146), the conduction along the liner wall can be neglected, because the heat is transferred mostly along radial direction. Furthermore; for the liner having a small thickness, the inner and outer surface areas are nearly the same. These assumptions cancel out the second term on the left hand side of the equation and also cancel out the area throughout the equation. The equation takes the form in equation (147).

$$R_i + C_i = R_o + C_o = K_{i-o} A_i \quad (147)$$

Expanding the conduction through the liner term leads to the final form of the general equilibrium equation. Notice that in equation (148)  $k_w$  is the thermal conductivity of the wall,  $t_w$  is the thickness of the wall, and  $T_w$  terms are the inner and outer temperature of the liner walls.

$$R_i + C_i = R_o + C_o = \frac{k_w}{t_w} (T_{wi} - T_{wo}) \quad (148)$$

### 5.3.2 Internal Radiation, $R_i$

Internal radiation from the hot gases inside the liner element is calculated by starting from the primitive form of the radiation equation. It is written from the internal gases to the inner wall of the liner and shown in equation (149).

$$R_i = \sigma (\epsilon_g T_g^4 - \alpha_g T_{wi}^4) \quad (149)$$

$\sigma$  : Stefan Boltzmann constant,  $5.67 \times 10^{-8} \text{ W}/(\text{m}^2 \text{ K}^4)$

$\epsilon_g$  : gas emissivity at average gas temperature at the axial location,  $T_g$

$\alpha_g$  : absorptivity of the gas at wall temperature  $T_{wi}$

Because the internal wall surface of the liner is not black, and its absorptivity is less than 1, a practical value of  $0.5(1 + \epsilon_w)$  is introduced by Lefebvre [1] to account this effect and the equation takes the form in equation (150).

$$R_i = \sigma \cdot 0.5(1 + \epsilon_w) (\epsilon_g T_g^4 - \alpha_g T_{wi}^4) \quad (150)$$

(81)

$\varepsilon_w$  is the emissivity of the wall surface and depend on the material and its temperature. An approximate value of around 0.7-0.8 is taken for  $\varepsilon_w$  in steel based alloys. Equation (151) shows the relation between emissivity and absorptivity of gases in their own state temperatures.

$$\frac{\alpha_g}{\varepsilon_g} = \left( \frac{T_g}{T_{wi}} \right)^{1.5} \quad (151)$$

Introducing this equation into the main equation, the final form of the internal radiation equation for the combustor liner to the liner inner wall can be found.

$$R_i = \sigma \cdot 0.5(1 + \varepsilon_w) \varepsilon_g T_g^{1.5} (T_g^{2.5} - T_{wi}^{2.5}) \quad (152)$$

Gas temperature in this equation is obtained from the chemical reactor network solution of the domain. Internal wall temperature is one of the main parameters searched in thermal analysis. Gas emissivity can be found as a function of pressure, temperature and gas temperature at the region of interest via the formula introduced in Lefebvre [1].

$$\varepsilon_g = 2 - \exp(-290P(far \cdot l_b)^{0.5} T_g^{-1.5}) \quad (153)$$

P: gas pressure (kPa)

$T_g$  : gas temperature (K)

$l_b$  : beam length (m)

far: fuel air ratio

Beam length,  $l_b$ , is dependent on the geometry and it is approximately calculated as in equation (154).

$$l_b = 3.4 \times \text{volume} / \text{surface area} \quad (154)$$

### 5.3.3 Internal Convection, $C_i$

Convection inside the combustor liner is the most complex process and it is not possible to predict the convective heat transfer going to the liner walls by calculations. Only comprehensive 3D analysis can give closer results. However as an approximation it is possible to predict the heat transfer to the inner walls of liner by assuming heat transfer to the classical pipe flow. With the condition of extreme turbulence, the following expression is suitable for taking convection into account inside the liner.

$$C_i = 0.020 \frac{k_g}{d_{hl}^{0.2}} \left( \frac{\dot{m}_g}{A_L \mu_g} \right)^{0.8} (T_g - T_{wi}) \quad (155)$$

$\dot{m}_g$  : mass flow going through (kg/s)

$d_{hl}$  : hydraulic diameter of the region (m)

$A_L$  : cross sectional area based on hydraulic diameter (m<sup>2</sup>)

$\mu_g$  : dynamic viscosity (kg/m s)

The complex flow inside the combustor is due to the swirl flow inside the primary zone and the character of flow is difficult to formulate. Near wall regions are cooler than the core of the combustion region, due to this fact a correction is applied to the equation (155) for the primary zone and for any point located in the primary zone the convection equation takes the following form [1].

$$C_i = 0.017 \frac{k_g}{d_{hl}^{0.2}} \left( \frac{\dot{m}_g}{A_L \mu_g} \right)^{0.8} (T_g - T_{wi}) \quad (156)$$

### 5.3.4 External Radiation, $R_o$



In annulus region radiative heat transfer takes place between the outer walls of the liner and the casing. In this analysis the casing is assumed to have a constant temperature of  $T_{31}$  which is the inlet temperature of the combustor. Although it is possible to define a complex radiative heat transfers formula including the surface emissivity data of each surface. It is possible to write a straightforward empiric relation which is well tested for most of the practical cases [1].

$$R_o = 0.4\sigma(T_{wo}^4 - T_{31}^4) \quad (157)$$

The above relation holds for aluminum casing. Casings are mostly made up of steel and modified version of the formulae according to the steel casing is given in equation (158).

$$R_o = 0.6\sigma(T_{wo}^4 - T_{31}^4) \quad (158)$$

### 5.3.5 External Convection, $C_o$

For convective heat transfer calculation from the liner outer surface to the casing again a traditional pipe flow convection formula is utilized. The formula is given in equation (159).

$$C_o = 0.020 \frac{k_g}{d_{ann}^{0.2}} \left( \frac{\dot{m}_{ann}}{A_{nn} \mu_{ann}} \right)^{0.8} (T_{wo} - T_{31}) \quad (159)$$

$\dot{m}_{ann}$  : mass flow through annulus (kg/s)

$d_{ann}$  : hydraulic diameter of the region (m), The hydraulic diameter for an annular combustor is given two times the local annulus height of the region.

$A_{ann}$  : cross sectional area based on hydraulic diameter ( $m^2$ )

$\mu_{ann}$  : dynamic viscosity (kg/m s)

### 5.3.6 Calculation Procedure

For the calculation of the wall temperature of the liner at the selected axial location, the equation mentioned above should be solved together. The equations are summarized in equations (160)-(164).

$$R_i = \sigma \cdot 0.5(1 + \varepsilon_w) \varepsilon_g T_g^{1.5} (T_g^{2.5} - T_{wi}^{2.5}) \quad (160)$$

$$C_i = 0.017 \frac{k_g}{d_{hl}^{0.2}} \left( \frac{\dot{m}_g}{A_L \mu_g} \right)^{0.8} (T_g - T_{wi}) \text{ for primary zone} \quad (161)$$

$$C_i = 0.020 \frac{k_g}{d_{hl}^{0.2}} \left( \frac{\dot{m}_g}{A_L \mu_g} \right)^{0.8} (T_g - T_{wi}) \text{ for other zones}$$

$$R_o = 0.6\sigma(T_{wo}^4 - T_{31}^4) \quad (162)$$

$$C_o = 0.020 \frac{k_g}{d_{ann}^{0.2}} \left( \frac{\dot{m}_{ann}}{A_{nn} \mu_{ann}} \right)^{0.8} (T_{wo} - T_{31}) \quad (163)$$

$$K_{i-o} = \frac{k_w}{t_w} (T_{wi} - T_{wo}) \quad (164)$$

As can be seen the equations are all functions of the liner inner surface temperature,  $T_{wi}$ , and liner outer surface temperature  $T_{wo}$ . If the constant terms are grouped and renamed, a final form of the equations can be obtained to find a solution. The equation group to be solved is given in equations (165)-(169).

$$R_i = a1 - b1 \cdot T_{wi}^{2.5} \quad (165)$$

$$C_i = a2 - b2 \cdot T_{wi} \quad (166)$$

$$R_o = a3 \cdot T_{wo}^4 - b3 \quad (167)$$

$$C_o = a4 \cdot T_{wo} - b4 \quad (168)$$

$$K_{i-o} = a5(T_{wi} - T_{wo}) \quad (169)$$

These equations can be put into equation (148) which binds all these together. Equation (148) leads to two final equations; one for the heat transfer from the inner surface of the liner and the other one is for the outer surface of the liner. These equations are given in equations (170) and (171).

$$R_i + C_i = \frac{k_w}{t_w} (T_{wi} - T_{wo}) \quad (170)$$

$$R_o + C_o = \frac{k_w}{t_w} (T_{wi} - T_{wo}) \quad (171)$$

Inserting the final form of the equations given in equations (165)-(169) into equations (170) and (171) the following equations are obtained.

$$a5 \cdot T_{wo} - b1 \cdot T_{wi}^{2.5} - b2 \cdot T_{wi} - a5 \cdot T_{wi} + a1 + a2 \quad (172)$$

$$a3 \cdot T_{wo}^4 + a4 \cdot T_{wo} + a5 \cdot T_{wo} - a5 \cdot T_{wi} - b3 - b4 \quad (173)$$

Equations (172) and (173) are non-linear equations and they can be solved iteratively by assuming an initial guesses for inner and outer surface of the liners. In this study a script has been prepared and added to the main design code for the calculation of the liner temperature.

#### 5.4 Wall Cooling Design and Implementation

Design of combustor liners, as it is mentioned previously, includes many challenges. Making a design that is having a stable flame character and a controlled exit temperature profile is not enough. The temperature levels on the liner metal should be checked and a cooling strategy should be applied if necessary. In order to cool the walls of the combustor liner two methods are widely used. The first method is the film cooling technique and the other one is the effusion cooling technique. Film cooling technique is mostly applied at the preliminary design stage and is a reliable solution for controlling the high spots regions on the liner. Effusion cooling however,

is usually an after design solution to cool hot spot regions which cannot be predicted at the preliminary design stage, or for the regions where film cooling is not possible. Although there exists some designs that are cooled fully by effusion cooling their design scope are out of the content of this study. So film cooling technique will be described in the rest of this section.

#### 5.4.1 Film Cooling Methods

Film cooling methods are used for cooling of a specific axial region of the inner surface of the liner. Film cooling holes at a specific axial location covers the entire inner surface circumferentially at that axial location. Due to physical restrictions and manufacturing difficulties it is not possible to apply film cooling at anywhere on the liner. A typical film cooling slot is shown in Figure 5.4. In the figure, the film cooling slot is placed after a major hole group and the liner region between the two hole groups are cooled by the film cooling slot. The flow jet passing through the small film cooling hole flows along the inner side of the combustor liner near the wall and creates a protecting cooled layer near the wall region.

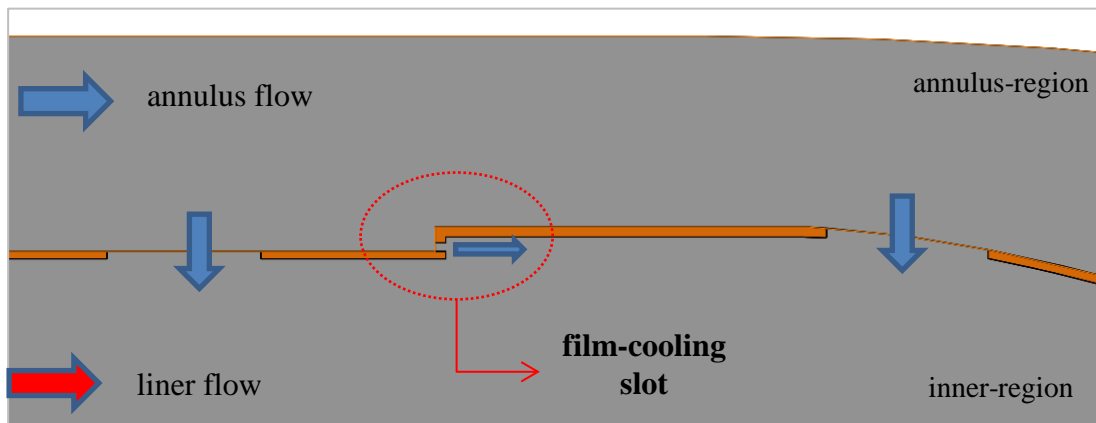


**Figure 5.4** – Simple film cooling slot representation.

Different film cooling hole configurations are available and they are developed to overcome difficulties in production stability and uniformity. The well-known film cooling configurations are outlined in Lefebvre [1] and shown in Figure 5.5.

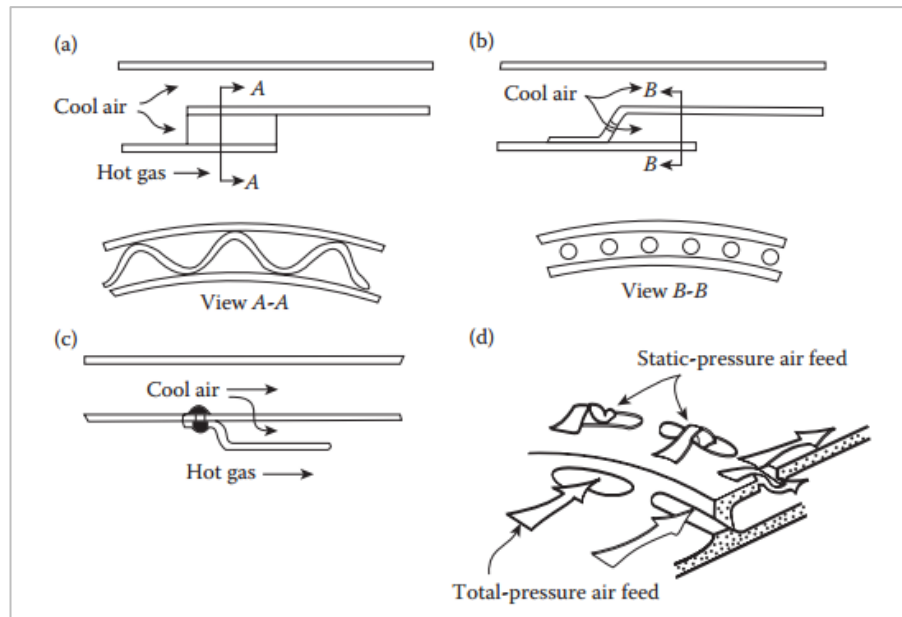


**Figure 5.5** – Film cooling configurations: a. wigglestrip b. stacked ring c. splash-cooling ring d. machined ring [1]

When the film cooling configurations are examined from the figure, it can be noted that the structure of the configurations are getting complicated from a. to d. The mostly used configurations are the stacked ring and splash ring configurations. The air passage holes on the stacked rings are drilled or punched and their accuracy is uniform compared with the wigglestrip configuration. Splash cooling ring uses only the static pressure difference between the two regions. To increase structural integrity of the cooling slots and prevent cracking more advanced designs are introduced by the major engine producers and these methods also guarantee the lip of the cooling slots are also cooled. These improved versions are shown in Figure 5.6.

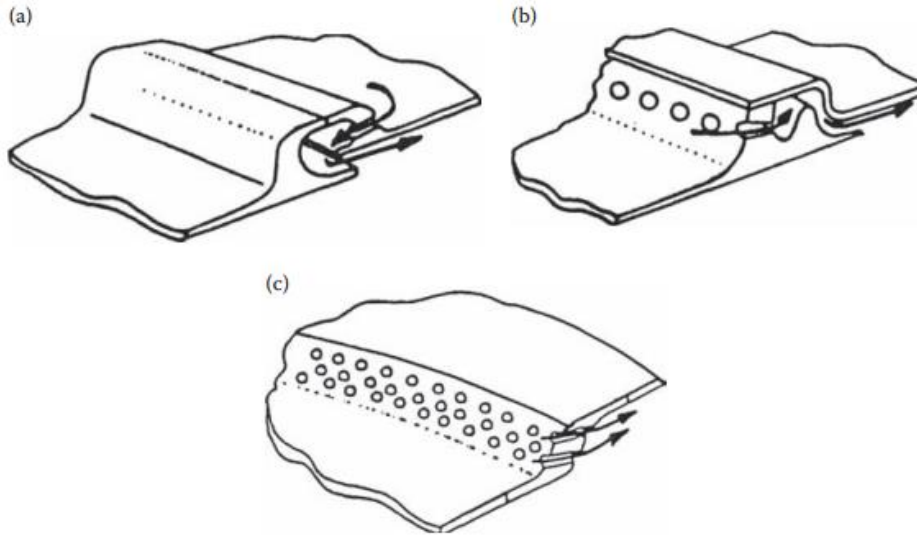


**Figure 5.6** – Improved film cooling configurations [1]

In the context of this study a simple stacked ring type configuration of film cooling will be utilized to show design implementation and the performance verification. More complex designs are to prevent real time manufacture and operational failures which are not the case in here.

#### 5.4.2 Implementation of Film Cooling to the Heat Transfer Model

Film cooling air is injected into the liner inner surface and it flows parallel to the liner inner wall. The flow of film cooling can be modeled by using a turbulent boundary-layer model or a wall-jet model. However for most of the aero engine combustor cases the film cooling jet flow is higher than the flow inside the liner region at that location. So it is more convenient to use wall-jet model rather than the boundary-layer based model.

The modelling of film cooling flow begins with the definition of the film-cooling effectiveness,  $\eta$ . It is given in the equation (174). In this equation  $T_g$  is the temperature of the gas inside liner at the region of interest,  $T_a$  is the temperature of the air coming from the slot which is actually  $T_{31}$  and  $T_{w-a}$  is the temperature of the gas near the film-cooled wall region at a predefined axial location.

$$\eta = \frac{T_g - T_{w-a}}{T_g - T_a} \quad (174)$$

Another important parameter used in the design is  $m_r$  which is the ratio of mass flux of the film cooling slot to the main gas flow slot.

$$m_r = \frac{\rho_a \cdot V_a}{\rho_g \cdot V_g} \quad (175)$$

$m_r$  is used to as a measure of correction and two different empirical film cooling effectiveness formula are introduced by Ballal and Lefebvre [1] these are given in equations (176) and (177).

for  $0.5 < m_r < 1.3$

$$\eta = 1.10 \cdot m_r^{0.65} \left( \frac{\mu_a}{\mu_g} \right)^{0.15} \left( \frac{x}{s} \right)^{-0.2} \left( \frac{t}{s} \right)^{-0.2} \quad (176)$$

for  $1.3 < m_r < 4.0$

$$\eta = 1.28 \cdot m_r^{0.65} \left( \frac{\mu_a}{\mu_g} \right)^{0.15} \left( \frac{x}{s} \right)^{-0.2} \left( \frac{t}{s} \right)^{-0.2} \quad (177)$$

In the equations (176) and (177),  $x$  is the point downstream of the film cooling hole where the temperature of the wall surface will be calculated. Notice that the temperature of the wall downstream of the film cooling hole decreases as the distance  $x$  increases. Moreover,  $t$  is the lip thickness of the film cooling hole, and finally  $s$  is the depth of the film cooling slot. For the empirical correlations also the values of dynamic viscosities are calculated for the film cooling flow and the liner inner side gas flow.

As for the implementation of the film cooling formulas to the general heat transfer model described in section 5.2, following modifications are needed to be made. In

the calculation of inner and outer wall temperature of the liner. The inner region radiation term  $R_i$ , annulus region radiation term  $R_o$  and annulus region convection term  $C_o$  is remained untouched. However, the inner region convection equation is needed to be modified.

For different values of the mass flow ratio,  $m_r$ , different convective terms are suggested [1].

for  $0.5 < m_r < 1.3$ ,

$$Nu = 0.069 \cdot \left( Re_s \cdot \frac{x}{s} \right)^{0.7} \quad (178)$$

$$Re_x = V_a \cdot \rho_a \cdot \frac{x}{\mu_a} \quad (179)$$

$$C_i = 0.069 \cdot \frac{k_a}{x} \cdot Re_x^{0.7} (T_{w-a} - T_{wi}) \quad (180)$$

for  $m_r > 1.3$ ,

$$Nu = 0.10 \cdot Re_s^{0.8} \cdot \left( \frac{x}{s} \right)^{0.44} \quad (181)$$

$$C_i = 0.10 \cdot \frac{k_a}{x} \cdot Re_x^{0.8} \cdot \left( \frac{x}{s} \right)^{-0.36} (T_{w-a} - T_{wi}) \quad (182)$$

Convection term can be calculated by the following steps:

- calculate the mass fluxes from the film cooling holes and inner liner region
- calculate the Reynolds number of the film cooling hole
- calculate ratio of the mass fluxes,  $m_r$
- by using suitable film cooling effectiveness formula, according to the value of  $m_r$ , the near wall region gas temperature  $T_{w-a}$  is calculated
- knowing value of  $T_{w-a}$ , it is possible to find the  $C_i$  by selecting the suitable  $C_i$  formula from equations (180) and (182).



## 5.5 Design Code Solution Methodology

As it is discussed at the beginning of this chapter, for designing a combustor basic combustor design parameters should be calculated. The limiting boundaries of this design are the geometric restrictions coming from the gas turbine design. These geometric restrictions define the outer geometry of annulus, combustor length, inlet structure of the combustor and exit structure of the combustor. By knowing these geometric limits the combustor design parameters can be calculated. This also gives the basic liner sizing. Afterwards an initial liner hole configuration is decided. The initial hole configuration can be based on the existing design. From that point, the core of the design code is used to calculate the flow, pressure, temperature distribution inside the chamber. Afterwards a liner wall thermal analysis is made to calculate the wall metal temperature of the current design. According to the high temperature limits of liner material, a suitable liner film cooling configuration is applied to the design. By using this final state of the combustor, an inner iteration is made to find the film cooling mass flow rates and to predict the new design's performance characteristics. These iteration inner iterations continue until the flow distributions and performance characteristics reach to design limits. This design procedure is shown schematically in Figure 5.7.

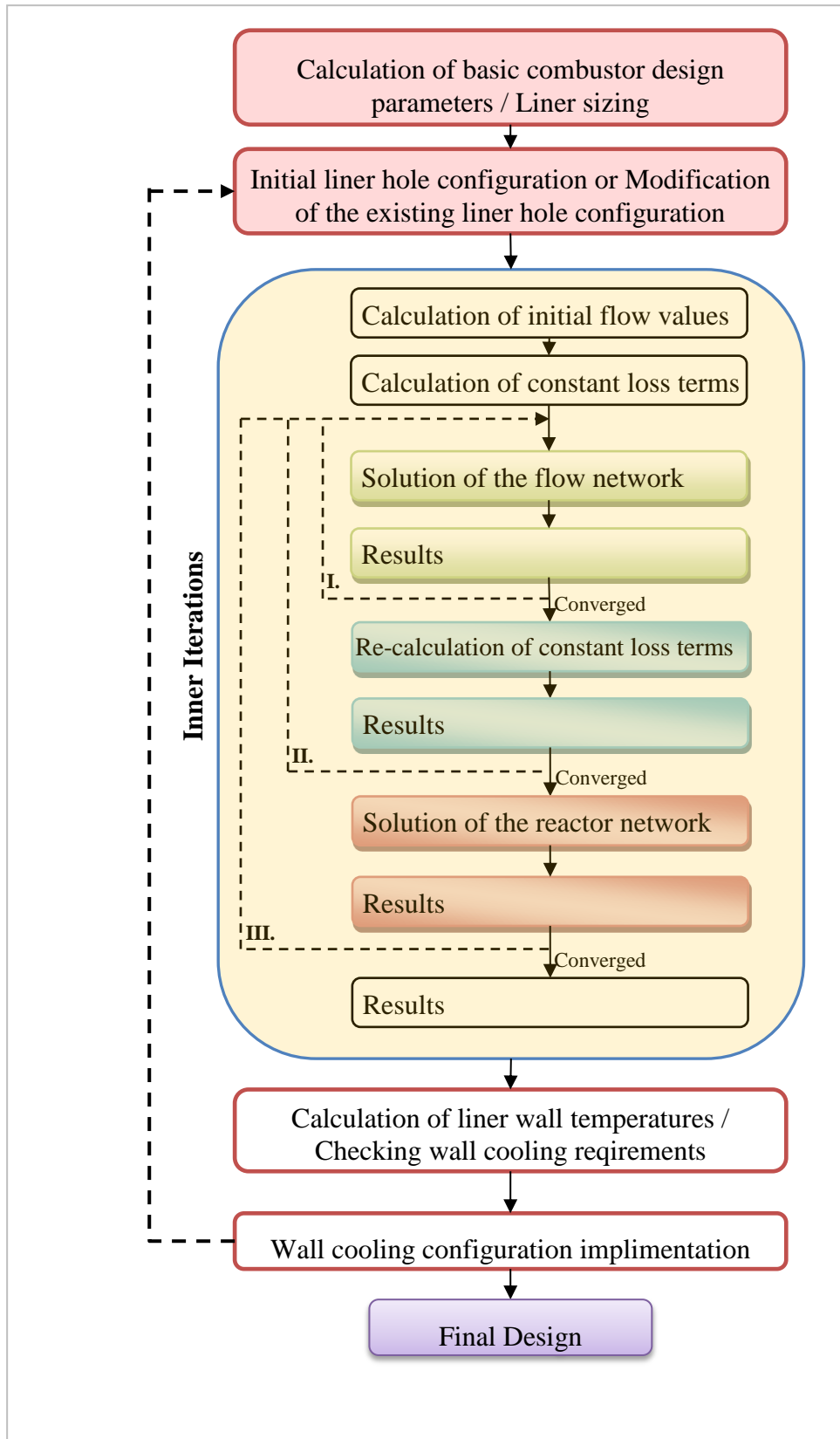


**Figure 5.7 - Solution procedure for the 1D design code**

## **5.6 Case Study: A New Test Combustor**

In Chapters 3 and 4, the test combustor of TEI is introduced and this combustor is solved by the developed network model. As a new design case, this test combustor is taken as a basis and will be improved in terms of the basic combustor design parameters and thermal considerations. The test combustor is an annular type of combustor and it is developed to be used for short mission objectives. Hence, it doesn't have a long operational hour targets. As a result the combustor doesn't include a cooling configuration on it, as an improvement the combustor liner will be added a liner cooling configuration. Furthermore, the basic characteristics of the combustor are slightly exceeding the predefined margins which are going to be redesigned in this section.

### **5.6.1 Existing Combustor Configuration**

In order to make a new combustor based on the existing test combustor design, the current design parameters should be determined. By the help of the parameters defined at the beginning of this chapter, a design analysis of the existing configuration of the test combustor will be presented here.

**Table 5.1**– Basic combustor design parameters for the existing design

<b>Combustor Loading (CL)</b>		13.1
$\dot{m}_{31}$	0.183	mass flow: kg/s
$P_{31}$	3.96	inlet pressure: atm
$T_{31}$	478.1	inlet temperature: K
V	0.000902888	volume of liner: m <sup>3</sup>

<b>Combustion Intensity (I)</b>		44.6
$\dot{m}_f$	0.00374	fuel mass flow: kg/s
LHV	43.1	fuel calarofic value (MJ/kg)
$P_{31}$	3.96	inlet pressure: atm
V	0.000902888	volume of liner: m <sup>3</sup>
$\eta_c$	0.99	efficiency

<b>Residence Time (ms)</b>		1.5
V	0.0009	volume of liner: m <sup>3</sup>
$P_{31}$	3.96	inlet pressure: atm
$T_{31}$	478.1	inlet temperature: K
R	287.1	gas constant J/ kg.K
$\dot{m}_{31}$	0.183	mass flow: kg/s
$\rho_{o3}$	2.89	density at the inlet
L	0.107	length of the main burner: m

It can be seen from Table 5.1 that the three major design parameters are selected such that they exceed the suggested limits. This kind of design deviations are usually occurs due to changing parameters of the engine cycle after design has been made. In the existing design, combustor loading parameter is around 13.1 kg/(s atm<sup>1.8</sup>m<sup>3</sup>) which is above the design limit 10 kg/s atm<sup>1.8</sup>m<sup>3</sup>, which means the current combustion volume generates more energy than it should be generated this may cause complications under real operations such as unstable flow and combustion transients due to changing flight conditions. In terms of combustion intensity the existing design is in the limits so it is acceptable for this criterion. Third major parameter is the residence time. Although residence time is a difficult parameter to predict in the preliminary design stage it is defined and according to the definition it

should be longer than 3ms which is 1.5 for the existing case. Shorter residence time means less time for completion of the combustion inside the chamber. This situation directly affects the combustion efficiency of the combustion chamber, which means increase in the fuel consumption of the engine.

### **5.6.2 New Combustor**

A new combustor design has been made to obey the limits of the basic design parameters. The new combustor design is based on the existed combustor design of TEI's test combustor. The major design change is made by changing the combustor volume afterwards a thermal analysis has been made to define the possibilities of implementation of wall cooling configuration. And finally a preliminary design is performed iteratively to determine the final liner hole diameter configuration.

In terms of basic design parameters the combustor volume is doubled, so that the energy released per unit volume of combustor is decreased. This means decrease of the combustor loading. In combustor scaling methodology described in Walsh et al [2], the air flow should be scaled proportional to the geometric scale factor. In the new configuration the air flow is scaled according to the geometric scale factor. In addition to that, a further increase has been made to compensate the cooling air requirements of the combustor. Basic combustor design parameters for the new combustor are summarized on Table 5.2.

**Iteration -1: Scale up / No film cooling configuration**

The scaled-up version of the new combustor is going to be named as iteration-1.

**Table 5.2**– Basic combustor design parameters for the new combustor

<b>Combustor Loading (CL)</b>		11.1
$\dot{m}_{31}$	0.31	mass flow: kg/s
$P_{31}$	3.96	inlet pressure: atm
$T_{31}$	478.1	inlet temperature: K
V	0.0018	volume of liner: m <sup>3</sup>

<b>Combustion Intensity (I)</b>		37.6
$\dot{m}_f$	0.0063	fuel mass flow: kg/s
LHV	43.1	fuel calarofic value (MJ/kg)
$P_{31}$	3.96	inlet pressure: atm
V	0.0018	volume of liner: m <sup>3</sup>
$\eta_c$	0.99	efficiency

<b>Residence Time (ms)</b>		2.3
V	0.0018	volume of liner: m <sup>3</sup>
$P_{31}$	3.96	inlet pressure: atm
$T_{31}$	478.1	inlet temperature: K
R	287.1	gas constant J/ kg.K
$\dot{m}_{31}$	0.31	mass flow: kg/s
$\rho_{o3}$	2.89	density at the inlet
L	0.134	length of the main burner: m

It can be seen from Table 5.2 that increasing the combustor volume decreases the combustor loading to 11.1 kg/s atm<sup>1.8</sup>m<sup>3</sup>. Combustion intensity is also dropped further from 44.6 to 37.6. Although design limit for the intensity is 60, the lower values are desired for the intensity; hence in this parameter the design is also improved. Finally the residence time is increased to the 2.3 ms which is the minimum design limit. Actually longer residence times are desired but increasing the design from 1.5 to 2.3 ms is a major improvement. Although it is aimed to drop combustor loading more, a balance is made between the volume and the airflow coming to the combustor.

After increasing of the volume without doing any other changes, the current flow split data should be checked. On Table 5.3 mass flow distribution can be seen. Nearly the same mass flow percentages are found as a result of the scaling operation, which is expected because no other changes are made on the combustor configuration yet.

**Table 5.3**– Current mass flow distribution between the holes of the new design, iteration-1

	MASS FLOW	
	kg/s	%
<b>Swirler</b>	0.072661292	23.4
<b>Primary</b>	0.035105874	11.3
<b>Secondary</b>	0.057621481	18.6
<b>Dilution-1</b>	0.133663835	43.1
<b>Dilution-2</b>	0.010947519	3.5

In order to further develop the combustor design the wall temperature calculation script is used and the wall temperature for different zones of the combustor are calculated by 1D design tool. The zones of the combustor are shown in Figure 5.8. Furthermore by using the coupled flow-chemical reactor network solver the expected temperatures inside the combustor zones are given on Table 5.4.

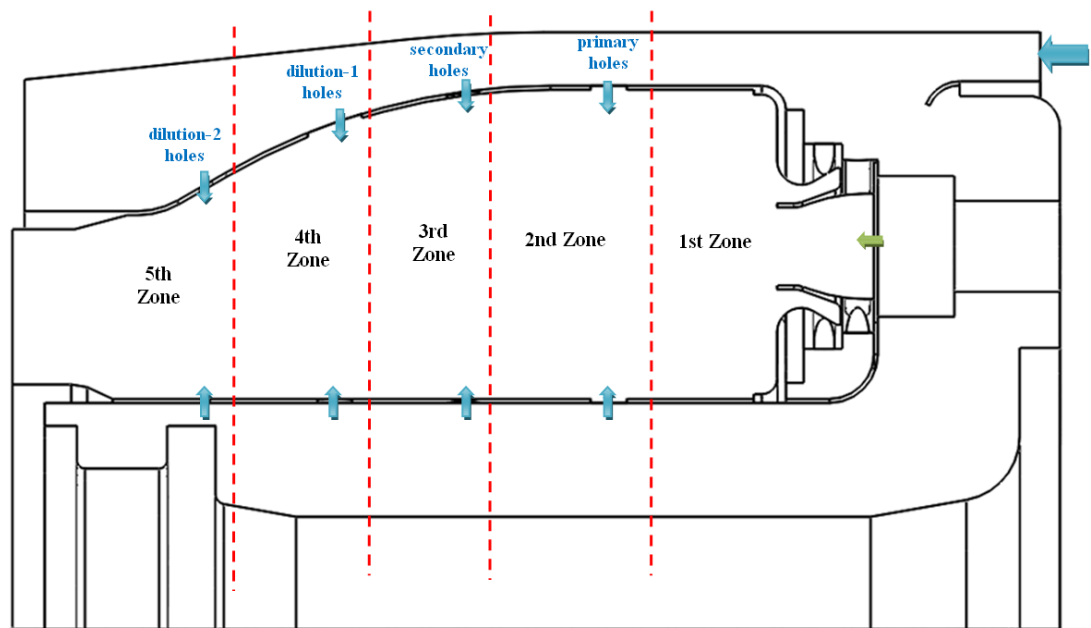


**Figure 5.8** – Combustor zones, iteration-1

**Table 5.4**– Gas temperature of the new design, iteration-1

ZONES	Gas Temperature (K)
1st Zone	2108.7
2nd Zone	2021.7
3rd Zone	1705.9
4th Zone	1251.1
5th zone	1232.5

As knowing of the zonal temperature inside the combustor liner, it is possible to predict the liner metal temperature inside the combustor. By using the thermal model described at the beginning of this chapter the inner and outer surface temperature of the liner for each zone is calculated. The temperature values are presented on Table 5.5.



**Table 5.5**– Liner wall temperature of the new design, iteration-1

ZONES	T inner wall (K)	T outer wall (K)
1 <sup>st</sup> Zone	<b>1390.6</b>	<b>1384.5</b>
2 <sup>nd</sup> Zone	<b>1320.1</b>	<b>1315.9</b>
3 <sup>rd</sup> Zone	1068.1	1065.3
4 <sup>th</sup> Zone	733.7	732.7
5 <sup>th</sup> zone	678.5	677.8

When Table 5.5 is examined it can be seen that the temperature gets high values at the liner wall walls of the 1<sup>st</sup> and the 2<sup>nd</sup> zones. These regions are the main regions that combustion process takes place, after 2<sup>nd</sup> zone the hot gases mix with the incoming air streams and cool down to the suitable temperature for the turbine blades. As the design material limit of 1100 K, is exceeded in these two zones film cooling configuration can be added to these regions. In the next iteration a 2 film cooling layers will be implemented on the surfaces 1<sup>st</sup> Zone and 2<sup>nd</sup> Zone of the liner which are found critical by the preliminary analysis.

### ***Iteration -2: Film Cooling Configuration***

After the preliminary sizing analysis, it is apparent that a wall cooling application is required for the 1<sup>st</sup> and 2<sup>nd</sup> Zones. Film cooling configuration is going to be decided by the following steps:

- an initial cooling hole diameter is going to be selected
- a new network model is going to be prepared
- by using the coupled flow and network the mass flow percentage from the liner holes are going to be found
- if the amount of cooling air is around 4% of the total flow for each of the flow zones, iterations are stopped

The network model of the new combustor is given in Figure 5.9.

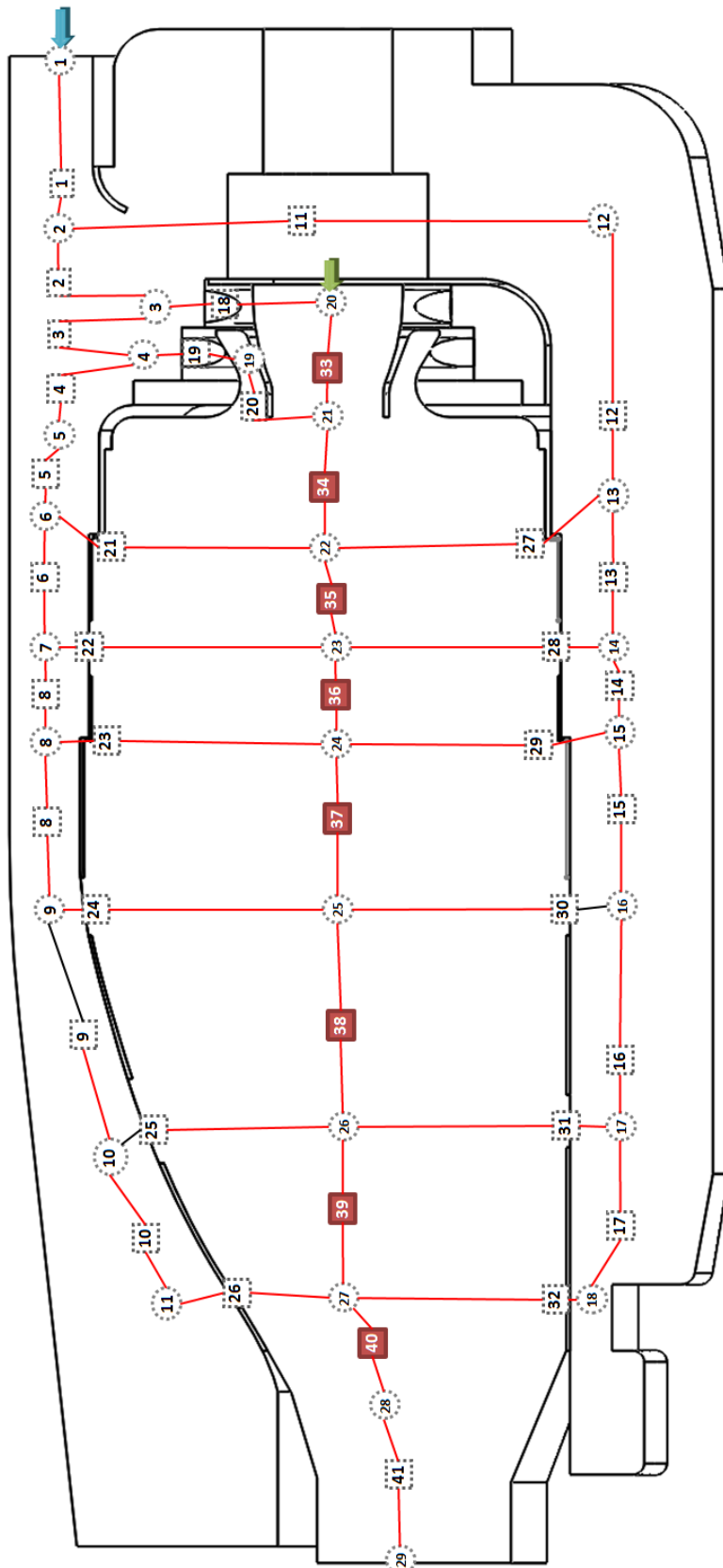


**Figure 5.9** – Network model of the new combustor

In order to make a good initial guess a comparison between the holes group should be made. Total hole area is a good measure of comparison because the hole numbers are different for different hole groups. The total hole areas are given on Table 5.6 for the current hole iteration. As an initial guess a total area of  $0.000319 \text{ m}^2$  is selected for both of the film cooling holes. By solving the flow-reactor network code flow split results are obtained. Hole mass flow percentage for film cooling-1 slot is 5.0% and for film cooling-2 slot it is 5.8% by changing the area of the film cooling holes; at the 3<sup>rd</sup> hole iteration mass flow percentage for both of the film cooling holes are set to 4.1 %. Notice that because the cooling air percentage is relatively low when compared with the other hole groups, the diameter of the other hole groups are remained unchanged during these iterations.

**Table 5.6**– Hole area iterations to get optimum wall cooling mass flow

	Hole Iteration-1		Hole Iteration-2		Hole Iteration-3	
	Total Area (m <sup>2</sup> )	Mass Flow Percentage	Total Area (m <sup>2</sup> )	Mass Flow Percentage	Total Area (m <sup>2</sup> )	Mass Flow Percentage
<b>swirler</b>	0.001336846	24.8	0.001336846	25.4	0.001336846	25.5
<b>primary</b>	0.000706858	11.0	0.000706858	11.3	0.000706858	11.3
<b>filmC 1</b>	0.000319206	5.0	0.000254469	4.1	0.000254469	4.1
<b>secondary</b>	0.001164156	18.1	0.001164156	18.5	0.001164156	18.6
<b>filmC 2</b>	0.000319206	5.8	0.000240528	4.5	0.000221671	4.1
<b>dilution1</b>	0.002308069	33.8	0.002308069	34.7	0.002308069	34.8
<b>dilution2</b>	0.000216424	1.5	0.000216424	1.6	0.000216424	1.6

It was mentioned on Table 5.6 that after scaling up the combustor, the 1<sup>st</sup> and 2<sup>nd</sup> Zone wall temperature were exceeding material limit 1100 K. By adding a film cooling configuration, the wall temperature levels can be set to much lower values. By using the methodology described in section 5.3.1 the wall temperatures of the 1<sup>st</sup> and 2<sup>nd</sup> Zone are recalculated for the determined cooling structure. The results for the zones are presented in Figure 5.10. Because the film cooling jet going coming from the film cooling hole loose its effect after a certain distance, the wall temperature is tend to increase which is the case in Figure 5.8.

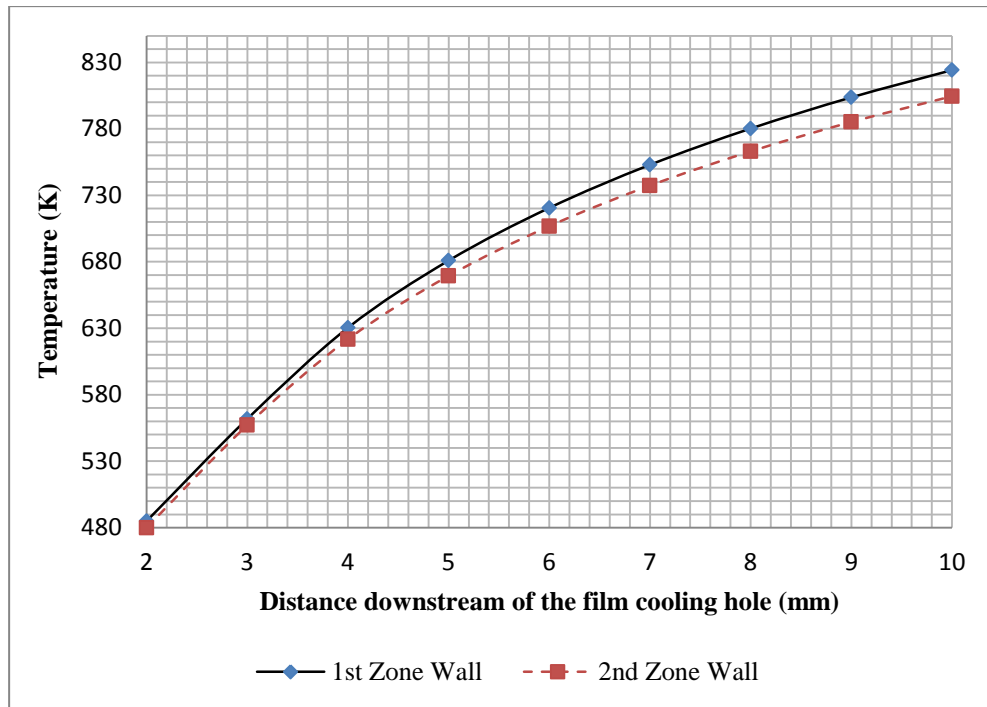


**Figure 5.10** – Average wall temperature calculated downstream of the cooling holes at 1<sup>st</sup> and 2<sup>nd</sup> Zones

After finding the required film cooling hole areas and diameters, the scaled up model is re-drawn in CAD for checking its performance in 3D detailed analysis. The new combustor design is shown in Figure 5.11.

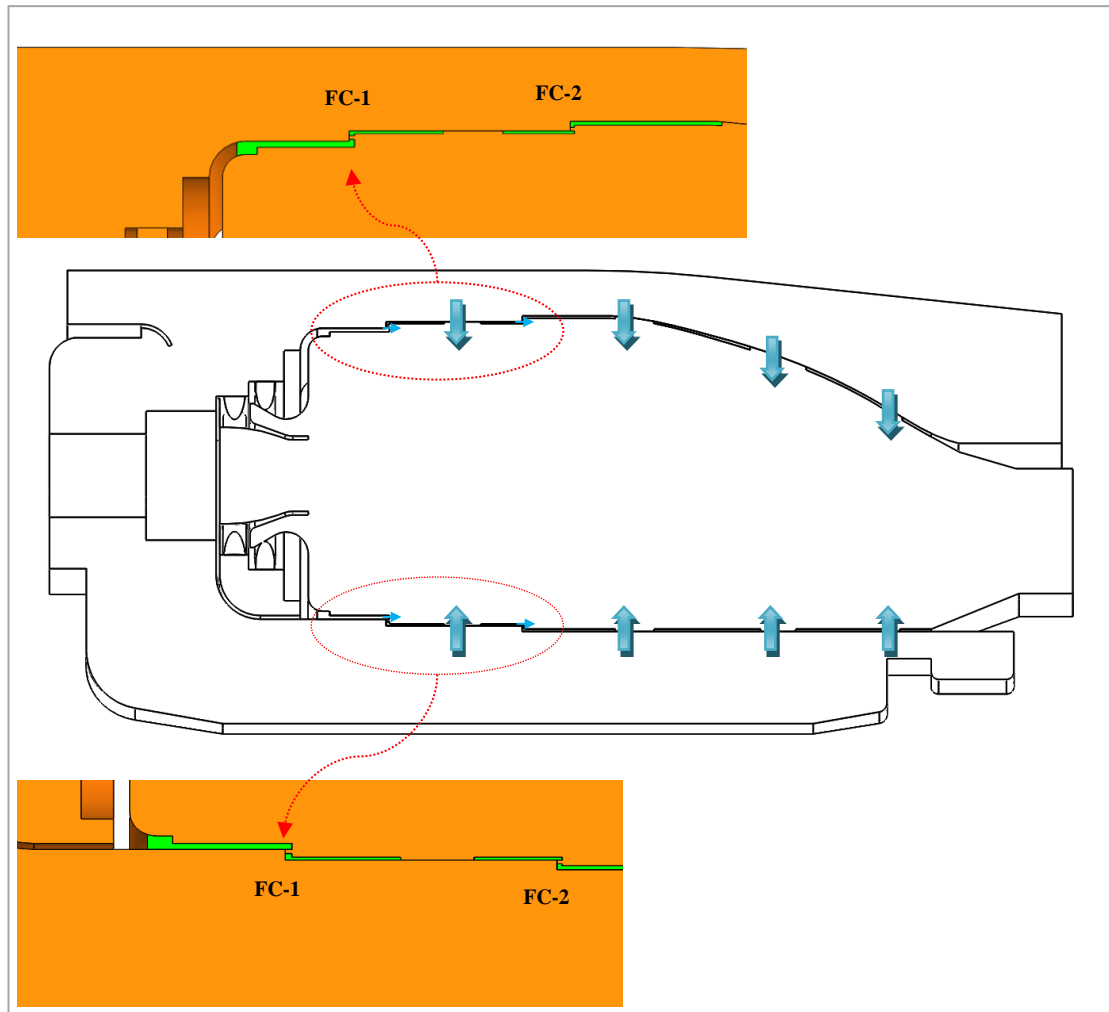


**Figure 5.11 – New combustor design with film cooling**

### 5.6.3 Detailed Performance Analysis of the New Design

The final check of the newly designed combustor is done by using CFD tools. The methodology used in the analysis is the same as described in Chapter 4. The combustion chamber is made up of 7 sectors and in the analysis only 1 sector is analyzed. 16M tetrahedral elements and 2.7M nodes are utilized, computational mesh is shown in Figure 5.12.

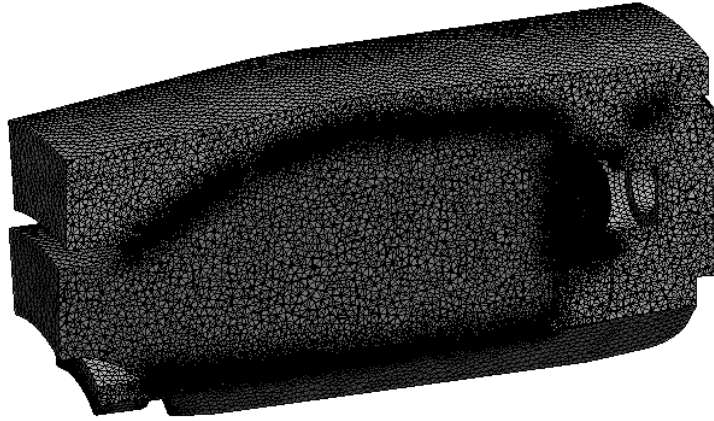


**Figure 5.12** – New combustor solution grid

The mesh is created to guarantee a  $y^+ \sim 60$  for the wall regions. A standard wall function is utilized during the analysis. Like in the previous analysis RANS model with realizable  $k-\varepsilon$  turbulence model is selected. The difference of this analysis from the previous analysis is that in this analysis the walls of the combustor are also meshed and they are taken account in the analysis. By solving the wall zone it became possible to predict the temperature of the wall, which is a comparison means for the prediction of the design code. The analysis settings are summarized on Table 5.7

**Table 5.7 – Analysis Settings**

Analysis Settings			
	Main Setting	1st Setting	2nd Setting
<b>Solver</b>	Pressure Based		
<b>Turbulence Model</b>	k- $\epsilon$ realizable	standart wall functions	
<b>Radiation</b>	on		
<b>Combustion Model</b>	Non-Premixed Combustion	Steady diffusion flamelet	
		Pre-Calculated chemistry table	
<b>Discrete Phase Model</b>	Interaction with continuous phase	Two-way turbulence coupling	
<b>Liquid Droplet Injection</b>	Injection type	Solid Cone	
		Multicomponent liquid fuel	
		Velocity magnitude: 50 m/s	
<b>Material</b>	Air-combustion species mixture	PDF Mixture	
	Liquid kerosene model	YC10H22	0.8
		YC9H12	0.2
<b>Boundary Conditions</b>	Inlet	Mass flow inlet	
	Outlet	Pressure outlet	
	Side Walls	Periodic Interface	
	Liner holes	interior surface	
<b>Solution Methods</b>	Pressure Velocity Coupling		
		SIMPLE/COUPLED	
	Spatial Discretization		Green-Gause node based
		Gradient	
		Pressure outlet	PRESTO
		Density	Second order upwind
		Momentum	Second order upwind
		Turbulent Kinetic Energy	Second order upwind
		Turbulent Dissipation Rate	Second order upwind
		Energy	Second order upwind
		Mean Mixture Fraction	Second order upwind
		Mixture Fraction Variance	Second order upwind

The inlet of the combustor is given mass flow boundary condition. The outlet is open to atmosphere as in the combustor test conditions. The fuel is injected into the domain at the exact place of the fuel injector. Fuel is injected from a 3mm opening and is forming a cone sheet with a cone angle of 30 degrees. The injected particles mix with the incoming air from the primary and secondary swirler air to form a combustible mixture. The sides of the combustor are given symmetric boundary condition. Furthermore in order to measure the amount of air passing through the liner holes internal hole boundaries are added on the model. These hole elements are

of the type interior and don't have any effect on the flow field. The boundary conditions are summarized on table 5.8 for the analysis.

**Table 5.8** – Combustion chamber CFD boundary conditions

Air mass flow rate (kg/s)	0.31
Fuel mass flow rate (kg/s)	0.0063
Combustor inlet temperature (K)	478
Combustor exit pressure	Open to atm.
Air/Fuel Ratio	49

For modeling of the combustion, non-premixed modeling approach is preferred. In non-premixed combustion fuel and oxidizer are mixed after entering the domain. A mixture fraction based approach is utilized, by this way solution of the complex mechanism during the solution of the domain is bypassed. Instead, a preliminary chemistry calculation stage is performed and it is used to generate flamelet library. For this analysis, a flamelet library is generated by using Aachen detailed chemical mechanism with a scalar dissipation range of 0.01 - 120 1/s, which is similar to the previous analysis described in Chapter 4.

After formation of the flamelets, they are imported into CFD solver and a combustion solution can be obtained. Numerical analysis is performed for the same boundary conditions with the experiments. The analysis is iterated until steady convergence is achieved. For the convergence of the flow field the residuals of the flow field parameters are monitored and solution is continued until the all of the residuals are dropped below the convergence limits. The limits of convergence for the flow parameters are given on Table 5.9. The convergence criteria shown on table 5.9 are selected in the upper limit, they may be selected lower values however in a steady combustion simulation the main convergence parameters are the time-wise tracked combustor parameters such as exit temperature and flow values (such as pressure or velocity) near the critical regions .



**Table 5.9** – Convergence Criteria for the Analysis

Residuals	Residual based on	Criteria
continuity	rate of mass creation in cells	1.00E-03
x-velocity	x-velocity parameter	1.00E-03
y-velocity	y-velocity parameter	1.00E-03
z-velocity	z-velocity parameter	1.00E-03
energy	energy parameter	1.00E-06
k	turbulence k parameter	1.00E-03
epsilon	turbulence epsilon parameter	1.00E-03
fmean	mass fraction residual of fuel	1.00E-03
fvar	variance of mass fraction of fuel	1.00E-03

The results of the CFD analysis' results for the new combustor design are presented in this section. The basic performance parameters are presented here as the output of the simulations. These are the flow, temperature, total pressure and species distributions. These data are also available as an experimental output in the next section, and for this reason the values obtained from the CFD can be used as a comparison tool for the results of the 1D code.

### 5.6.3.1 Velocity Results

Performance characteristics of the chamber can be understood by inspection of the velocity figures. It can be seen in Figure 5.13 that the velocity distribution is dominated by the primary hole flow. The jet is flowing through the primary hole with an average velocity of 55 m/s and forms a barrier in front of the centerline flow in which hot gases are recirculating. The low velocity region at the primary zone is the recirculation region which can also be seen in Figure 5.14. The vector distribution also shows the weak recirculation region that is occurring at the end of the outer annulus region. The incoming air flow from different hole groups combines with the hot gases and leaves the combustor with a high speed. Figure 5.13 also includes the detail showing the air flow coming through the cooling holes. Especially the 2<sup>nd</sup> cooling hole shows its effectiveness. The upstream of the cooling hole exit, near the

liner wall has low velocity and downstream of the cooling region has a significantly higher velocity. The high velocity maintains high cooling capacity which is going to be mentioned in thermal results.

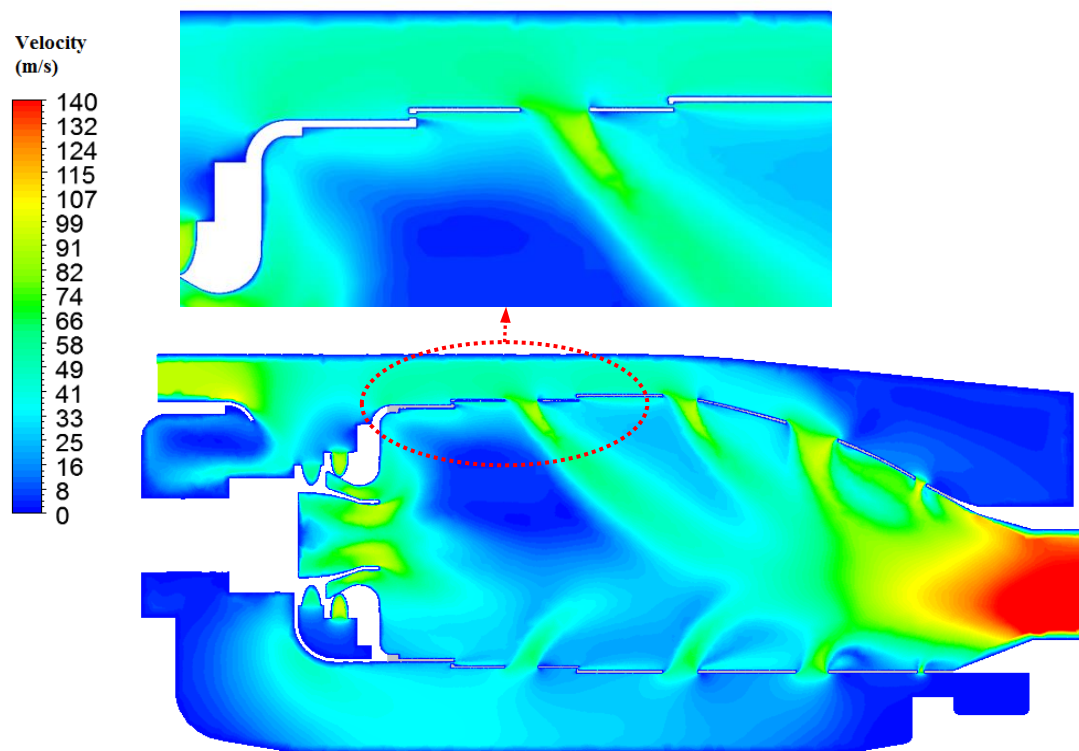


**Figure 5.13** – Velocity distribution along centerline section

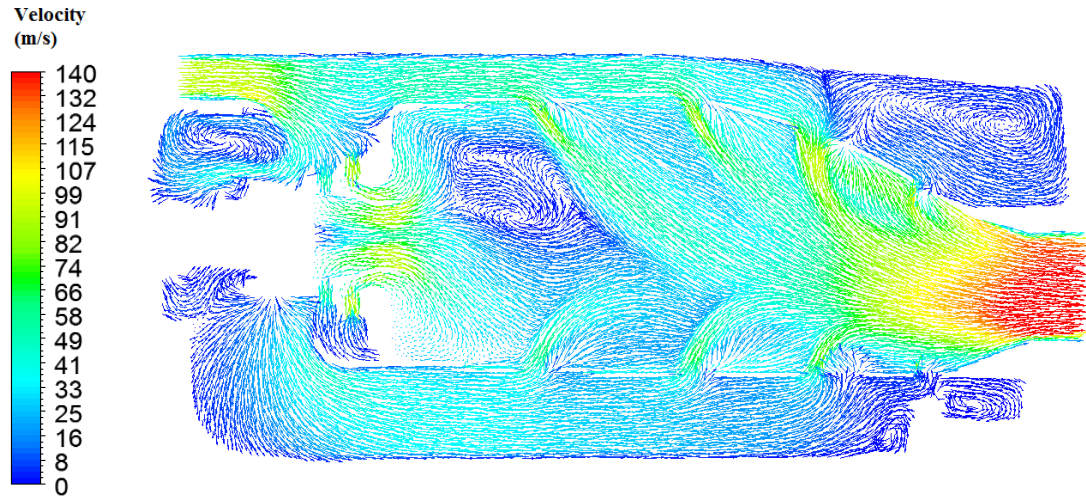


**Figure 5.14** – Velocity vector distribution along centerline section

Mach number characteristic of the combustion chamber, shown in Figure 5.15, gives information about the conformity of the design to the design limits. As mentioned at the beginning of this chapter, the air passing through the hole groups should have Mach number around 0.2-0.3 which is also consisted with the preliminary design results. However the Mach number values of the inner liner hole groups are lower than the outer hole group.

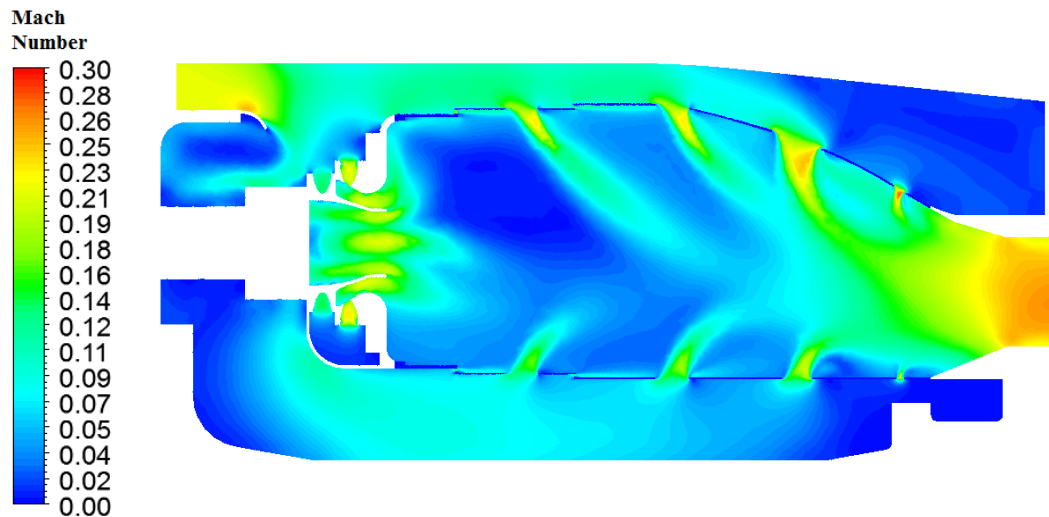


**Figure 5.15** – Mach number distribution along centerline section

The exit velocity and Mach number distribution are shown in Figure 5.16 and 5.17. The magnitude of the velocity increases towards the inner liner region. The Mach number character at the exit is more homogenous due to the effect of the high temperature at the exit.

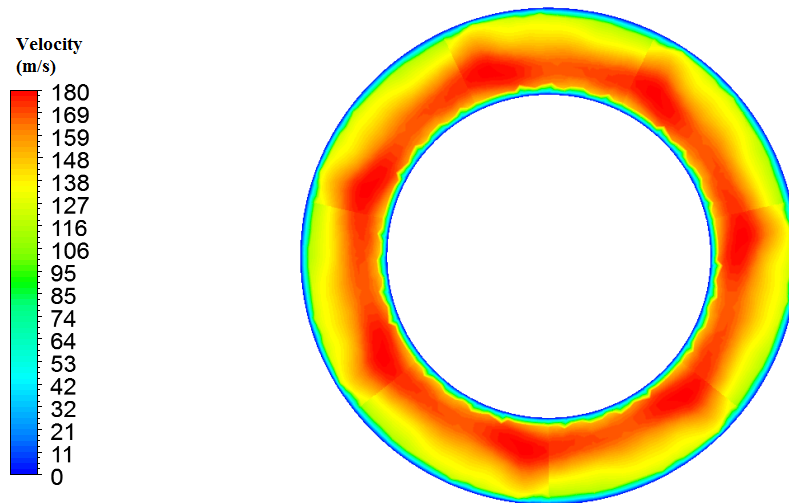


**Figure 5.16** – Velocity distribution at the exit plane

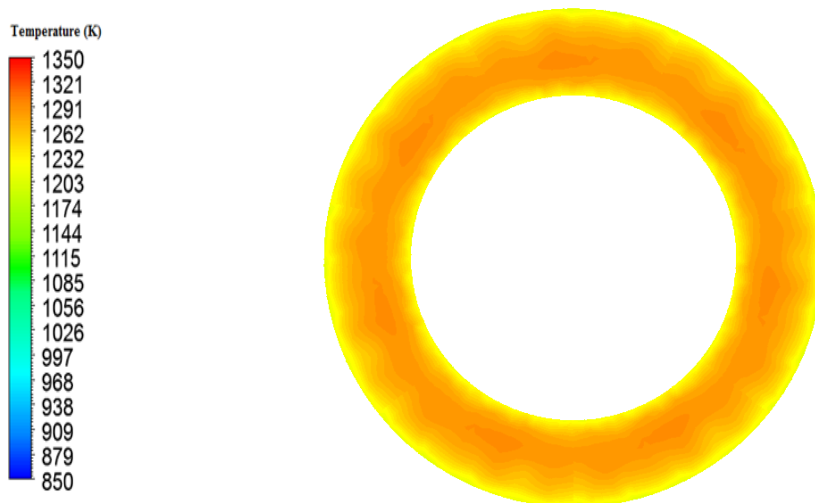


**Figure 5.17** – Mach number distribution at the exit plane

### 5.6.3.2 Flow Streamline

Streamlines of the flow particles released from the inlet of the flow field is given in Figure 5.18. Some significant findings can be observed from the figure, it is concluded in the previous section that the inner liner flow is lower than the outer liner flow this situation is also can be observed in the figure less particles are going to the inner liner region. The swirler region and its effect to the main liner flow can be seen also in the figure. The swirler flow causes a low velocity region in the primary zone of the combustor, in which the particles are following radial path.

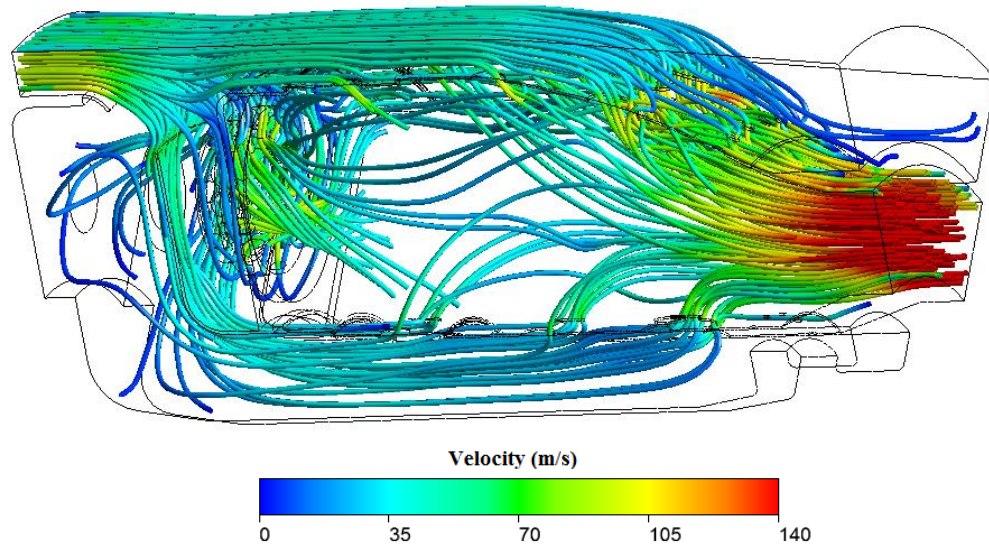


**Figure 5.18** – Streamlines emanating from the inlet

Figure 5.19 shows the particles emanated from the swirler holes. The significant amount of particles is joined to the mainstream and the rest of them are going in radial direction in to neighboring combustor segment zones. Particles released from the other hole groups (primary, secondary, dilution 1 and dilution 2) are shown in Figure 5.20. They are all combined at the converging section of the combustor. Most of these particles are following in the axial direction.

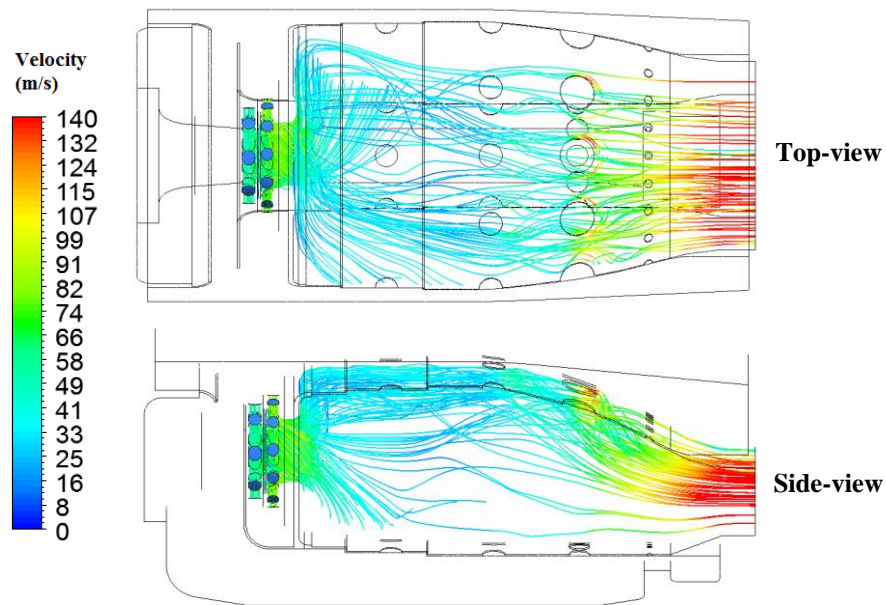


**Figure 5.19** – Streamlines emanating from the swirler holes

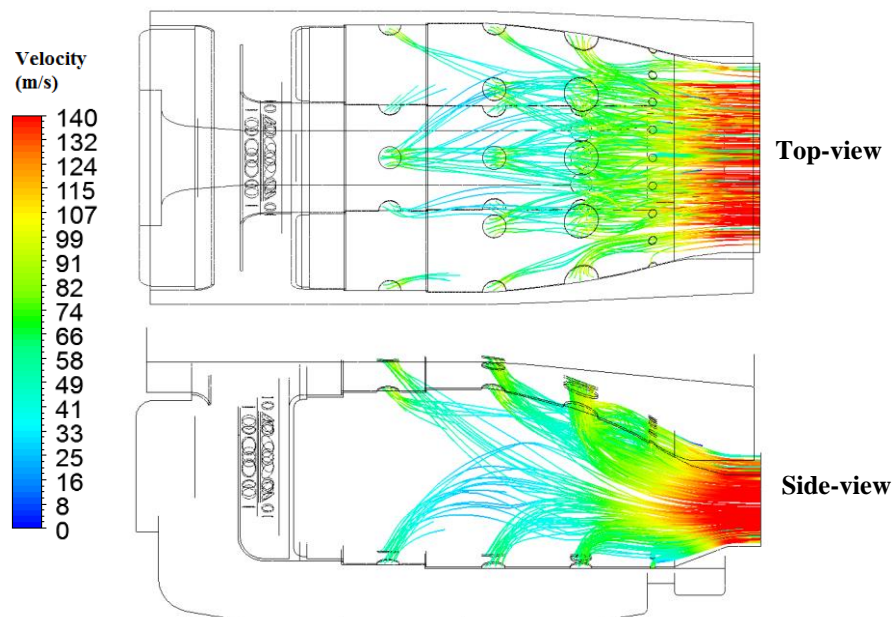


**Figure 5.20** – Streamlines emanating from liner holes

### 5.6.3.3 Temperature Results

Temperature distribution along the centerline section is shown in Figure 5.21. The temperature distribution shows a different character inside the chamber than the



previous design. By the effect of the wall cooling holes, near wall regions of the 1<sup>st</sup> and 2<sup>nd</sup> zone are having a significantly lower temperature character, see chapter 4.

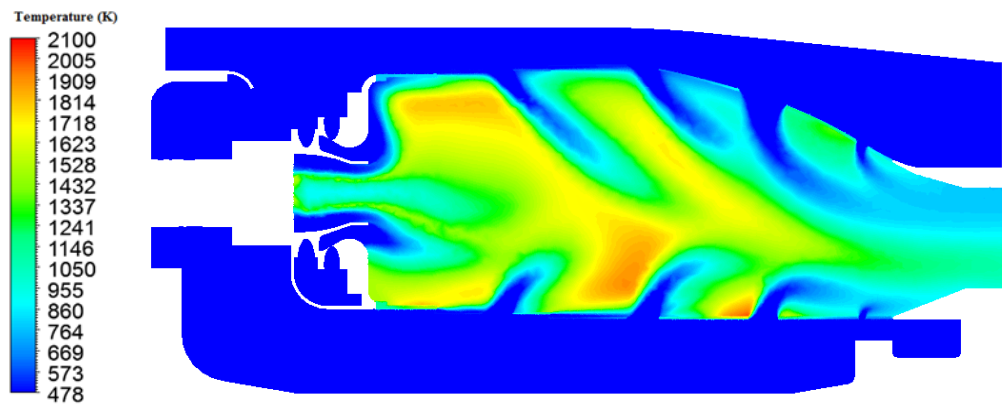


**Figure 5.21** – Temperature distribution along centerline section

The exit temperature profile shows its peak values near the center of the combustor, by this way this design is significantly improved version of the previous one. This is strictly related with the increased combustion volume. The average exit temperature of the chamber is dropped to 1070 K. In the original design the exit temperature was predicted as 1109 K, although the drop in average exit temperature is not desired, due to change in mixing character and modelling of radiation this new version has a lower exit temperature.

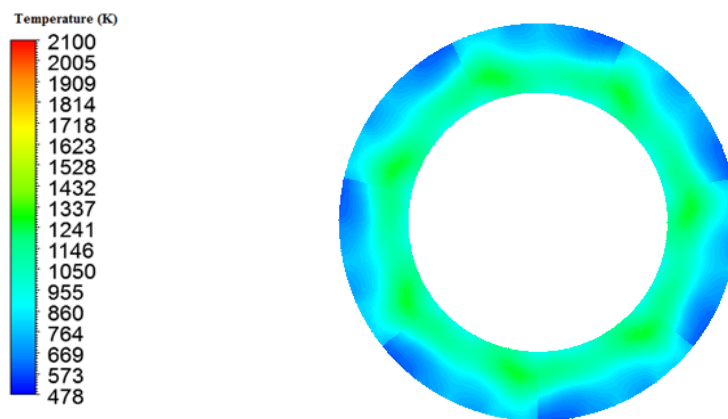


**Figure 5.22** – Temperature distribution at the exit plane

Figure 5.23 shows the temperature distribution on the section of outer and inner liner metal. In the analysis the liner material is selected as steel. As can be seen from the

figure, the temperature is significantly higher at upstream of the cooling holes. Primary cooling hole can be placed further upstream to cool more of the wall portion especially at the inner liner wall region.

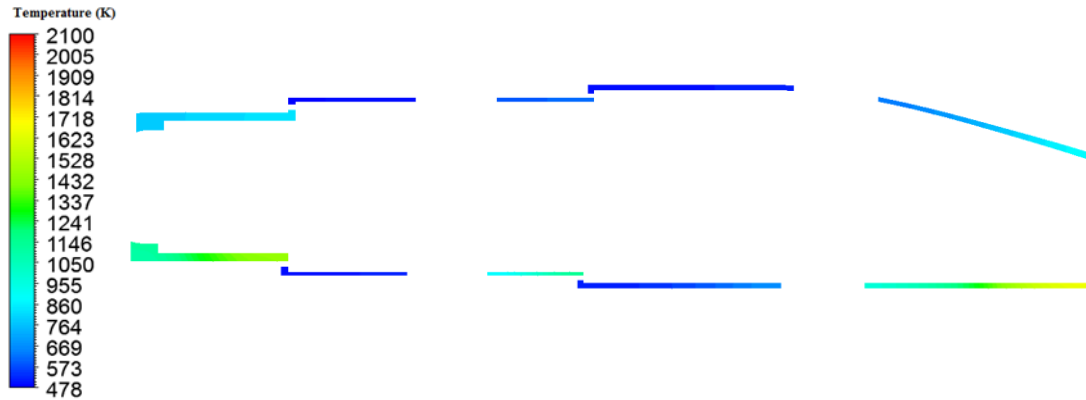


**Figure 5.23** – Temperature distribution on liner walls – centerline section

#### 5.6.3.4 Total Pressure Results

The total temperature figure shown in Figure 5.24, has a very similar character as in the original design. There is a pressure difference between the outer and inner annulus. Furthermore due to high radial flow, a peak total pressure values can be seen in the swirler zone. The average total pressure drop is calculated as 4618 Pa which is significantly lower than the original design, in which the total pressure drop value was 4988 Pa. This is also related with the new operation point of the chamber, since combustor loading is lowered in the new design the combustion performance parameters are positively affected and the chamber shows a better performance.



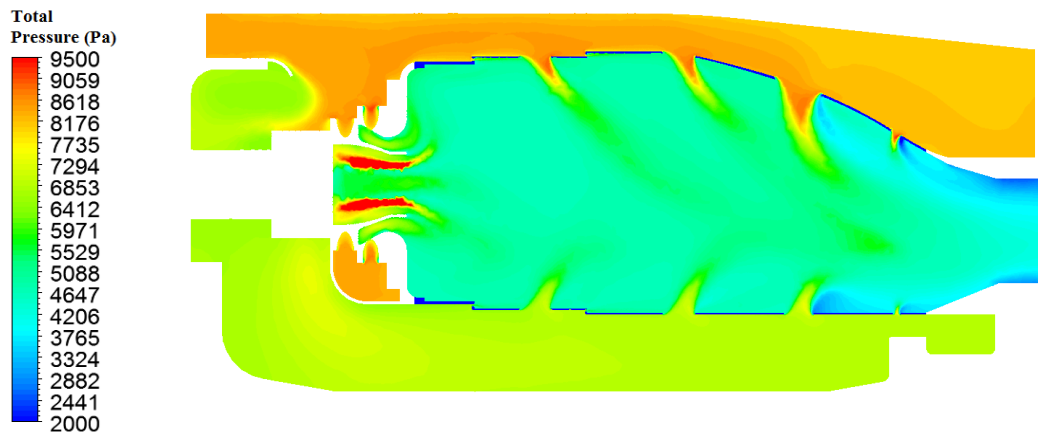


**Figure 5.24** - Total pressure distribution along centerline

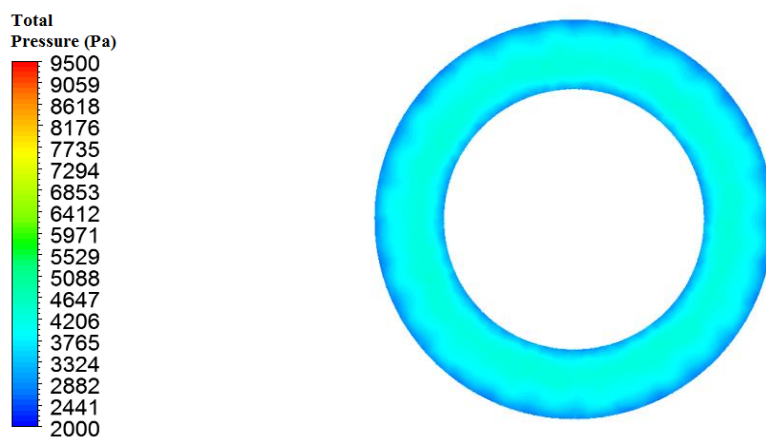


**Figure 4.64** - Pressure drop distribution at the exit plane



## CHAPTER 6

### CONCLUSION AND FUTURE WORK

#### 6.1 Conclusion

In this study a gas turbine performance prediction model was presented for three different flow network solvers. The coupling of the chemical reactor elements with the flow network elements and the solution procedure was given in detail. To conclude the study, two different chemical mechanisms were utilized and the effect of the mechanism change was also investigated.

Developed code is applied to a test combustor and the basic performance parameters are investigated. A significant performance parameter of the gas turbine combustors is pressure drop. By looking at the pressure figures, it can be inferred that in general for all of the flow network models the pressure levels are estimated with a significant error in annulus, the overall pressure drop showed 10 % to 20 % of error among the models. This is related with the hole flow discharge character, because the highest loss happens when flow is passing through the liner holes. The inner nodes inside the liner are more compatible with each other. From this point of view, it can be seen that non-linear model predicts a larger pressure loss through the liner holes; whereas LTM and segregated modes predicts a lower pressure loss through the liner holes. Non-linear method has an extra term in the pressure loss equation, equation (132) that term is actually responsible from this behavior because velocity values across a liner hole element depends on the local conditions at each node. One node is placed to the cold side the other node is on the hot side the density difference through this node causes that extra term to generate extra pressure drop. Actually it is the only

model among the flow models that takes this density variation at that stage. Actually that explains the outer annulus pressure levels in Figure 3.5 and general pressure drop trends in Figures 3.7 and 3.13. Pressure drop values of the CFD analysis and experiment are located between the lower prediction of the LTM and segregated methods and higher prediction of the non-linear method. The inner nodes in the network model are given reactor output temperatures directly, which is not the case in a real combustor. Because in 3D model, the temperature varies inside the combustor liner segments dramatically and local temperature just at the hole exits are not as high as the core region temperatures, that is the reason of higher predictions of non-linear model.

Temperature values at the elements of the liner, shown in Figures 3.9 and 3.15, shows that for the primary and secondary zones of combustor the reactor network predicts higher values however the results converge to reasonable values near the exit of the combustor. A better modeling approach can be made by adding extra reactors to the primary and secondary zones for modeling of the flow reversal in these regions, by this way the higher temperature values can be reduced and brought to reasonable levels. Figure 3.10 and 3.16 shows the average exit temperature comparison, reactor models neglect the mixing, and other effects as a result they predict higher temperatures.

Liner hole flow distributions presented on Tables 3.7 and 3.8 shows that the mass flow percentage passing through the holes are nearly predicted at the same levels. However, non-linear mode predicts a 1.8 % higher mass flow through primary swirler holes whereas other models predict only 1 % through this hole. All three models predict nearly 5 % less air flow from dilution 1 outer hole group. And dilution 1 inner hole predicts 3.5 % higher. In general the deviations are nearly 3 to 5 percentage at maximum. LTM and segregated model predicts very close mass flow split predictions, whereas non-linear model is deviates from other two around 0.2-0.3 percentage. That is directly related with the pressure predictions explained above.

Two different mechanisms are used in this study and results are presented for each mechanism separately. The pressure results show no significant change by changing

the mechanism because the temperature levels in the liner nodes are nearly the same. However when the temperature results are examined, small difference in exit temperature of the 1D models can be noticed. The exit temperature with Aachen mechanism is found as 1238 K whereas Creck mechanism predicts 1227 K. A more remarkable degradation from switching from Aachen to Creck mechanism can be seen in CFD results average exit temperature differs nearly 60 K which is a significant difference.

The differences among the three solver models are explained above in terms of the basic performance parameters. However, it is also worth mentioning the convergence character and runtime of these three versions. As for the LTM and non-linear model, their convergence are not easily violated during solution steps their structures can bear flow-pressure variations at initial time steps. However non-linear model depends on the initial pressure distribution given to the system. If initial values are not carefully selected system may converge to an unphysical solution point. For all three methods low resistance lines may cause convergence problems. Segregated method has some convergence problem in high flow speed regions [13-14]. To overcome convergence problems in segregated method, an under-relaxation constant is applied to the pressure correction terms. The overall runtime of the three codes are given on Table 6.1. However notice that these times are for cold flow cases when reactors are not activated. If the reactor network is also activated the solution times goes from seconds to several minutes. The main reason is the length of the used mechanism in this study.

**Table 6.1** - Solver runtime comparison

<b>Solver Method</b>	<b>Runtime (s)</b>
<b>LTM Method</b>	0.14
<b>Segregated Method</b>	17.1
<b>Non-linear</b>	0.38

The verification of the performance figures are performed by using the results of the CFD analyses and experiments. CFD analyses are described in detail in verification

chapter. CFD results supply information about the 3D characteristics of the chamber and these properties cannot be obtained in a 1D analysis. The velocity figures of the centerline section figures shows the primary combustion zone just ahead of the swirler exit. Furthermore, the air penetration of the incomings flows from liner holes can also be observed. Although it is preferred to keep the main combustion zone in the primary zone which is between the exit of the swirler and primary liner hole group, in this test combustor the combustion doesn't completed in this zone but spreads into the other zones which can be seen in temperature figures and the CO iso-surface. As an intermediate species of combustion, CO is reveals the active combustion zones inside the domain. The high concentration zones of combustion products  $\text{CO}_2$  and  $\text{H}_2\text{O}$  also shows the active combustion zones inside the liner. This kind of regions cannot be predicted in preliminary design, so in a design cycle each preliminary design should be controlled with a detailed CFD analysis.

The combustor domain is also solved with SAS method to obtain instantaneous unsteady character of the chamber. Although the unsteady results didn't use as a mean of verification, the results are presented to show the unsteady character of the chamber. The difference between the instantaneous and average figures shows some difference which is a direct indication of time varying parameters inside the chamber. A 1D transient modelling of the chamber can also be performed for transient injection character or by assuming a transient velocity profile in primary combustion zone however these models are not covered in this study.

The developed performance characterization code is extended so it can be used as a design tool. Details of the design tool are presented in Chapter 5. A new design has been made by using the developed code. This design is an improved version of the case used in verification chapter. The combustor volume of the liner is doubled by this way the loading of combustor is decreased. The decrease of the combustor loading and intensity means a physically more stable design, and lower energy per unit volume, in general. In addition to that, 1<sup>st</sup> zone and 2<sup>nd</sup> zone of the combustor liner is improved by adding film cooling holes to protect the liner material from excessive temperatures at liner walls. All the design limits, cooling requirements are

presented in the design chapter. The design code calculated the mass flow split inside the chamber. It also calculated the inner combustion zone temperatures and revealed the film cooling requirements. The mass flow distribution inside the chamber is changed due to the existence of the cooling holes. The mass flow percentage passing through the liner flow holes in the old and new designs are summarized on Table 6.2. According to the numbers adding relatively small film cooling holes significantly affects the amount of dilution air passing through combustor. Mass percentage in the other holes is slightly changed. The annulus regions that are near the primary, secondary and film cooling holes are physically close and they are in the narrow region in the outer annulus. As a result the pressure difference causing the mass flow into liner is nearly remained unchanged by the existence of the film cooling holes. However, because the dilution holes lay at the rear region of the combustor, the amount of gas is dropped before the dilution holes. Hence, existence of film cooling holes critically effects the dilution hole flow.

**Table 6.2** – Mass flow rate percentage comparison of existing and new designs

	<b>Mass Flow Percentage %</b>	
	<b>Existing Design</b>	<b>New Design</b>
<b>swirler</b>	23.4	25.5
<b>primary</b>	11.3	11.3
<b>filmC 1</b>	-	4.1
<b>secondary</b>	18.6	18.6
<b>filmC 2</b>	-	4.1
<b>dilution1</b>	43.1	34.8
<b>dilution2</b>	3.5	1.6

In conclusion, this study presented a coupled flow and chemical reactor network model. Different solver types are written for the code. The results of the performance prediction code are verified by detailed numerical and experimental results. The developed code is developed further to include a design capability. By using this extended version an improved design was made for the test combustor and its results are also presented.

## 6.2 Future Work

The coupled flow and chemical reactor network model is used as a performance prediction tool in this study. In addition, it is improved for designing combustors. The model can be improved further to make better performance estimations inside the combustor zones. This can be done by splitting flow domain into smaller regions and focusing on the combustion reaction in these regions. However; utilizing more chemical reactors, increases the computational time for solution of this chemical network. To overcome the sophisticated calculations, simpler mechanisms can be utilized. Doing the design iterations with a simple chemical mechanism can be utilized and when the general parameters are converged one analysis with a complex mechanism can be solved. By using this approach a chemical modelling approach can be developed.

The 1D tool developed in this study is designed as a steady tool. It is possible to rearrange the tool to overcome simple transient cases like, transient inlet flow character or varying fuel flow rate. As described in the previous paragraph a simpler chemical mechanism can decrease the response time of the model to the transients significantly. 1D transient combustor model is also useful for the performance prediction groups. This kind of a code can be coupled with an engine performance prediction tools. Better predictions for on-design and off-design character of the engine can be obtained.



## REFERENCES

- [1] Lefebvre AH, Ballal DR. Gas Trubine Combustion. 3<sup>rd</sup> ed. CRC Press; 2010.
- [2] Walsh PP, Fletcher P. Gas Turbine Performance. 2<sup>nd</sup> ed. Blackwell Science; 2004.
- [3] Boyce MP, Gas Turbine Engineering Handbook. 3<sup>rd</sup> ed. Gulf Professional Publishing; 2006.
- [4] Greyvenstein GP, Laurie DP. A Segregated CFD Approach to Pipe Network Analysis. International Journal for Numerical Methods in Engineering. 1994; 37: 3685-3705.
- [5] Liu H. Pipeline Engineering. Lewis Publishers; 2003.
- [6] Stuttaford PJ. Preliminary Gas Turbine Combustor Design Using a Network Approach. PhD Thesis, Schoold of Mechanical Engineering, Cranfield University; 1997.
- [7] Dupuis P, Robert JL, Ouellet Y, A Modified element Method for Pipe Network Analysis. Journal of Hydraulic research. 1987; 25: 1
- [8] Costa ALH, de Medeiros JL, Pessoa FLP. Steady-State Modeling and Simulation of Pipeline Networks for Compressible Fluids. Braz. J. Chem. Eng. 1998; 15: 4.
- [9] Krope J, Dobersek D, Goricanec D. Flow Pressure Analysis of Pipe Networks with Linear Theory Method. Proceedings of the International Conference on Fluid Mechanics. 2006; 59-62.
- [10] Krope J, Trop P, Goricanec D. Flow-Pressure Analysis of Loop Gas Networks. International Journal of Systems Applications, Engineering & Development. 2011; 4: 5.
- [11] Jeppson RW. Steady Flow Analysis of Pipe Networks: An Instructional Manual. 1974. Reports. Paper 300. [http://digitalcommons.usu.edu/water\\_rep/300](http://digitalcommons.usu.edu/water_rep/300) [Last accessed on 05.08.2015]

- [12] Stuttaford PJ, Rubini PA. Preliminary Gas Turbine COmbustor Design Using a Network Approach. Transactions of the ASME. 1997; 119: 546-552.
- [13] Pretorius JJ. A Network Approach for The Prediction of Flow and Flow Splits within A Gas Turbine Combustor. MSc Thesis, Faculty of Engineering, University of Pretoria; 2005.
- [14] Pretorius JJ, Malan AG, Visser JA. A Flow Network Formulation for Compressible and Incompressible Flow. International Journal of Numerical Methods for Heat & Fluid Flow. 2008; 18: 2: 185-201
- [15] Tabkhi F, Pibouleau L, Azzaro-Pantel C, Domenech S. Total Cost Minimization of a High-Pressure Natural Gas Network. Journal of Energy Resources Technology. 2009; 131
- [16] Tabkhi F, Pibouleau L, Azzaro-Pantel C, Domenech S. Improving the Performance of Natural Gas Pipeline Networks Fuel Consumption Minimization Problems. AIChE Journal. 2010; 56: 4: 946-964.
- [17] Murthy JN, Gas Turbine Combustor Modelling for Design. PhD Thesis, School of Mechanical Engineering, Cranfield University; 1988.
- [18] Falcitelli M, Pasini S, Rossi N, Tognotti L. CFD+Reactor Network Analysis: An Integrated Methodology for The Modeling and Optimisation of Industrial Systems for Energy Saving and Pollution Reduction. Applied Thermal Engineering. 2002; 22: 971-979.
- [19] Fichet V, Kanniche M, Plion P, Gicquel O. A Reactor Network Model for Predicting NOx Emissions in Gas Turbines. Fuel. 2010; 89:2202-2210.
- [20] De Toni A, Hayashi T, Schneider P. A Reactor Network Model for Predicting NOx Emissions in an Industrial Natural Gas Burner. J. Braz. Soc. Mech. Sci. Eng. 2013; 35: 199-206.
- [21] Chen X, Zheng H, Pan G. Preliminary Combustor Design Using a Network Approach Based on Chemical Reactor Modeling. Journal of Chemical and Pharmaceutical Research. 2013; 5(12): 599-606.
- [22] Novosselov IV. Chemical Reactor Networks for Combustion System Modeling. PhD Thesis, Mechanical Engineering, University of Washington; 2006.
- [23] Rezvani R. A Conceptual Methodology for The Prediction of Engine Emissions. PhD Thesis, School of Aerospace/ College of Engineering, Georgia Institute of Technology; 2010.

- [24] Drennan SA, Chou CP, Shelburn AF, Hodgson DW, Wang C, Naik CV, Meeks E, Karim H. Flow Field Derived Equivalent Reactor Networks for Accurate Chemistry Simulation In Gas Turbine Combustors. Proceeding of ASME Turbo Expo. 2009; GT2009-59861.
- [25] Xu K, Shen S, Li C, Zheng L. A New Procedure For Predicting NO<sub>x</sub> Emission in Preliminary Gas Turbine Combustor Design. Proceeding of ASME Turbo Expo. 2013; GT2013-95248.
- [26] Nilsson T. Development of A Simulation Methodology for Gas Turbine Combustion. MSc Thesis, Lund University; 2014.
- [27] Cantera Documentation on Reactor Networks. [Online]. Available: [www.cantera.org/docs/sphinx/html/reactors.html](http://www.cantera.org/docs/sphinx/html/reactors.html) [Last accessed on 15.01.2016]
- [28] White FM. Fluid Mechanics. 7<sup>th</sup> ed. McGraw Hill; 2011.
- [29] Colket M, Edwards T, Williams S, Cernansky NP, Miller DL, Egolfopoulos F, Lindstedt P, Seshadri K, Dryer FL, Chung KL, Friend D, Lenhart DB, Pitsch H, Sarofim A, Smooke M, Tsang W. Development of an Experimental Database and Kinetic Models for Surrogate Jet Fuels. American Institute of Aeronautics and Astronautics. 2007.
- [30] Oldani AL. Surrogate Modeling of Alternative Jet Fuels for Study of Autoignition Characteristics. MSc Thesis, University of Illinois at Urbana-Champaign; 2014.
- [31] Honnet S, Seshadri K, Niemann U, Peters N. A Surrogate Fuel for Kerosene. Thirty-Second International Symposium on Combustion. 2008. [Online]. Available: [www.itv.rwth-aachen.de](http://www.itv.rwth-aachen.de)
- [32] Ranzi E, Frassoldati A, Stagni A, Pelucchi M, Cuoci A, Faravelli T. Reduced Kinetic Schemes of Complex Reaction Systems: Fossil and Biomass-Derived Transportation Fuels. International Journal of Chemical Kinetics. 2014.
- [33] Ranzi E, Frassoldati A, Grana R, Cuoci A, Faravelli T, Kelley AP, Law CK. Hierarchical and Comparative Kinetic Modeling of Laminar Flame Speeds of Hydrocarbon and Oxygenated Fuels. Progress in Energy and Combustion Science. 2012; 38: 468-501.
- [34] Topal A, Çatorı C, Çağan L, Uslu S, Turan Ö, Pişkin A. One-Dimensional Heat Transfer Analysis and Experimental Investigation of A Gas Turbine Combustor. CONV-14: Int. Symp. on Convective Heat and Mass Transfer. 2014; CONV-14-123.

- [35] Peters N. Turbulent Combustion. Cambridge University Press; 2000.
- [36] Hataysal SE, Yozgatlıgil A. Effect of Different Reaction Mechanisms on Calculation of A Jet Flame. Eighth Mediterranean Combustion Symposium. 2013.
- [37] Versteeg HK, Malalasekara W An Introduction to Computational Fluid Mechanics. 2<sup>nd</sup> Edition, Pearson Education Press. 2007.
- [38] Menter FR, Egorov Y. Turbulence Models Based on the Length-Scale Equation. 4<sup>th</sup> international Symposium on Turbulent Shear. 2004.
- [39] Menter F. Scale Resolving Simulations in CFD. Presentation, ANSYS. 2010.
- [40] Nam NG. CFD Simulation of a Gas Turbine Combustor. Ottawa-Carleton Institute for Mechanical and Aerospace Engineering. 2003.
- [41] ANSYS Fluent Theory Guide, Version 14.5. ANSYS. Germany. 2014.



## APPENDIX A

### EXPERIMENTAL EQUIPMENTS

#### A.1 Temperature Measurements

For temperature measurement K type thermocouples are utilized. They have a straight connection with the data acquisition system. Two types of thermocouples are utilized for measuring the temperature throughout the system. For measuring inlet temperature and outer casing temperature of the set-up low temperature thermocouples are used. For measuring exit temperature profile high temperature thermocouples are used. Technical specs and other details of the thermocouples are given on Table A.1


**Table A.1– Thermocouple properties**

MODEL	Details	Tech. Specs.	Figure
<b>Omega KMTIN</b>	Exhaust Gas Temp	<ul style="list-style-type: none"> <li>• K Type</li> <li>• Max Temp: 1335 °C</li> <li>• Direct connection to acq. system</li> </ul>	
<b>Omega TJ36- CAXL</b>	Inlet temp, surface Temperature Measurements	<ul style="list-style-type: none"> <li>• K Type</li> <li>• Max Temp: 480 °C</li> <li>• Direct connection to acq. system</li> </ul>	

## A.2 Pressure Measurements

Performance tests are performed under atmospheric conditions, meaning the exit of the combustor is opened to the atmosphere. Pressure data is measured from 2 distinct location of the combustor. The first one is the entrance of the combustor to measure the air pressure before entering the combustion chamber. The second location is the exit plane. The measurement of the exit plane is done by utilizing special probe to prevent overheating of the transducer itself. The other end of the probe is attached to the pressure transducer. The details of the pressure transducer used are given on Table A.2


**Table A.2**– Pressure transducer properties

MODEL	Details	Tech. Specs.	Figure
UNIK 5000	Low pressure measurement	<ul style="list-style-type: none"><li>• -170-+180 mbar, 1500mbar, 350 mbar</li><li>• Acc. %0.04.</li><li>• Freq. resp. 3500 kHz.</li><li>• Operating temperature - 55 to 125 °C</li></ul>	

## A.3 Species Concentration Measurements

For measuring exit species concentration an exhaust gas analyzer is utilized. This measurement unit is a compact system and it includes the data acquisition system and the probe on it. The exhaust gas is sucked by the probe of the data analyzer and the gas sample going inside the system is analyzed. The system includes its inner pump to get samples from the probe. It has the capability for measuring the O<sub>2</sub>, CO<sub>2</sub>, CO, NO<sub>x</sub>, C<sub>x</sub>H<sub>y</sub> concentration and temperature can be measured also. The type and details of the gas analyzer unit is given on Table A.3 and Table A.4.

**Table A.3–** Gas analyzer unit properties

MODEL	Details	Tech. Specs.	Figure
<b>TESTO 350 M/XL</b>	Species Measurement	<ul style="list-style-type: none"> <li>• -Compact unit includes probe and data acquisition part</li> <li>• Table 4.5</li> </ul>	

**Table A.4–** Gas analyzer measurement specs.

Probe Type	Measurement Range	Accuracy	Resolution	Reaction time (s)
O <sub>2</sub>	0...+25 vol. % O <sub>2</sub>	+/- 0.8 %	0.1 Vol. %O <sub>2</sub>	20
CO	0...+10000 ppm CO	+/- 5 %	1 ppm CO	40
Nox	0...+3000 ppm Nox	+/- 5 %	1 ppm CO	30
CO <sub>2</sub>	0...+50 vol. % CO <sub>2</sub>	+/- 0.3 %	0.01 Vol. %CO <sub>2</sub>	10
C <sub>x</sub> H <sub>y</sub>	-	10 %	10 ppm	40





## **CURRICULUM VITAE**

### **PERSONAL INFORMATION**

Date - Place of Birth: 22 June 1983 - Ankara

Nationality: Republic of Turkey

Marital Status: Married

Languages: English (Advanced) - Turkish (Native)

### **EDUCATION**

**M.Sc., Middle East Technical University / Mechanical Engineering Dept.**  
(09.2009)

Thesis Title: Simulation of Aerodynamic Drag of a Heavy Commercial Vehicle

**B.S., Middle East Technical University / Mechanical Engineering Dept.**  
(06.2006)

### **PROFESSIONAL EXPERIENCE**

**ARUP UKMEA:** November 2015 - present

Senior Mechanical Engineer

**TUSAS Engine Industries (TEI):** January 2014 – November 2015

Integrated Program Team Leader / CFD Combustion

**ASELSAN:** December 2011 - December 2013

Mechanical / CFD Engineer

**Middle East Technical University, Mechanical Engineering Dept.:** September 2006 - November 2011

Teaching Assistant

### **CORE COMPETENCIES**

**Combustion Modeling/Chamber Design:** Utilization of 1D and 3D numerical methods and tools for preliminary and detailed design and analysis of combustion chambers. Usage of detailed chemistry tools (Cosilab and Cantera) to predict accurate species and temperature distribution.

**Fluid Systems Analysis/Design:** Analysis and design of external flow cases. CFD analysis of the external aerodynamics of vehicles or external units attached to the aircrafts. Calculation of drag, pressure distribution and aero-thermal heating. (Utilization of 3D CFD tools.)

Determination of internal flow distribution inside the tunnel network systems and combustors in preliminary design. Utilization/coding of 1D CFD tools for calculation of flow distribution. CFD Analysis of complex problems such as station fires or tunnel fires.

**Thermal Analysis/Design:** Thermal analysis of electronic packages/boxes including electronic units. Defining the ventilation requirements of the interior of the boxes. Coupled analysis of external units which are including electronic units inside. Wind analysis in large fields and thermal plume behavior analysis.